Micro- and nanoanatomy of human brain tissues

Inaugural dissertation
to
be awarded the degree of Dr. sc. med.
presented at
the Faculty of Medicine

of the University of Basel

by

Anna Khimchenko

from Kiew, Ukraine

Basel, 2017

Approved by the Faculty of Medicine

On application of

Prof. Dr. Bert Müller

Basel, the 26 June 2017

Prof. Dr. Thomas Gasser
Dean

Contents

Acknowledgements

This work was only possible due to the contribution and cooperation of a number of people. I would like to take this opportunity to thank all of them.

First and foremost, I would like to thank my supervisor, **Prof Dr. Bert Müller**, for giving me the opportunity to work on this exciting project at the Biomaterials Science Center and for mentoring my work. Prof Dr. Bert Müller is a great supervisor, and his door was always open if I ever had any questions.

My thank also go to **Dr. Georg Schulz** for his guidance throughout the realisation of this work. He actively supported me scientifically and technically, and I thank him for introducing me to phase-contrast computed tomography, for always providing professional feedback on my work and for support in times when the night was dark.

A special thank you goes to **Dr. Simone E. Hieber** for all the fruitful discussions and inspirations to think outside the box. She was the driving force that initiated visualisation of paraffin-embedded specimens - opened door to a new world for researchers. Moreover, I thank her for irreplaceable contributions to data segmentation.

I thank **Dr. Hans Deyhle** for sharing invaluable knowledge on tomographic imaging and overall help. I feel very fortunate and honoured to have a chance to experiment, analyse data and write papers with him.

Special thanks go to all present and past members of the Biomaterials Science Center, in particular **Verena Grötzinger, Willy Kuo, Sofia Matviykiv, Dr. Simon Bugna, Gabriela Gerganova, Dr. Marco Dominietto, Dr. Florian Weiss and Dr. Margaret Holme**, for the great atmosphere and cooperation. I cannot express how much I have learned, grown and enjoyed working with them. It has been an extraordinary privilege to have met them.

I thank **Prof. Dr. Magdalena Müller-Gerbl** for kindly acting as co-referee and for the evaluation of my thesis. Please let me emphasise that I am grateful for her active support of my work.

I wish also to thank **Peter Thalmann** for supporting me during many challenging programming problems in MATLAB and ITK - he was always open to any type of question. Throughout the years, we have solved a lot of puzzles together and seen the magic of data registration and reconstruction.

I thank **Natalia Chicherova** for the availability of the 2D-3D registration tool, as without her, automatic registration of the two-dimensional histology to the tomographic data would never have been possible. I learned so much working with her.

Thank you **Dr. Christos Bikis** for the great help with specimen preparation, related histology and support regarding medical questions. I really enjoyed working with him.

I would like to express my gratitude to **Prof. Dr. Atsushi Momose** for kindly being the external reviewer of the PhD-thesis.

Sincere thanks are given to **Dr. Alexander Rack** for his support during all beamtimes at ID19, as well as timely help and assistance.

I extend my gratitude to **Dr. Alexandra Pacureanu** and **Dr. Peter Cloetens** with whom I had the pleasure of acquiring and reconstructing the nano-holotomography data. The friendly and supportive atmosphere provided by members of the ID16 team was greatly appreciated.

Furthermore, I thank **Dr. Felix Beckmann**, **Dr. Alexander Hipp**, **Dr. Julia Herzen** and **Dr. Imke Greving** for their patience and continuous support during the beamtimes at DESY.

My sincere gratitude goes to **Dr. Irene Zanette**, **Marie-Christine Zdora**, **Dr. Joan Vila-Comamala** and **Dr. Christoph Rau** for their kind assistance during the beamtimes at Diamond.

I would like to thank **Gabriel Schweighauser** and **Dr. Jürgen Hench** for the organisation and preparation of the human tissues, as well as excellent support during medical questions, preparation of histological sections and for bringing my attention to combing multi-modal data.

My gratitude goes to **Sascha Martin** for helping me with phantom preparation, with his prompt and invaluable support.

I would like to express my gratitude to **Marzia Buscema** for keeping up my motivation when I could not see the light at the end of the tunnel.

I would like to thank **Bekim Osmani** for his help with the special preparation required for vacuum conditions and stimulating discussions.

I would like to thank **Dr. Tino Töpper** who was always willing to help and for creating a very nice atmosphere.

Parts of this book have been proof-read by Peter Thalmann, Dr. Tino Töpper, Dr. Simone E. Hieber, Dr. Georg Schulz and Alexandra Dombrovskiy. I thank them all for kind help!

The financial support provided by the Swiss National Science Foundation is greatly acknowledged.

Last but not least, I would like to thank my parents and friends for giving me all the assistance I needed and for their never-ending, positive motivation. I also thank my husband, **Alexander Dombrovskiy**, for always being with me and for all his support during my studies.

Summary

"*Better to see something once than to hear about it a thousand times.*"
Proverb

The human brain is one of the most complex organs in the body, containing billions of neurons of hundreds of types. To understand its properties and functionality at the most fundamental level, one must reveal and describe its structure down to the (sub-)cellular level. In general, three-dimensional (3D) characterisation of physically soft tissues is a challenge. Thus, the possibility of performing non-destructive label-free 3D imaging with the reasonable sensitivity, resolution and increased manageable specimen sizes, especially within the laboratory environment, is of great interest.

The focus of the thesis relies on the non-destructive 3D investigation of the micro- and nanoanatomy of human brain tissues. The ambitious challenge faced was to bridge the performance gap between the tomography data from laboratory systems, histological approaches employed by anatomists and pathologists, and synchrotron radiation-based tomography, by taking advantage of recent developments in X-ray tomographic imaging.

The main reached milestones of the project include (i) visualisation of individual Purkinje cells in a label-free manner by laboratory-based absorption-contrast micro computed tomography (LBµCT), (ii) incorporation of the double-grating interferometer into the nanotom® m (GE Sensing & Inspection Technologies GmbH, Wunstorf, Germany) for phase-contrast imaging and (iii) visualisation and quantification of sub-cellular structures using nano-holotomography (nano-imaging beamline ID16A-NI, European Synchrotron Radiation Facility (ESRF), Grenoble, France).

Hard X-ray micro computed tomography (µCT) in the absorption-contrast mode is well-established for hard tissue visualisation. However, performance in relation to lower density materials, such as *post mortem* brain tissues, is questionable, as attenuation differences between anatomical features are weak. It was demonstrated, through the example of a formalin-fixed paraffin-embedded (FFPE) human cerebellum, that absorption-contrast laboratory-based micro computed tomography can provide premium contrast images, complementary to hematoxylin and eosin (H&E) stained histological sections. Based on our knowledge, the detection of individual Purkinje cells without a dedicated contrast agent is unique in the field of absorption-contrast laboratory-based micro computed tomography. As the intensity of H&E staining of histological sections and the attenuation contrast of LBµCT data demonstrated a correlation, pseudo-colouring of tomography data according to the H&E stain can be performed, virtually extending two-dimensional (2D) histology into the third dimension. The LBµCT of FFPE samples can be understood as a time-efficient and reliable tissue visualisation methodology, and so it could become a method of choice for imaging of relatively large specimens within the laboratory environment.

Comparing the data acquired at the LBµCT system nanotom® m and synchrotron radiation facilities (Diamond-Manchester Imaging Branchline I13-2, Diamond Light Source, Didcot, UK and Microtomography beamline ID19, ESRF), it was demonstrated that all selected modalities, namely LBµCT, synchrotron radiation-based in-line phase-contrast tomography using single-distance phase reconstruction and synchrotron radiation-based grating interferometry, can reach cellular resolution.

As phase contrast yields better data quality for soft tissues, and in order to overcome the restrictions of limited beamtime access for phase-contrast measurements,

a commercially available advanced µCT system nanotom® m was equipped with an X-ray double-grating interferometer (XDGI). The successful performance of the interferometer in the tomography mode was demonstrated on a human knee joint sample. XDGI provided enough contrast (1.094 ± 0.152) and spatial resolution (73 ± 6) µm to identify the cartilage layer, which is not recognised in the absorption mode without staining. These results suggest that the extension of a commercially available absorption-contrast µCT system via grating interferometry offers the potential to fill the performance gap between LBµCT and phase-contrast µCT using synchrotron radiation in the visualising soft tissues.

Although optical microscopy of stained tissue sections enables the quantification of neuron morphology within brain tissues in health and disease, the lateral spatial resolution of histological sections is limited to the wavelength of visible light, while the orthogonal resolution is usually restricted to the section´s thickness. Based on the data acquired from the ID16A-NI, the study demonstrated the application of hard X-ray nano-holotomography with isotropic voxels down to 25 nm for the three-dimensional visualising the human cerebellum and neocortex. The images exhibit a reasonable contrast to noise ratio and a spatial resolution of at least 84 nm. Therefore, the three-dimensional data resembles the surface images obtained by electron microscopy (EM), but in this case electron dense staining is avoided. The (sub-)cellular structures within the Purkinje, granule, stellate and pyramidal cells of the FFPE tissue blocks were resolved and segmented. Micrometre spatial resolution is routinely achieved at synchrotron radiation facilities worldwide, while reaching the isotropic 100-nm barrier for soft tissues without applying any dedicated contrast agent, labelling or tissue-transformation is a challenge that could set a new standard in non-destructive 3D imaging.

Chapter 1

Introduction

In the following, a review of different microscopy and tomography methods will give a short overview of the existing techniques, highlighting the current state of the art.

Review of visualisation techniques

Current *in vivo* imaging modalities established in clinical diagnostics, such as magnetic resonance imaging (MRI), positron emission tomography (PET), electroencephalography (EEG), magnetoencephalography (MEG), single-photon emission computed tomography (SPECT) with their functional sub-modalities, can only reach a spatial resolution of a fraction of a millimetre, with the exception of microscopic magnetic resonance imaging (µMRI), microscopic positron emission tomography (µPET) and microscopic single photon emission computed tomography (µSPECT). Nevertheless, these modalities are successfully applied for identifying structural and functional changes at the macroscale [1–3].

In contrast, *ex vivo* imaging modalities can reach the sub-cellular level. Light microscopy (LM) of stained tissue sections remains a "gold standard" tool in neuroscience [4]. Electron microscopy (EM) has even higher resolving power. Nevertheless, both modalities, EM and LM, are mainly limited to the 2D investigation and require the use of additional materials for contrast enhancement.

3D data can be acquired by serial sectioning or optical-ablative [5] imaging methods, for example through optical [6–8], two-photon or multi-photon [9, 10], electron [11, 12], confocal [13], deconvolution, or array [14] microscopy and tomography. The main drawbacks of these methods are associated with sectioning requirement [6].

Sectioning-free methods combined with tissue-clearing or -transformation [15–17] to increase penetration depth, offer 3D imaging of ultrastructure within mm-thick samples [18]. However, optical clearing is a technically demanding process with limitations in the number of different protocols that can be applied to the same specimen.

X-ray imaging, on the contrary, allows for 3D visualising samples down to nanometre resolution. For example, X-ray microscopy [19–23] is suitable for visualising biological specimens with quantitative contrast. Nonetheless, X-ray microscopy modalities are mainly limited in their field of view (FOV).

Ptychographic computed tomography (ptychography) is another promising imaging modality. However, in the current state, data analysis and image reconstruction are highly complex and time-consuming [24].

X-ray imaging

Almost since their discovery by Wilhelm Conrad Röntgen in 1895, X-rays have been used successfully in many fields, including medicine and biology, where it allows mapping the microstructures within human tissues. To date, X-ray computed tomography provides the best spatial resolution of all clinical three-dimensional imaging modalities.

Nevertheless, there are different principles of X-ray imaging, all are based on the fundamental aspects of the theory of X-ray interaction with matter. A more detailed treatment of the topic can be found in [25].

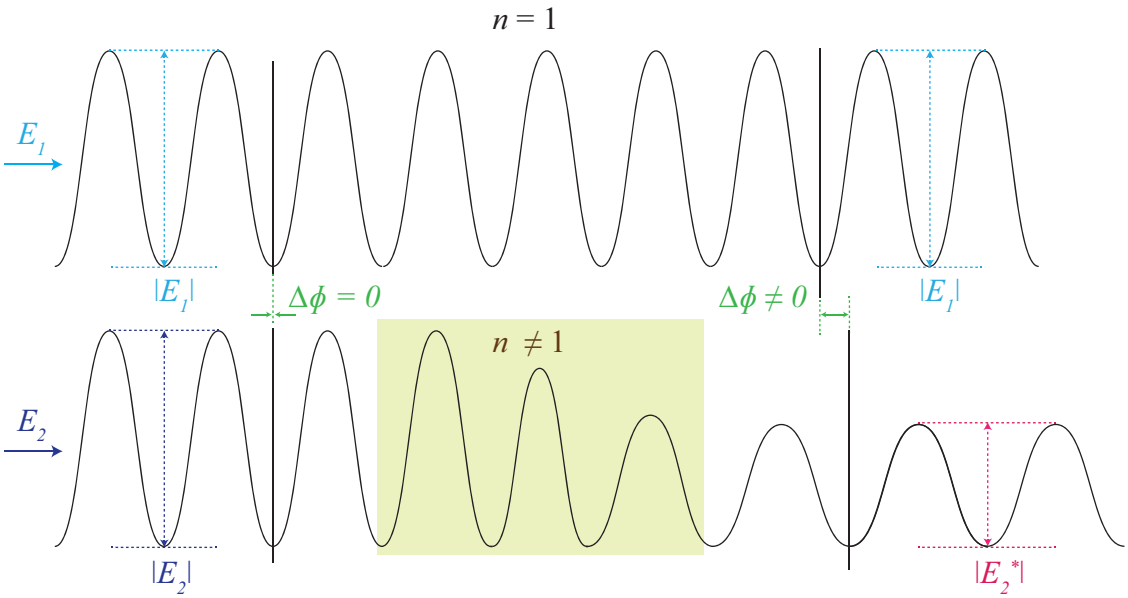

Figure 1: Schematic drawing of attenuation and phase shift of two electromagnetic waves E_1 and E_2 propagating in a free space with refractive index $n(x, y, z) = 1$ and a medium with $n(x, y, z) \neq 1$, respectively. $\mid E_1 \mid$: amplitude of the wave E_1; $\mid E_2 \mid$: amplitude of the wave E_2; $\mid E_2^* \mid$: modified amplitude of the wave E_2 after passing the matter (light green); $\triangle\phi$: phase shift.

In order to describe the interaction between X-rays and matter, the complex refractive index $n(x, y, z)$ is used

$$n(x, y, z) = 1 - \delta(x, y, z) + i\beta(x, y, z), \tag{1.1}$$

where $\delta(x, y, z)$ denotes refractive index decrement, accounting for phase-shift, and $\beta(x, y, z)$ is the imaginary part of the complex refractive index, accounting for attenuation. Both $\delta(x, y, z)$ and $\beta(x, y, z)$ are real-value, dimensionless quantities and depend on the matter and radiation. In a free space $n(x, y, z) = 1$, thus $\delta(x, y, z) = \beta(x, y, z) = 0$.

Lets consider two non-polarized monochromatic plane waves E_1 and E_2, see Figure 1. Wave E_1 propagates through a free space, where the refractive index $n(x, y, z) = 1$. Thus, wave E_1 remains unperturbed. Wave E_2 passes through a homogeneous medium with refractive index $n(x, y, z) \neq 1$. Thus, the amplitude is reduced to $\mid E_2 \mid > \mid E_2^* \mid$ and phase shifted with respect to the unperturbed wave $\triangle\phi \neq 0$. $\mid E_2^* \mid$ is a modified amplitude of the wave E_2 after passing the matter.

Absorption-contrast imaging

Conventional hard X-ray imaging approaches rely on X-ray absorption, whereby image contrast is related to the *linear attenuation coefficient* $\mu(x, y, z)$

$$\mu(x, y, z) = \frac{4\pi}{\lambda} \cdot \beta(x, y, z), \tag{1.2}$$

where λ denotes the wavelength of the incident X-rays.

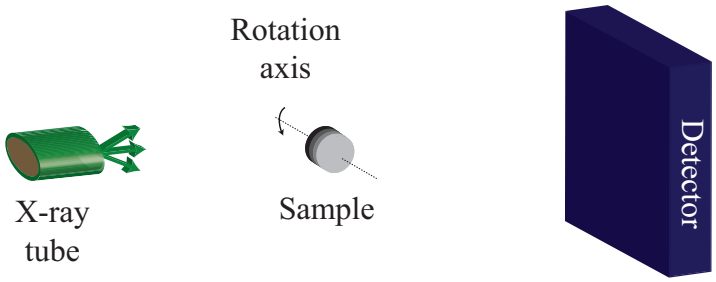

Figure 2: Schematic drawing of the cone-beam X-ray source-based absorption-contrast set-up.

Clinical or laboratory-based X-ray imaging is performed mainly in absorption-contrast mode in a cone-beam configuration, as shown in Figure 2. X-rays propagate from the X-ray source to the detector. If the sample is positioned in between, it causes attenuation of the X-ray.

For the region in between absorption edges, the X-ray attenuation coefficient is dependent on the atomic number Z [26] and photon energy E

$$\mu \approx (\frac{Z}{E})^m, \tag{1.3}$$

where $m \subset (2.5...3.5)$.

Absorption-contrast imaging is successfully used in distinguishing between hard and soft tissues, or visualising materials consisting of a higher atomic number Z elements, such as Ca. For visualising soft materials in absorption contrast, staining agents are often used.

Phase-contrast imaging

Phase-contrast imaging was first demonstrated by Frits Zernike in 1930. In phase-contrast imaging, which relies on the phase shift caused by a medium, density contrast is related to the decrement $\delta(x, y, z)$. For soft materials, mainly consisting of a low atomic number Z elements, such as C, H, O and N, the magnitude of the refractive index decrement δ can be greater than the imaginary part β of the refractive index, up to three orders of magnitude [27]. Thus, hard X-ray imaging of soft tissues is preferentially performed in the phase-contrast mode [28, 29]. Medical applications can find phase imaging beneficial, as no contrast agent is required.

It is common for phase-contrast imaging techniques to transform phase shift caused by the sample into an intensity modulation that is recorded by the detector. Nowadays, there is a wide range of methodologies for phase-contrast imaging [27, 30, 31].

As a short overview, three main groups of phase imaging can be specified: (1) direct methods, for example Bonse-Hart crystal interferometry [32], (2) methods related to the second derivative, for example propagation-based imaging [33], and (3) methods related to the first derivative of phase shift, for example grating interferometry [34–38] or analyser-based imaging [39]. A more detailed treatment of the topic can be found elsewhere [26, 40].

Crystal interferometry

Crystal interferometry is a powerful, highly sensitive imaging method, firstly introduced by Ulrich Bonse and Michael Hart [32] more then half a century ago. In spite of its instrumental complexity, the method was optimised for clinical settings [29,41] and used to study a variety of soft tissues of human and animal origin. Nevertheless, the applicability of the methodology is limited to weakly absorbing materials with reduced sample size and require a highly mechanically stable system.

Propagation-based imaging

Propagation-based imaging (also called *in-line*) [33, 42–44] can be used to obtain quantitative phase images with superior instrumental simplicity, and so it is widely used at synchrotron radiation facilities worldwide. Data reconstruction can be performed based on algorithms of absorption tomography, albeit only in the edge-detection mode [45]. The most prominent application of the method is holotomography [45], as seen in Figure 3, where images are recorded at several object-to-detector distances, and in-line single distance tomography [46], where only one propagation distance is used.

In order to retrieve the phase maps in holotomography [45, 47], a set of radiographs at several object-to-detector distances at a given rotation angle is normalised with respect to the incoming beam, aligned and used in an adapted contrast transfer function (CTF) algorithm to determine the phase shift. Single distance phase recovery is performed successfully as well [48].

Three-dimensional holotomography imaging, similar to grating interferometry, yields a refractive index decrement, which is related to electron density distribution within the object. Thus, quantitative value. Nevertheless, holotomography data reconstruction is complex and the quantitative accuracy of values is lower, while experimental set-up is less complex and data acquisition is time-efficient, in comparison to grating interferometry [28].

The technique does not require highly monochromatic parallel-beam radiation, and so imaging can be performed using laboratory X-ray sources [44] and systems [49]. As no optical elements are required, the modality can provide extremely high spatial resolution.

Analyser-based imaging

Analyser-based imaging [39, 50–52] is a sensitive modality that can provide small-angle scattering and phase signals. Nevertheless, the method is limited to high brilliance systems.

Grating interferometry

X-ray grating interferometry [34, 36–38, 53] is successfully performed using synchrotron radiation [27, 35] and polychromatic X-ray tube sources [54–58] for quantitatively [43, 59–61] visualising soft and hard materials. For example, synchrotron radiation-based grating interferometry has enabled the identification of non-stained

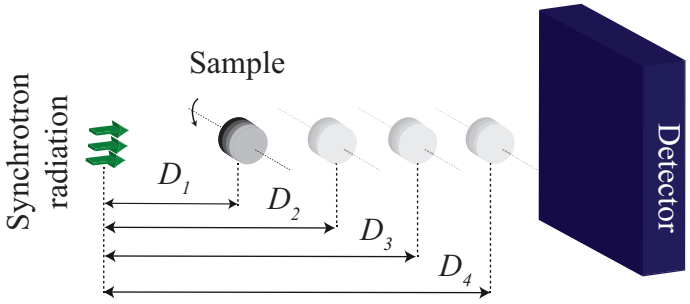

Figure 3: Schematic drawing of the holotomography phase-contrast set-up. Hotomography is a free-space propagation-based method, so no optical elements are positioned between the source and the detector. The images are acquired at selected distances and then numerically combined through holographic reconstruction. D1, D2, D3, D4: propagation distances.

Purkinje cells [62, 63] with sub-cellular details [64] and the detection of amyloid plaques [65].

In contrast to propagation-based imaging, grating interferometry requires additional component(s) positioned between the X-ray source and the detector. Grating interferometry is performed in one- [66–70] and two-grating (Talbot interferometer) configurations, even with microfocus X-ray sources [71]. The three-grating set-up works with conventional, low-brilliance X-ray laboratory sources [55, 72, 73]. Analysis of the data yields phase, absorption and small-angle scattering (dark-field) information simultaneously [74].

Grating interferometry is based on the detection of the deflection angles $\alpha(y, z)$ of the incident X-rays caused by the object. The deflection angle is directly related to the wavefront $\Phi(y, z)$

$$\alpha(y,z) = \frac{\lambda}{2\pi}\frac{\partial\Phi(y,z)}{\partial y} = \int_{-\infty}^{\infty}\frac{\partial\delta(x,y,z)}{\partial y}dx. \tag{1.4}$$

Grating set-up usually is operated using two gratings: beam-splitter grating G1 (mainly phase grating, though absorption gratings are also used) and analyser grating G2 (absorption grating). This type of interferometer is known as a *Talbot interferometer*, as shown in Figure 4a - b.

In the grating set-up, beam-splitter grating G1 induces a periodic spatial modulation in the X-ray wavefront. Downstream of G1, the periodic interference pattern is formed. Distortions in the wavefront, such as due to the object in the wave pass, lead to distortions in the intensity pattern.

The period of intensity fringes is usually very small, and so the detector is not able to resolve them directly. Therefore, the second grating G2, acting as a transmission mask, is often necessary.

In order to achieve optimal grating set-up efficiency, phase shift induced by the G1 should be $\pi/2$ or π [75].

For the parallel-beam geometry, see Figure 4a, the intensity pattern exhibits maximum or minimum contrast at certain distances along the optical axis, known as *Talbot distances*

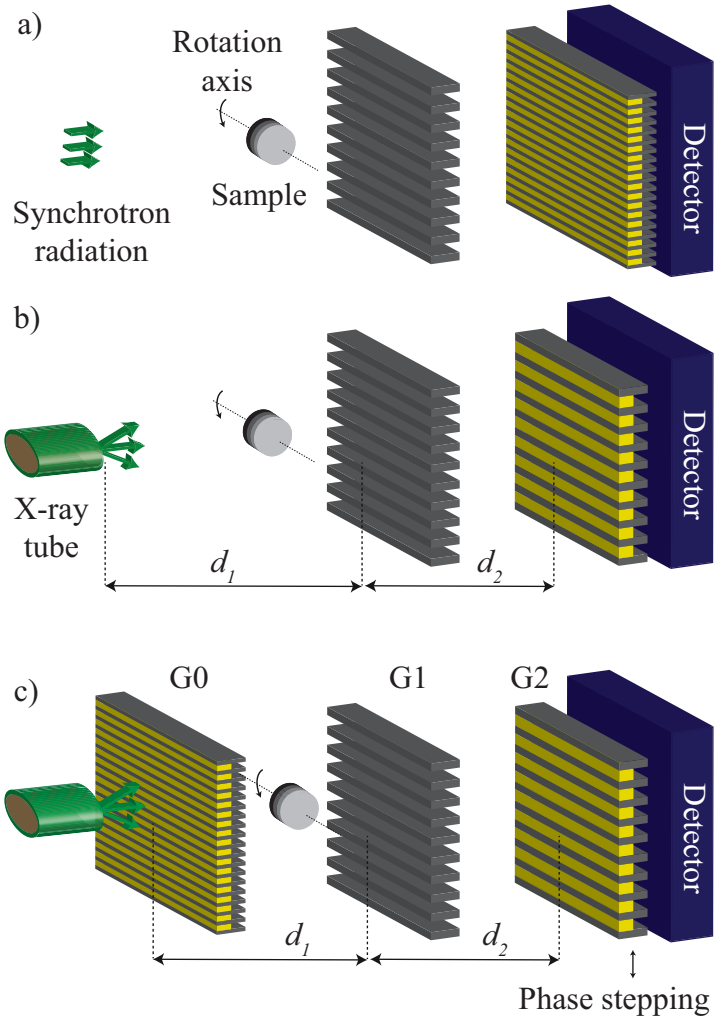

Figure 4: Schematic drawing of the parallel-beam synchrotron radiation-based (a) and cone-beam X-ray source-based (b) double-grating phase-contrast set-ups, and three-grating cone-beam X-ray source-based phase-contrast set-up. G0: source grating; G1: phase grating; G2: analyser grating; d_1: distance from the source to the phase grating G1; d_2: distance from the phase to the analyser grating G2.

$$d_m = \frac{1}{\eta^2}\frac{mp_1^2}{2\lambda}, \tag{1.5}$$

where λ is the wavelength of the incoming beam, p_1 the period of beam-splitter grating G_1 and m an integer ($m = 0, 1, 2, ...$) known as the *Talbot order*. When m is an odd number, contrast is at its maximum for phase grating, while when m is an even number, contrast reaches a maximum for amplitude grating. η is a coefficient that depends on the optical properties of beam-splitter grating G1.

If G1 is $\pi/2$-shifting grating

$$\eta_{\pi/2} = 1, p_2 = p_1, \tag{1.6}$$

where p_2 is the period of the analyser grating.

If G1 is π-shifting grating

$$\eta_{\pi} = 2, p_2 = p_1/2. \tag{1.7}$$

For cone-beam geometry, see Figure 4b, where radiation is not plane but spherical, magnification M needs to be considered as well

$$M = \frac{d_1}{d_1 - d_2}. \tag{1.8}$$

Thus, the Talbot distance becomes $d_m^* = M \cdot d_m$.

Fringe spacing, so the required period of the analyser grating is also influenced by magnification

$$p_2 = \frac{Mp_1}{\eta}. \tag{1.9}$$

Coherence requirements, in particular with respect to source size, can be easily met at synchrotron radiation facilities. However, fulfilling these requirements with laboratory X-ray sources is not trivial undertaking, so grating interferometry with a laboratory source is mainly performed in a modified configuration. In this case, addition grating, so called source grating G0, see Figure 4c, is introduced behind the X-ray source. In this configuration, the grating set-up is known as a *Talbot-Lau interferometer*. The period of the source grating p_0 should be properly chosen:

$$p_0 = \frac{d_2}{d_1}p_2. \tag{1.10}$$

Nonetheless, the introduction of source grating enables one to meet coherence requirements, flux decreases.

Relevance and aims

"*Knowing it and seeing it are two different things.*"
Suzanne Collins, Mockingja

To understand the brain´s properties and functionality at the most fundamental level, one must reveal and describe its structure down to the (sub-)cellular level. Three-dimensional characterisation of brain tissues is a challenge and the possibility of performing non-destructive 3D imaging with the reasonable sensitivity, resolution, data acquisition rate and quantitative information of a relatively large tissue volumes, especially within a laboratory environment, is of a great interest in a wide range of biomedical applications.

Almost since their discovery by Wilhelm Conrad Röntgen in 1895, X-rays have been used to image internal structures within objects. To date, a number of techniques have been successfully applied to image brain tissues and neuroscience has made a great progress in extracting previously inaccessible anatomical data. Conventional hard X-ray absorption-contrast imaging is used successfully for visualising features with higher density. Hard X-ray absorption-contrast imaging of weakly absorbing materials is usually performed by applying of contrast agents, although these treatments remain complex and time-consuming. On the other hand, visualising weakly absorbing materials is performed with significantly enhanced contrast in the phase mode, using highly brilliant radiation and conventional X-ray sources.

The aim of the present work was to find the most suitable, non-destructive 3D imaging approach with both reasonable density and spatial resolutions for visualising brain tissues. The ambitious challenge faced was to bridge the performance gap between the tomography data from laboratory systems, histological approaches employed by anatomists and pathologists, and synchrotron radiation-based tomography, by taking advantage of recent developments in X-ray tomographic imaging.

Outline

This cumulative thesis includes four publications, summarising the project´s main parts: (i) the use of the nanotom® m to visualise selected formalin-fixed paraffin-embedded brain tissues (*Chapter 2*), (ii) the incorporation of a double-grating interferometer into the nanotom® m for phase-contrast imaging (*Chapter 3*) and (iii) the nano-holotomography to reveal the nanoanatomy of selected brain tissues (*Chapter 4*).

Chapter 2 is divided into two sections: (i) the absorption-contrast laboratory-based micro computed tomography of human brain tissues and (ii) a qualitative comparison of absorption-contrast laboratory-based and phase-contrast synchrotron radiation-based tomography. The general aim of the study is to reveal individual cells within the human brain and to describe the three-dimensional structure on the cellular level. The idea was realised by using the hard X-ray µCT system nanotom® m and the successful results were demonstrated on a formalin-fixed paraffin-embedded human cerebellum specimen. It is illustrated that the contrast of the tomography data is comparable to conventional histological sections and almost comparable to synchrotron radiation-based phase-contrast tomography. Furthermore, a possibility to merge multi-modal complementary imaging techniques, namely histology and tomography, is presented. The proposed laboratory methodology is not only rewarding for the analysis of the human cerebellum, but it also has relevance for investigations into various tissue biopsies.

Chapter 3 describes the implementation of a double-grating interferometer for phase-contrast computed tomography in a conventional system nanotom® m. In this study, an X-ray double-grating interferometer is designed and installed at the µCT system nanotom® m. Qualitative and quantitative comparisons of the data acquired in phase- and absorption-contrast modes are performed. While both modes demonstrate accuracy while visualising bone, cartilage was only determined in the phase mode.

Chapter 4 discusses the investigation of the human brain nanoanatomy with synchrotron radiation-based hard X-ray phase-contrast nano-holotomography at the ID16A-NI nano-imaging beamline with pixel sizes down to 25 nm. Using a neocortex block imaged with an effective pixel size of 50 nm, the study demonstrates the fully automatic segmentation of pyramidal cells. The advanced software (VGStudio MAX 2.0, Volume Graphics, Heidelberg, Germany) allows for semi-automatic segmenting sub-cellular structures, including nuclear membrane and nucleoli.

The thesis is completed by a conclusion and an outlook on future research in *Chapter 5*.

Contributors

In order to achieve the desired results, the content of the *Chapters 2 - 4* was developed within the framework of strong cooperation with a multi-disciplinary team. Although the main work was done by the author of the present thesis (A.K.), experienced scientists and medical doctors made the valuable contributions, namely, Prof. Dr. Bert Müller (B.M.), Dr. Simone E. Hieber (S.E.H.), Dr. Georg Schulz (Ge.S.), Dr. Christos Bikis (C.B.), Natalia Chicherova (N.C.), Peter Thalmann (P.T.), Dr. Hans Deyhle (H.D), Gabriel Schweighauser (Ga.S.), Dr. Jürgen Hench (J.H.), Dr. Stephan Frank (S.F.), Dr. Irene Zanette (I.Z.), Marie-Christine Zdora (M.-C.Z.), Dr. Alexander Hipp (A.H.), Dr. Alexandra Pacureanu (A.P.), Prof. Dr. Magdalena Müller-Gerbl (M.M.-G.) and Dr. Peter Cloetens (P.C).

A.K. made substantial creative contributions in the following phases of the work: the study design and implementation, conducting the experiments, data analysis, figure preparation and writing the manuscripts.

In the following, the contributions of the co-authors are listed for each chapter. The authors' order is equivalent to the order in the published or submitted articles. All authors discussed the results, contributed to the final manuscript and performed critical reviews of the related manuscripts.

Chapter 2 Section 1:

H.D.:	Assistance with the data interpretation and figure preparation.
Ge.S.:	Assistance with the study design. Assistance with the data acquisition. Suggestions for the data interpretation and figure preparation.
Ga.S.:	The specimen preparation. Prepared the histological sections. Assistance with writing the "Materials and Methods" section.
J.H.:	Initiated the study concept. Critical reviewing of the manuscript for content. Assistance with writing the "Materials and Methods" section.
N.C.:	Automatically registered the histological sections to the CT data. Assistance with writing the "Materials and Methods" section.
C.B.:	Prepared the histological sections. Assistance with writing the "Materials and Methods" section.
S.E.H.:	Initiation of the study and main contribution to the specimen preparation. Suggestions for the graphical representation of figures.
B.M.:	Initiation of the study. Assistance with the study design. Assistance with the writing of the "Introduction" and "Results and Discussion" sections. Critical reviewing of the manuscript for content. Suggestions for the graphical representation of figures.

Chapter 2 Section 2:

Ge.S.:	Assistance with the study design. Assistance with the data acquisition. Suggestions for the data interpretation and reconstruction.
H.D.:	Assistance with the data acquisition.
P.T.:	Assistance with the data registration.
I.Z.:	Assistance with the data acquisition.
M.-C.: Z.	Assistance with the data acquisition.
C.B.:	Prepared the histological sections.

A.H.:	Assistance with the data acquisition.
S.E.H.:	Initiation of the study and main contribution to the specimen preparation. Suggestions for the graphical representation of figures.
Ga.S.:	The specimen preparation. Prepared the histological sections.
J.H.:	Critical reviewing of the manuscript for content.
B.M.:	Initiation of the study. Assistance with the study design. Assistance with the preparation of the specimen. Critical reviewing of the manuscript for content. Suggestions for the graphical representation of figures.

Chapter 3:

Ge.S.:	Initiation of the study. Assistance with the study design. Suggestions and assistance for the data acquisition, reconstruction and interpretation. Suggestions for the graphical representation of figures.
P.T.:	Assistance with the data acquisition, reconstruction and registration.
B.M.:	Initiation of the study. Assistance with the study design. Critical reviewing of the manuscript for content. Suggestions for the graphical representation of figures.

Chapter 4:

C.B.:	Assistance with the specimen preparation. Assistance with the data acquisition. Preparation of the histological sections.
A.P.:	Assistance with the data acquisition and reconstruction. Assistance with writing the "Materials and Methods" section.
S.E.H.:	Suggestions for the graphical representation of figures. Assistance with the data segmentation.
P.T.:	Assistance with the data registration.
H.D.:	Assistance with the data acquisition.
Ga.S.:	Assistance with the specimen preparation. Prepared the histological sections.
J.H.:	Critical reviewing of the manuscript.
S.F.:	Critical reviewing of the manuscript.
M.M.-G.:	Assistance with the specimen preparation.
Ge.S.:	Assisted the study initialisation. Assistance with the study design. Assistance with the data acquisition. Suggestions and assistance for the data interpretation and figure preparation.
P.C.:	Assistance with the data acquisition and reconstruction.
B.M.:	Initiation of the study. Assistance with the study design. Assistance with writing of the "Introduction" and "Results and Discussion" sections. Critical reviewing of the manuscript for content. Suggestions for the graphical representation of figures.

Chapter 2

Visualising individual cells within the human brain

Extending two-dimensional histology into the third dimension through conventional micro computed tomography

A. Khimchenko, H. Deyhle, G. Schulz, G. Schweighauser, J. Hench, N. Chicherova, C. Bikis, S. E. Hieber, B. Müller,

NeuroImage 139, 26-36 (2016)
(doi:10.1016/j.neuroimage.2016.06.005)

NeuroImage 139 (2016) 26–36

Contents lists available at ScienceDirect

NeuroImage

journal homepage: www.elsevier.com/locate/ynimg

Extending two-dimensional histology into the third dimension through conventional micro computed tomography

Anna Khimchenko [a], Hans Deyhle [a], Georg Schulz [a], Gabriel Schweighauser [c], Jürgen Hench [c], Natalia Chicherova [a,b], Christos Bikis [a], Simone E. Hieber [a], Bert Müller [a,*]

[a] Biomaterials Science Center, Department of Biomedical Engineering, University of Basel, Allschwil, Switzerland
[b] Medical Image Analysis Center, Department of Biomedical Engineering, University of Basel, Allschwil, Switzerland
[c] Institute of Pathology, Department of Neuropathology, Basel University Hospital, Basel, Switzerland

ARTICLE INFO

Article history:
Received 7 March 2016
Revised 11 May 2016
Accepted 4 June 2016
Available online 14 June 2016

Keywords:
Hard X-ray tomography
Nano-focus X-ray
Histology
2D-3D image registration
Paraffin-embedded human cerebellum
Purkinje cells
Joint histogram analysis

ABSTRACT

Histological examination achieves sub-micrometer resolution laterally. In the third dimension, however, resolution is limited to section thickness. In addition, histological sectioning and mounting sections on glass slides introduce tissue-dependent stress and strain. In contrast, state-of-the-art hard X-ray micro computed tomography (μCT) systems provide isotropic sub-micrometer resolution and avoid sectioning artefacts. The drawback of μCT in the absorption contrast mode for visualising physically soft tissue is a low attenuation difference between anatomical features. In this communication, we demonstrate that formalin-fixed paraffin-embedded human cerebellum yields appropriate absorption contrast in laboratory-based μCT data, comparable to conventional histological sections. Purkinje cells, for example, are readily visible. In order to investigate the pros and cons of complementary approaches, two- and three-dimensional data were manually and automatically registered. The joint histogram of histology and the related μCT slice allows for a detailed discussion on how to integrate two-dimensional information from histology into a three-dimensional tomography dataset. This methodology is not only rewarding for the analysis of the human cerebellum, but it also has relevance for investigations of tissue biopsies and post-mortem applications. Our data indicate that laboratory-based μCT as a modality can fill the gap between synchrotron radiation-based μCT and histology for a variety of tissues. As the information from haematoxylin and eosin (H&E) stained sections and μCT data is related, one can colourise local X-ray absorption values according to the H&E stain. Hence, μCT data can correlate and virtually extend two-dimensional (2D) histology data into the third dimension.

Introduction

The microanatomy, i.e. microstructures and morphology, of tissue components is generally characterised by means of histological sectioning, as this sort of examination can provide a true (sub-)micrometer resolution in two lateral dimensions, when neglecting processing-derived shrinkage artefacts, and the option of functional staining for the contrast (Müller et al., 2006; Irshad et al., 2014). By means of optical microscopy individual intra- and extracellular components are visualised (Irshad et al., 2014; Kandel et al., 2012; Fuchs and Buhmann, 2011). Currently established protocols, however, are often time-consuming, and individual steps involved in the preparation procedure induce stress- and strain-related artefacts in the tissue (Schulz et al., 2010a; Müller et al., 2012; Germann et al., 2008). Moreover, for histological examinations, the tissue has to be irreversibly cut into slices (Lang et al., 2014). As the sections are a few micrometers thick, isotropic lateral resolution is lost in the third dimension. Therefore, non-destructive three-dimensional imaging is a promising complement to provide volumetric morphological information (Schulz et al., 2010a).

Confocal microscopy yields images of cells in layers well below the surface. However, the limited transmission of visible light does not allow for the comprehensive visualisation of human tissue in its three-dimensional (3D) state (Müller et al., 2006). Multiphoton fluorescence in general and one- or two-photon microscopy (Wolf et al., 2015) in particular can provide information from tissue layers up to hundreds of micrometers, while decreasing the spatial resolution (So, 2002), for example in zebrafish larval brain (Vladimirov et al., 2014). Tissue-clearing methods significantly increase the accessible depth (Richardson and Lichtman, 2015). For example, tissue-transformation method CLARITY can increase the achievable imaging depth up to 5 or even 6 mm (Chung et al., 2013). The SWITCH method improves the light penetration as well, demonstrating clearing of a whole adult

* Corresponding author at: Biomaterials Science Center, Department of Biomedical Engineering, University of Basel, Gewerbestrasse 14, 4123 Allschwil, Switzerland.
E-mail address: bert.mueller@unibas.ch (B. Müller).

http://dx.doi.org/10.1016/j.neuroimage.2016.06.005
1053-8119/

mouse brain, lung, kidney, heart, liver and spinal cord with a required tissue-clearing time between five and ten days (Murray et al., 2015). Combining tissue clearing with confocal light sheet and light sheet fluorescence microscopy allows for the visualisation of entire mouse brains (Dodt et al., 2007; Silvestri et al., 2012; Costantini et al., 2015). Nevertheless, these procedures are often technically demanding, expensive, time-consuming, induce significant tissue deformation, and restricted to a particular tissue type with sizes not exceeding a thickness of some millimeters.

Another means of obtaining 3D morphology is serial sectioning, which is time-consuming and is mainly applied to small tissue volumes (Chung et al., 2013). The time restriction can be overcome by applying a serial optical coherence scanner (Wang et al., 2014), albeit spatial resolution in the third dimension still remains restricted to section thickness (Lang et al., 2014; Schulz et al., 2010a). Nonetheless, these methods are destructive and the same sample can often not be reused for subsequent examinations.

Synchrotron radiation-based micro and nano computed tomography (SRμCT) provides impressive 3D images of biological tissues on a (sub-)cellular level (Zehbe et al., 2010; Huang et al., 2015). For example, one can detect and image RNA/DNA-stained HEK 293 cell clusters (Müller et al., 2006), intracellular structures of dehydrated human cells (Guk et al., 2008), single endothelial cells labelled with iron oxide particles (Thimm et al., 2012), chondrocytes within the extracellular matrix of articular cartilages without metal staining (Zehbe et al., 2015), the lacuno-canalicular network and collagen fibres in human bone (Langer et al., 2012), osmium-stained individual ganglion cells (Lareida et al., 2009), unstained Purkinje cells (Schulz et al., 2010b) and freeze-dried neurons (Mokso et al., 2007). The limited accessibility of synchrotron radiation facilities, though, imposes severe restrictions on the user (Wenz et al., 2015).

In contrast to laboratory sources, the synchrotron radiation sources yield such a high photon flux, that a monochromator can be incorporated to pass about 10^{-4} of the photons and generate monochromatic light, avoiding beam hardening. Laboratory-based μCT systems have successfully been employed for 3D visualisation of higher density materials (Chappard et al., 2005; Blouin et al., 2006) and stained tissues (Metscher, 2009; de Crespigny et al., 2008; Ribi et al., 2008; Ashton et al., 2015). Recently μCT was successfully used for analysis of brain architecture of insect species (Sombke et al., 2015). Furthermore, μCT can achieve superb resolution, although performance for lower density materials is restricted due to limited contrast.

Consequently, we state that there is a paucity of methods to study the microstructure and morphology of large tissue components in 3D space with isotropic (sub-)cellular spatial resolution within a laboratory environment.

In this study, we evaluate the contrast of formalin-fixed paraffin-embedded (FFPE) tissue obtained with laboratory-based μCT. We aim to demonstrate the three-dimensional non-destructive visualisation of a human cerebellum sample with cellular resolution, with phoenix|xray nanotom® m laboratory-based μCT system.

In order to directly compare three-dimensional μCT data with histology, the counterpart of the histological section has to be localised within the three-dimensional μCT dataset (Stalder et al., 2014). Such registration enables the validation of structures within the μCT data by selected histological sections (Gambichler et al., 2007).

It was shown that synchrotron radiation-based computed tomography, using the phase-contrast mode, allows for identifying not only major blood vessels, but also *Stratum moleculare*, *Stratum granulosum* and white matter within formalin-fixed human cerebellum - even individual Purkinje cells are visualised (Schulz et al., 2010b). The question arises as to whether laboratory-based absorption-contrast μCT of an FFPE human cerebellum sample can provide comparable results. We investigate how μCT could become a complementary method to the microscopic examination of stained tissue slices, thereby extending its applicability to three-dimensional features.

Materials and methods

Tissue preparation

The specimen was extracted from the donated cadaveric brain of a 73-year-old man. Written consent for scientific use was documented. All procedures were conducted in accordance with the Declaration of Helsinki and approved by the Ethikkommission Nordwestschweiz. The brain was fixed in 4% histological-grade buffered formalin for two weeks prior to dissection. Tissue samples for histological work-up were excised by a scalpel. These specimens, approximately 15 mm × 15 mm × 4 mm, to fit into conventional histological embedding cassettes, were dehydrated and paraffin embedded according to surgical pathology procedures: 3× 1 h in 70% ethanol (EtOH) in H_2O (v/v), 1 h in 80% EtOH in H_2O (v/v), 2× 1 h in 96% EtOH in H_2O (v/v), 2× 1 h 100% xylene followed by 3× 1 h paraffin/plastic mixture (Surgipath Paraplast ®, Leica Biosystems, Switzerland) at 60 °C. Next, samples within the molten paraffin were transferred to histological embedding moulds on a routine paraffin block-casting device. Here, the paraffin was cooled down to approximately −8 °C, to solidify and then removed from the casting moulds. Cylinders 6 mm in diameter were extracted from the FFPE tissue, using a metal punch, for μCT measurements. Typically, minimum formaldehyde fixation time is one hour, paraffin embedding takes approximately ten hours, casting blocks five minutes and punching five minutes.

Data acquisition and processing

The tomography experiments were carried out using the absorption-contrast μCT system nanotom® m (phoenix|x-ray, GE Sensing & Inspection Technologies GmbH, Wunstorf, Germany) equipped with a 180 kV–15 W high-power nano-focus® tube with W and Mo transmission targets (General Electric, Measurement and Control, 2014; Egbert and Brunke, 2011). The nanotom® m μCT-system allows measuring objects with up to 25 cm in diameter and height.

The μCT was performed with a voxel length of 3.5 μm^3 and a field of view of about 8.5 × 10.5 mm^2. For each acquisition, 1900 projections were recorded over 360°. Geometric magnification M was maintained at 28.57 for selected focus-detector distances (FDD) and focus-object distances (FOD): M = FDD/FOD. Measurements were taken in the tube operation mode "0" with an estimated source size of 2.7 μm.

Data acquisition and reconstruction were performed with datos|x 2.0 software (phoenix|x-ray, GE Sensing & Inspection Technologies GmbH, Wunstorf, Germany). The average data acquisition time was 3.5 h, with the requirement of the user interaction in the beginning of the scan followed by the automated execution. Data reconstruction is based on Feldkamps cone beam reconstruction algorithm (Egbert and Brunke, 2011; Feldkamp et al., 1984) and can be automatically done within less than 15 min. The reconstructed slices were scaled from black to white within the range of three times the distance from the maximum to the minimum histogram peak position for each dataset.

The reconstructed datasets were compared for their contrast-to-noise ratio:

$$CNR = \frac{|I_1 - I_2|}{\sqrt{\sigma_1^2 + \sigma_2^2}} \quad (1)$$

where I_1 and I_2 indicate the mean intensities of homogeneous components within the specimen, and σ_1 and σ_2 the standard deviations. To this end, volumes of interest (VOI) were selected within the white matter (VOI = 18.200 voxels), *Stratum granulosum* (VOI = 5292 voxels), *Stratum moleculare* (VOI = 4032 voxels), and paraffin (VOI = 4704 voxels) of each dataset. To ensure comparability of the *CNR* values, VOIs were selected from the same location within each dataset.

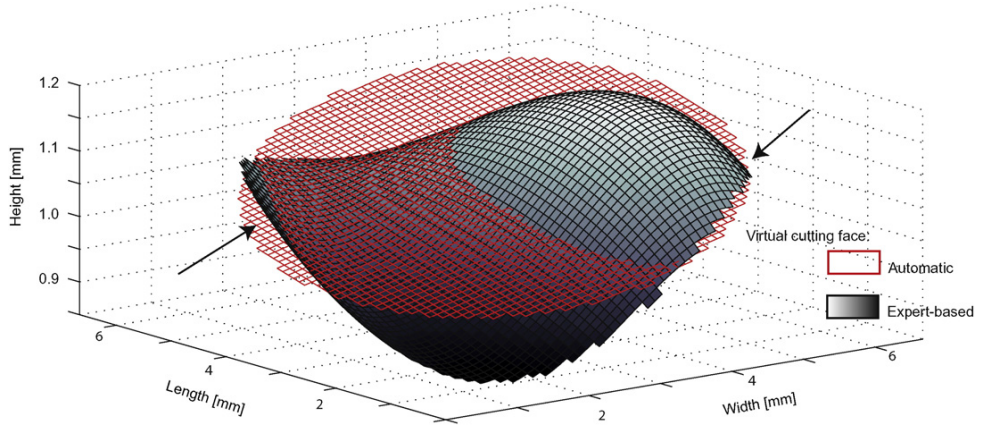

Fig. 1. Shape of the histological section in the tomography dataset based on the expert-based (black) and automatic (red) registrations. Note that automatic registration yields a plane, while manual registration allows for curved surfaces. Arrows indicate regions of low landmark density.

Reconstructed data were filtered using VGStudio MAX 2.0 (Volume Graphics, Heidelberg, Germany) for noise reduction (median filter size "5" followed by an adaptive Gauss filter with smoothing "0.1" and an edge threshold "1") for comparison with histology.

Histology

Subsequent to the laboratory-based μCT measurements, the specimen was investigated by means of histology. The paraffin cylinder was re-embedded in a standard histological paraffin block by melting it, placing the tissue cylinder into a mould and filling it up with fresh paraffin. Sections of 4 μm thickness were cut using a microtome, mounted on glass slides, and stained with haematoxylin and eosin (H&E). The preparation time ranged from 30 to 60 s per slide.

Images of the resulting slides were taken on a light microscope and resulted in pixel sizes of 6.99 μm and 4.38 μm. These pixel sizes were selected to match the μCT data. The resolution of computed tomography depends on several factors including the source spot size due to focal spot blurring effect, noise on a detector and beam instability and is normally within the range of 1.5 to 2.0 pixel sizes. Under such estimation, resolutions of the selected histological section and tomography slice are comparable. Micrographs acquired with a slide scanner (Olympus® VS120 Virtual Slide Microscope, Japan) reached 0.35 μm pixel size.

A histological photograph with a pixel size of 6.99 μm was used for the quantitative comparison to the tomography slice. For comparison, the histological section was grey-scaled and colour-inverted to provide grey-value correlation to the tomography data.

Data registration

To locate the histological slide within the μCT data, 2D-3D registration was performed (Chicherova et al., 2014). First, corresponding feature points between the histological image and each image in the μCT volume were identified using the key-point detector SURF (Bay et al., 2008). The coordinates of the matching points of the μCT images were stored in a 3D space. Second, the points were filtered according to their density. Weights to each of the points in the 3D cloud were assigned based on their neighborhood. The 500 points with the highest weights were selected. Finally, a plane was fitted into the filtered 3D cloud using the modified model-fitting algorithm RANSAC (Fischler and Bolles, 1981). The

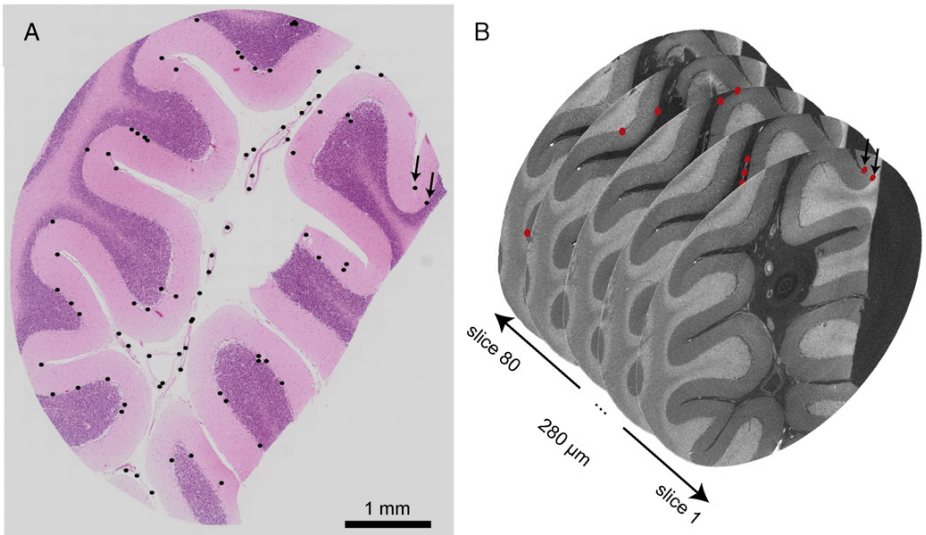

Fig. 2. Visualisation of characteristic landmarks for manual 2D-3D registration marked in a selected histological section (A) and in the μCT dataset (B). Characteristic landmarks of one histological section are spread over 80 consecutive μCT slices.

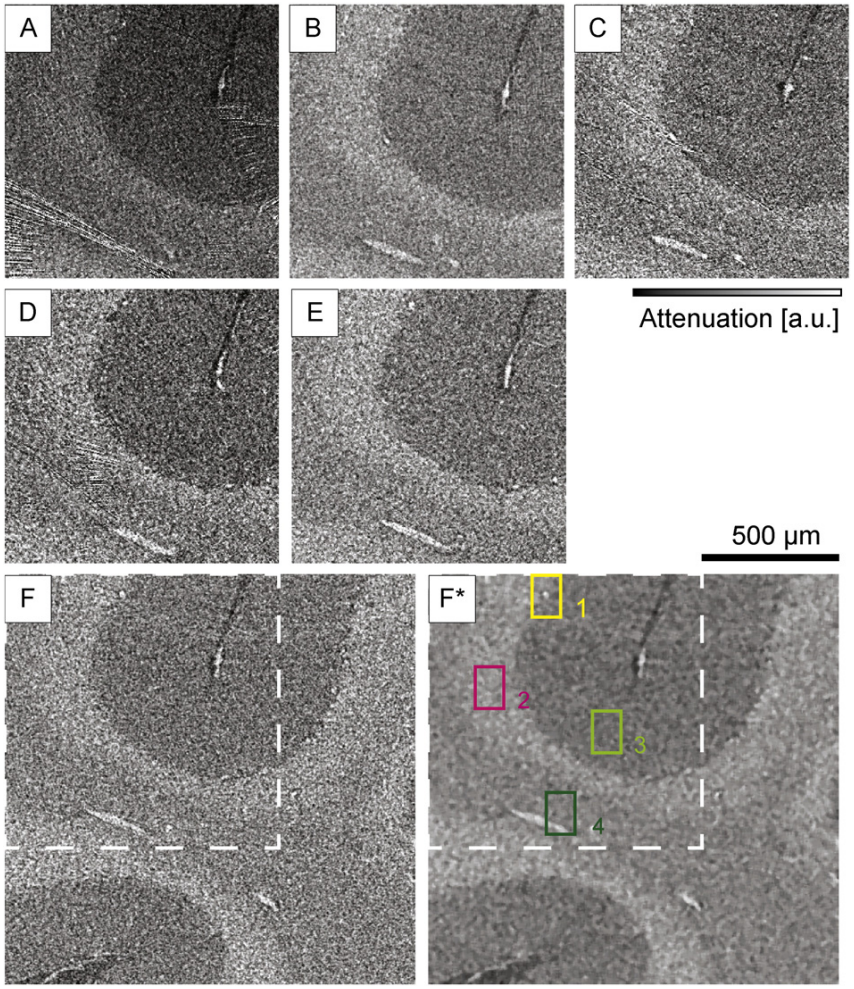

Fig. 3. Human cerebellum block measured with six µCT settings. Images provide sufficient contrast for visualising morphological features. As the images are dominated by noise, filtering is required. A–F: selected part of the tomographic slice recorded with parameters summarised in Table 1. F*: Slice F filtered for noise reduction. 1 (yellow): Purkinje cell, 2 (pink): *Stratum granulosum*, 3 (light green): *Stratum moleculare*, 4 (dark green): blood vessel within the white matter.

corresponding tomogram is then interpolated from the µCT volume using the obtained coordinates of the plane, see Fig. 1. After matching the histological slide in the tomogram, we registered the histology section and correlated tomography slice in 2D, using the Demon registration tool (Kroon and Slump, 2009) with affine transformation constraint. In the present study, the histological slides show only gradually varying local deformations. Therefore, one may conclude that the affine transformation is sufficiently precise to accurately register histology slide with µCT slice. We took the histological section as the reference, due to its higher spatial resolution, and the tomographic slice as the floating image. The entire pipeline was written in Matlab R2014a (MathWorks, Natick, USA).

To validate automatic registration, an expert-based 2D-3D registration was performed. The registration was based on the point-to-point correspondence of anatomical landmarks located in tomography data and

Table 1
Selection of the optimized settings: Scanning parameters of the nanotom® m used for the µCT experiments and contrast-to-noise ratios (CNRs) of the reconstructed data. *Target*: X-ray tube transmission target, *U*: acceleration voltage, *I*: e-beam current, FDD: focus-detector distance, FOD: focus-object distance, *t*: exposure time per projection, CNR(1): contrast-to-noise ratio between paraffin and *Stratum moleculare*; CNR(2): contrast-to-noise ratio between paraffin and white matter; CNR(3): contrast-to-noise ratio between paraffin and *Stratum granulosum*.

Setting	Target	*U* [kV]	*I* [µA]	FDD [mm]	FOD [mm]	*t* [s]	CNR (*I*)	CNR (*II*)	CNR (*III*)
A	Mo	40	230	285.69	9.99	7	0.02 ± 0.07	1.26 ± 0.07	1.42 ± 0.07
B	W	40	350	285.69	9.99	6	0.88 ± 0.20	1.35 ± 0.21	1.91 ± 0.23
C	W	40	350	399.99	13.99	12	0.44 ± 0.09	0.87 ± 0.09	1.28 ± 0.09
D	Mo	50	180	285.69	9.99	7	0.31 ± 0.07	0.70 ± 0.07	1.11 ± 0.07
E	Mo	60	150	285.69	9.99	3	0.68 ± 0.06	1.01 ± 0.06	1.45 ± 0.07
F	W	60	350	285.69	9.99	3	0.70 ± 0.10	1.11 ± 0.17	1.57 ± 0.18

histology images (Markelj et al., 2012) (see Fig. 2). For this purpose, characteristic vessels, cell groups and cracks seen in both datasets were matched in four histological sections. The manually identified landmarks in the tomography data were then fitted with a 2D polynomial surface (see Fig. 1), using the Curve Fitting Toolbox™ implemented in Matlab R2014a. This surface was considered to correspond to the location of the histological section in the 3D data. 2D-2D affine post-registration of the histological section and its tomographic counterpart was performed in a manner similar to that used for automatic registration.

Volume ratio calculation

The volume ratio (VRs) of structures of interest was calculated, defined as: $VR = V_1/V_2$,

where V_1 and V_2 indicate the volume/area occupied by structures of interest within the sample in voxels/pixels. We calculated the surface area (in pixels) occupied by *Stratum moleculare*/white matter and *Stratum granulosum* for the registered tomographic volume (*), and the selected histological section and tomographic slice. The surface area was extracted from histogram based segmentation (Manjon-Herrera, 2006).

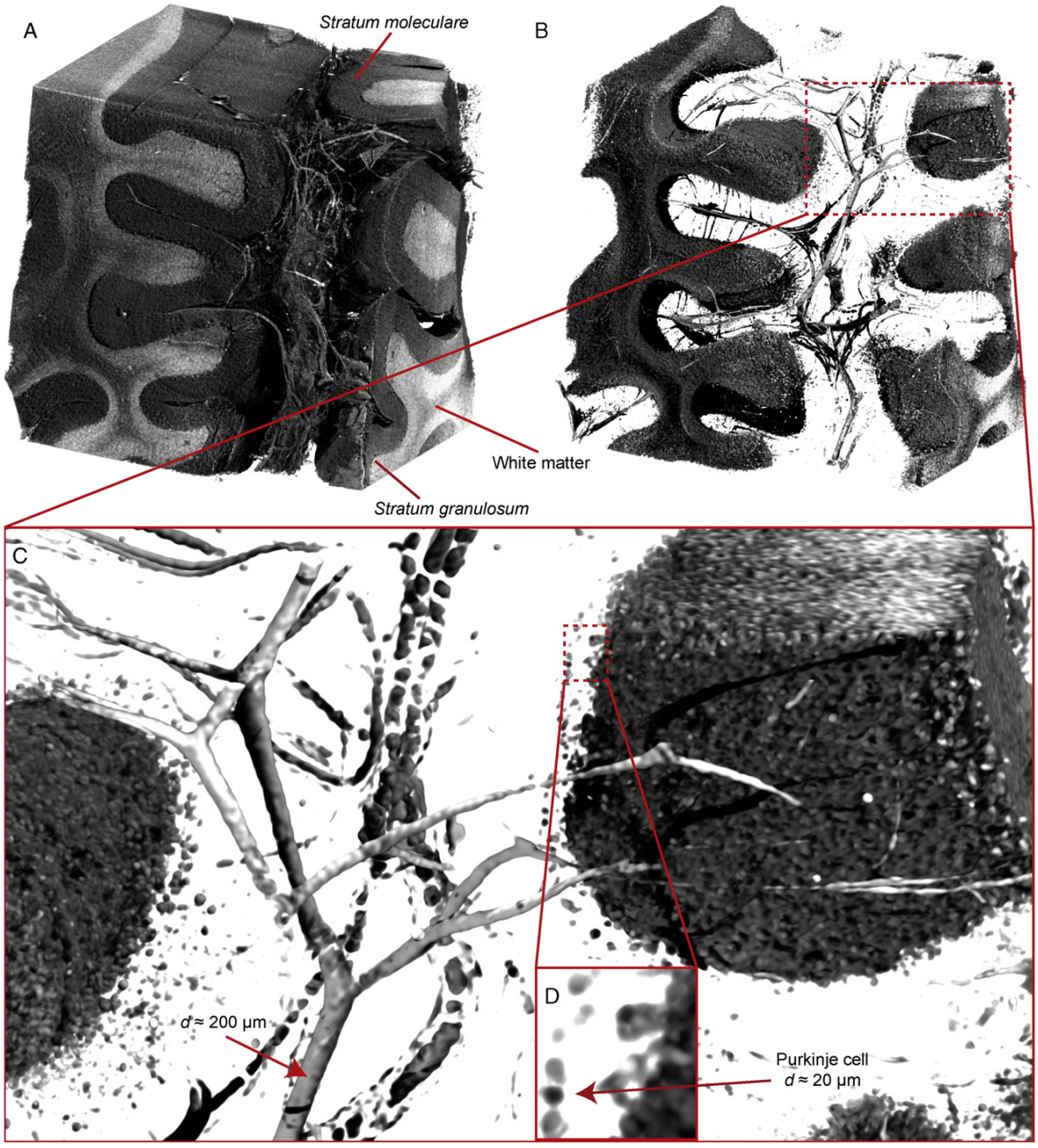

Fig. 4. The 3D-rendering of the human cerebellum block based on the filtered µCT data (A) shows blood vessels of various sizes, *Stratum moleculare*, *Stratum granulosum*, and white matter. Intensity thresholding (B) enables the exclusion of *Stratum moleculare* for an improved visualisation of the blood vessels and Purkinje cells (C, D).

In order to calculate the volume ratio for 3D data, cumulative slice-wise calculation was carried out.

Histogram analysis

The quantitative comparison of histology and tomography was based on the histogram analysis of the selected registered slices.

For the quantitative analysis of the registered μCT and histology slices, the grey value histograms of the corresponding 2D images were fitted with multi-Gaussian distributions (Müller et al., 2002), using the Levenberg-Marquardt algorithm of OriginPro 7.5 (OriginLab Corporation, Northampton, USA) (Schulz et al., 2010b, 2012). This common approach supports the intensity-based segmentation. The Gaussian shape of the peaks results from the limited photon statistics (Beckmann et al., 2008).

Results

Parameter selection for optimized tomography

Fig. 3 presents parts of μCT slices acquired with the parameters summarised in Table 1. The slices in Fig. 3 are cropped around the region occupied by three structures of interest. Visual inspection reveals that *Stratum granulosum* (2, pink), *Stratum moleculare* (3, light green), individual cells (1, yellow), and blood vessels within the white matter (4, dark green) can be recognized. Images obtained with increased FDD have significant artefacts, resulting in a radial grey-value gradient. Since the μCT raw data comprises noise, filtering is essential for feature extraction. The impact of filtering can for example be recognized comparing the images in Fig. 3 F and F*.

The reconstructed datasets, recorded with the parameters summarised in Table 1, were compared for their contrast-to-noise ratio. The highest *CNR* for the selected anatomical features was achieved for scans B and F, and differences between the scans are within the confidence interval. Even though the *CNR* for scan B is higher than for scan F by trend, data from scan F was filtered and used for further analysis, since the acquisition time was approximately 2.5 h and was half that of scan B.

The 3D-rendering of filtered μCT data in Fig. 4 shows the 3D microarchitecture of the selected part of the FFPE human cerebellum. It is illustrated that the morphology of the human tissue sample can be investigated using laboratory-based μCT on a cellular level, without applying contrast agents. After filtering and intensity thresholding, segmentation allows for precise discrimination of *Stratum moleculare* and *Stratum granulosum*. The diameters of the vessel in Fig. 4 C and Purkinje cell in Fig. 4 D were estimated based on the number of voxels in the related orthogonal cutting plane manually.

Retrieval of histology slice in μCT data

An established technique to investigate anatomical structures is histology. Based on size, location, and shape one could reasonably assume that the elliptically shaped features in the μCT data correspond to the Purkinje cells. The four histology slides validated this assumption in 2D.

The polynomial surface fit provides reasonable results in regions of high landmark point density; however, it diverges quickly outside these regions. Regions presenting a limited number, or absence of, landmarks are comparatively small. Thus, these differences are not pronounced, and the visual quality of the registration is preserved. For example, in regions labelled with an arrow in Fig. 1, the surface has a steep slope, and the fitting quality deteriorates. However, this deviation is limited to the homogeneous border regions of the slice. The slopes of our virtual histology sections are more prominent in regions of low landmark density, e.g. in a homogeneous middle background part that does not have any features in the histological section (see Fig. 5, G and H central parts).

Manual 2D-3D registration of a single histological slide to μCT volume is highly time consuming process that lasts up to 8 h for

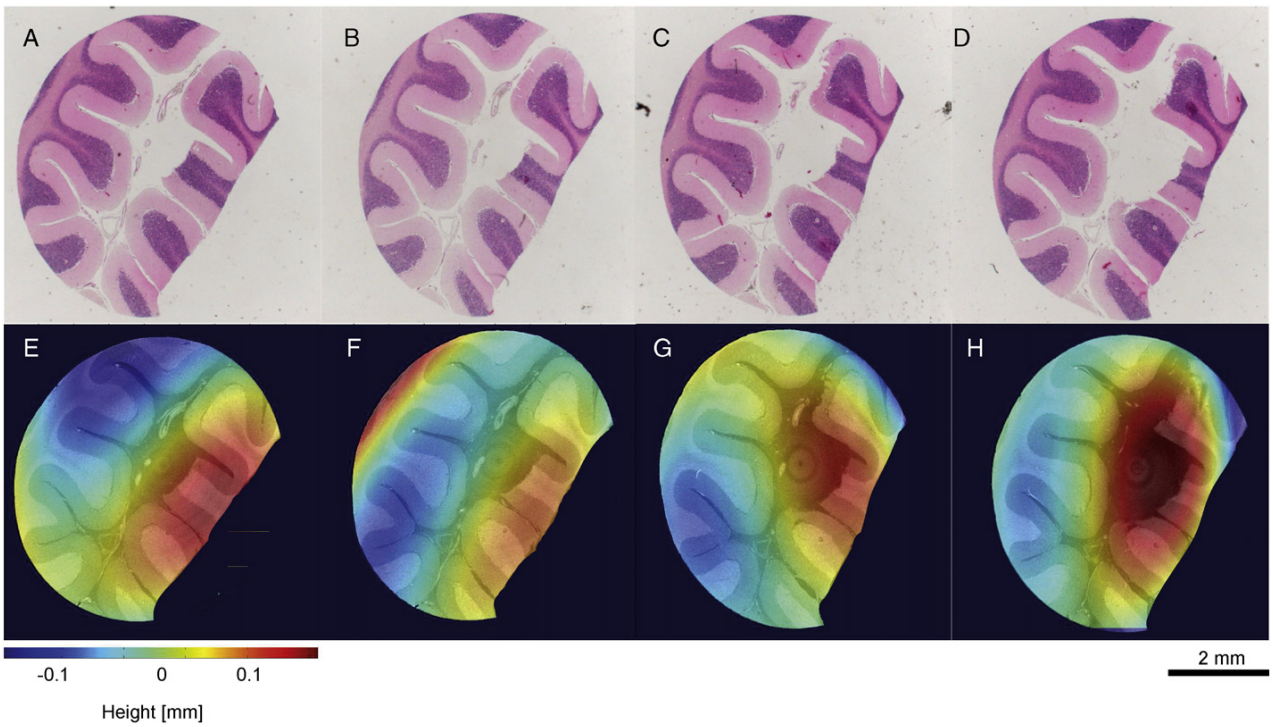

Fig. 5. Virtual cutting planes within the μCT volume visualising the position of the histological sections. The colour on top of the registered μCT slices (E–H) indicates the shape of the histological sections (A–D) in the tomography dataset based on the expert-based registration.

identification of point-to-point correspondence of anatomical landmarks. Thus, manual registration was done only for validation purposes. Precision of the automatic 2D-3D registration can be also deduced from Fig. 6, if one considers the expert-based registration as ground truth. Mean difference between manual and automatic registrations planes is 4 μm.

The characteristic landmarks used for the expert-based 2D-3D registration are distributed over 80 tomographic slices (see Fig. 2), which results in a height difference of 280 over a 6 mm sample diameter. Thus, the tilting angle corresponds to 2.6°. The tilting angle for the virtual cutting plane based on automatic registration is around 3°, while the maximal tilting angle for the histological cut is 5° and estimated at around 1° to 3°, therefore being in agreement with our findings.

To evaluate distortions in the selected histological slide, an additional 2D-2D registration with the tomographic slice as the reference and the histological section as the floating image was performed. A comparison of uncorrected and corrected histological sections enables one to conclude that radial stretching by approximately 6% and longitudinal stretching by approximately 15% have taken place.

Comparison of tomography and light microscopy-based imaging of histological sections

Fig. 6 displays the human cerebellum, with manually (left) and automatically (right) registered tomography slices compared to the selected high resolution histological section with a pixel size of 0.34 μm (middle) at three magnification strengths. Reasonable agreement between the registration approaches and histology is found. Manual registration validates the automatic approach on the macroscopic level (top row) in terms of tissue layer boundaries and bigger blood vessels. On the mesoscopic level (middle row) the difference between the registration methods becomes more pronounced, thus highlighting the differences between smaller vessels and groups of cells. On the microscopic level (bottom) one may clearly appreciate that automatic registration does not account for feature correspondence down to the true micrometer level, as cell correspondence is not preserved. To preserve the microscopic level of correspondence between tomography and histology, further quantitative comparison was based on the results of the expert-based registration.

Fig. 7 shows the histograms (left and top) of the single expert-based registered histological section and tomographic slice (right) along with

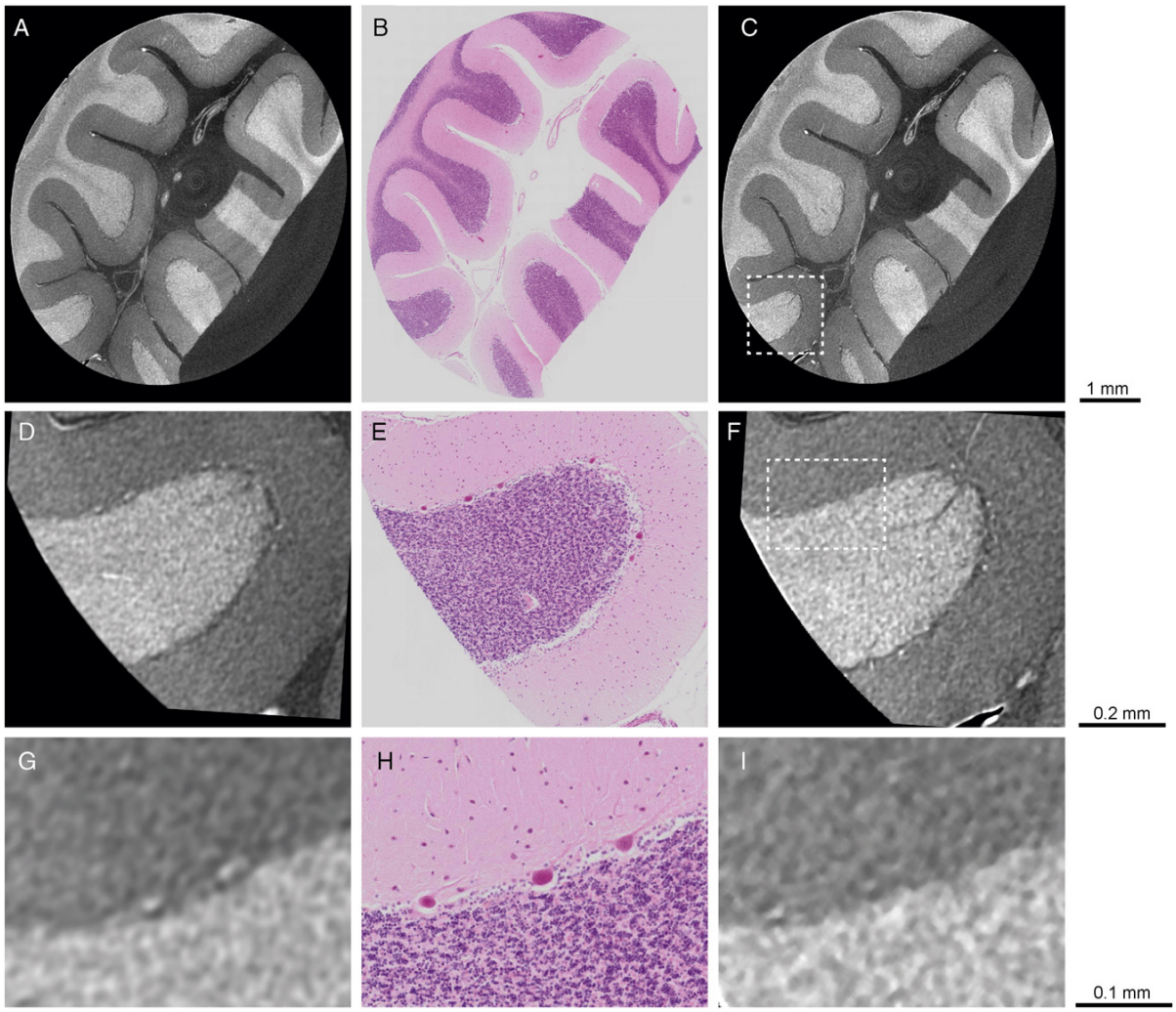

Fig. 6. Validation of tomography results by histology. The comparison between expert-based and automatic registration at three magnification levels highlights similarities in the results. By means of 2D-3D expert-based (A, D, G) and automatic (C, F, I) registration, histological section (B) was positioned in the 3D tomographic volume. E, H: magnified parts of the histological section B. Tomography images are scaled from black to white in arbitrary units of X-ray attenuation.

a related 2D-2D joint histogram. In both modalities white matter (1*, green) and *Stratum moleculare* (1, green) appear darker than *Stratum granulosum* (3, pink). The white matter exhibits very similar grey values to the *Stratum moleculare* (Schulz et al., 2012) and is presented by a single histogram peak (green) for both modalities. *Stratum granulosum* gives rise to a separate histogram peak (pink). Blood vessels exhibit intermediate grey values between *Stratum granulosum* and *Stratum moleculare* and do not have a separate peak. A grey colour overlap between *Stratum moleculare* and blood vessels caused partial segmentation of blood vessels during segmentation of *Stratum granulosum*, as highlighted in Fig. 4. Inhomogeneities in illumination during the acquisition of histology data resulted in separating the background peak into two (dark and light blue). The joint histogram shows three main data clouds associated with background (paraffin for μCT), white matter and *Stratum moleculare*, as well as *Stratum granulosum*. The standard deviation of related histogram peaks is plotted as a red line on the joint histogram.

The joint histogram shows a correlation between the grey-scaled intensities of tomography and histology. Based on the 2D joint histogram there is a quadratic correlation ($y = p1 \cdot x^2 - p2 \cdot x + p3$, where coefficients (with 95% confidence bounds) are p1 = 0.01 (−0.01, 0.03), p2 = −0.12 (−3.26, 3.02) and p3 = 14.69 (−78.52, 107.90)) between staining intensity of histology x and the local X-ray attenuation of tomography y. *Goodness of fit* (R-square = 0.9988) is reasonable. Attempts to find a linear relationship between the intensities result in a decrease in the *goodness of fit* to 0.9734. Fit coefficients (with 95% confidence bounds): p2 = −41.82(−20.81, 62.86) and p3 = 50.61 (31.4, 68.81).

Fig. 8 shows the selected tomographic slice (A) converted into an RGB colour space of histology data (B, D). The grey-scaled tomographic slice has been transformed into a colour space based on quadratic and linear interpolation, respectively, through component-wise histogram equalisation. Differences between the RGB-coloured tomography slices B and D are hardly recognisable.

To compare the quality of the images obtained with μCT and histology we considered the contrast-to-noise ratio between the anatomical structures given by Eq. (1), where I_1, I_2, σ_1 and σ_2 were extracted from histogram fitting. The results are shown in Table 2. Note that the increased *CNR* of μCT compared to Table 1 is caused by data filtering.

In general, histological data exhibit a higher contrast-to-noise ratio than tomography, as highlighted in Table 2. The highest contrast-to-noise ratio was determined to be between the background and *Stratum granulosum* for both modalities. *CNRs* between morphological structures, calculated for the histological slices acquired with the optical magnifications 1.25× and 2× provide comparable results, with a difference less than 10% except for *CNR* (2), as due to resolution decrease *Stratum granulosum* appears less homogeneous.

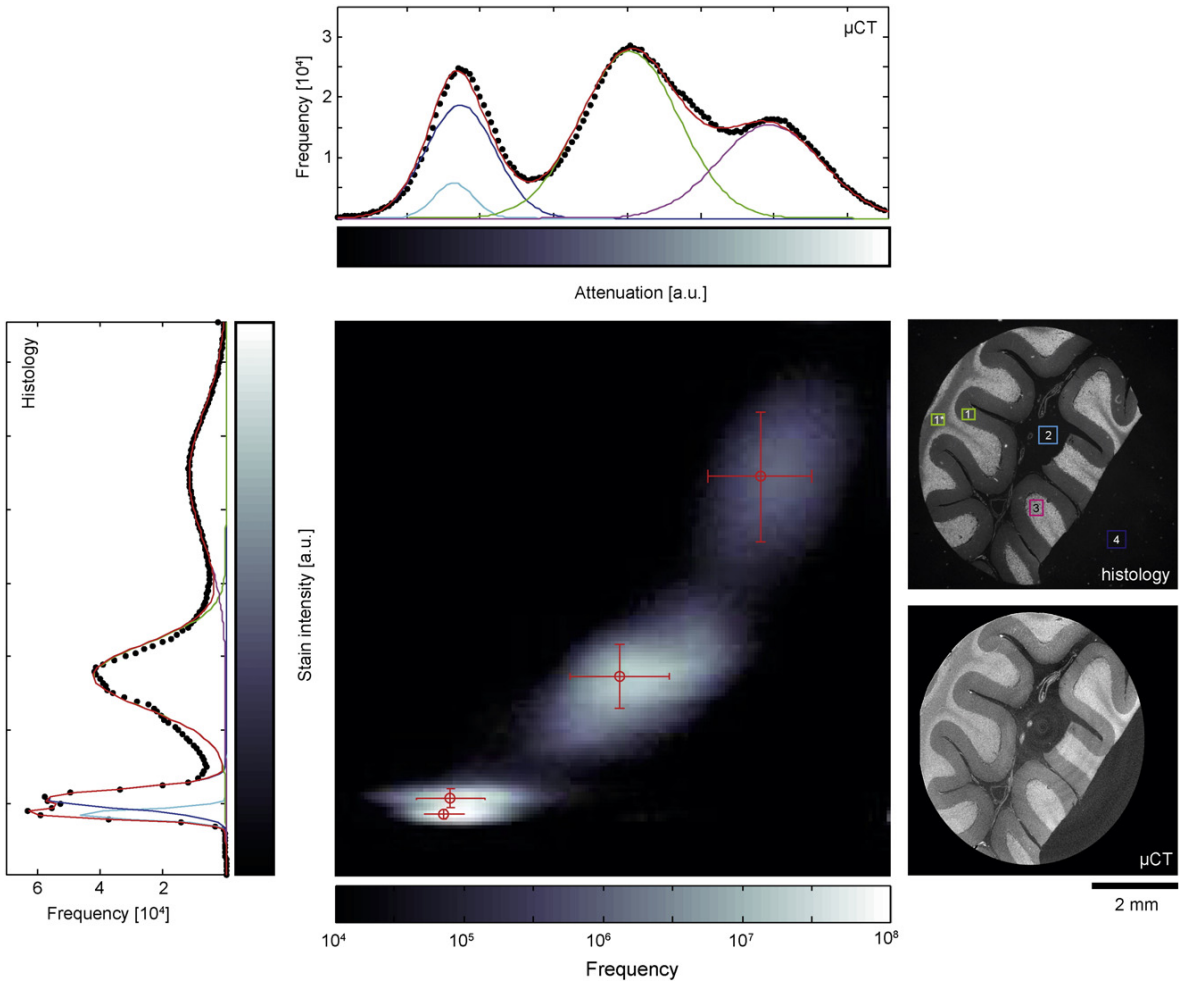

Fig. 7. Joint histogram of registered the tomographic slice and the histological section with histograms (black dots), with fitted multi-Gaussian distributions (red curves) and individual Gaussian peaks (light blue, dark blue, green and pink). Light and dark blue (2 and 4): background (paraffin for μCT), green (1) *Stratum moleculare* and (1*) white matter, pink (3): *Stratum granulosum*.

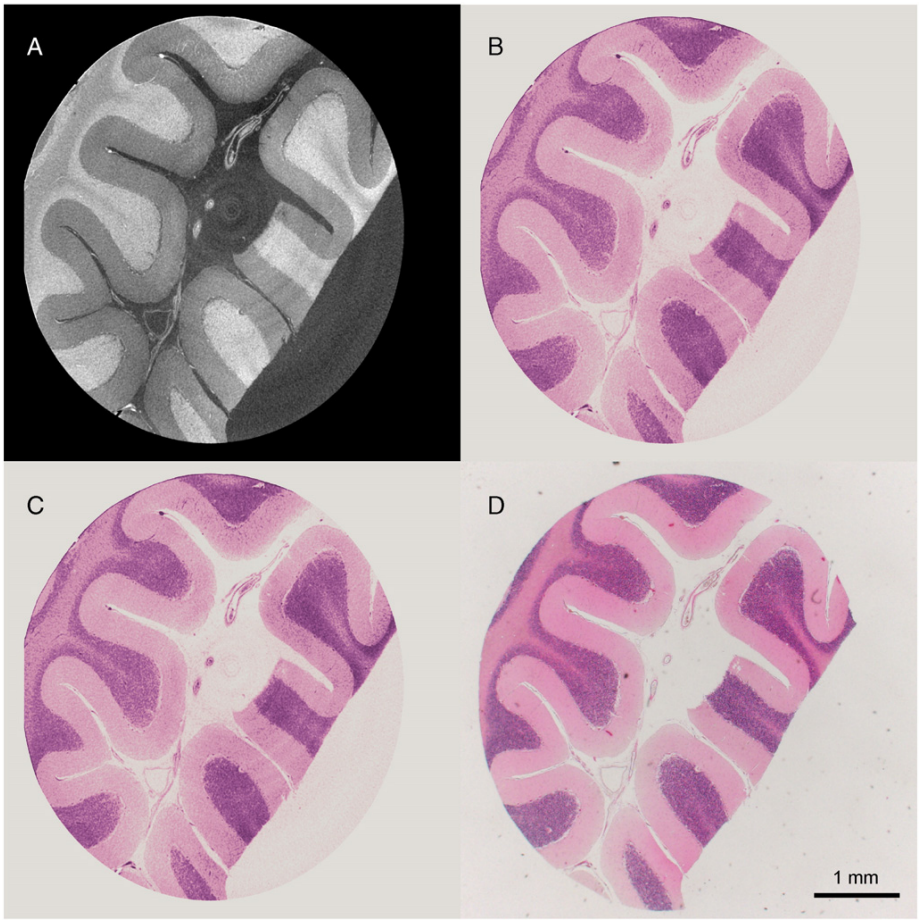

Fig. 8. Virtual histology by colourised μCT: Comparison of stain intensity and X-ray attenuation. The selected registered tomography slice (A) has been converted into an RGB colour space to resemble the H&*E*-stained histological section (D). B: tomography slice coloured as histology based on the quadratic relation, C: tomography slice coloured as histology based on the linear relation.

Discussion

The results shown in Table 1 demonstrate that scans performed with lower voltages and tungsten targets generally exhibit a better contrast-to-noise ratio for anatomical features. This result is expected, as the selected voltages are higher than optimal for the soft tissue sample (Schulz et al., 2010b). In order to increase contrast, energy reduction is required (Grodzins, 1983a, 1983b). Due to the insufficient counts for the low voltages in the nanotom® m, a further decrease in voltage is not beneficial. Therefore, the lowest possible voltage with sufficient photon counts provides the best results.

The currently available μCT systems provide isotropic micrometer resolution. It is well known, that formalin-fixed human brain tissues show limited X-ray absorption contrast. It was shown by Schulz et al. (Schulz et al., 2010b) that only marginal absorption contrast of a formalin-fixed human cerebellum using SRμCT can be achieved. Obviously, the contrast found for FFPE brain is superior (see Figs. 4 and 6). In the specific case of the cerebellum, the 3D visualisation of the Purkinje cells without staining could be achieved. Dehydration of the tissue induces a structure-dependent density increase. It is speculated that dehydration also causes an increase in attenuation differences, which leads to the observed gain in contrast. The subsequently performed paraffin embedding may accentuate the attenuation differences.

A decrease of pixel size below 3.5 μm enables sub-cellular resolution. The μCT system used in the present study can record data with pixel sizes down to 200 nm (General Electric, Measurement and Control, 2014). This nanometer range would be sufficient to visualize the neuronal dendrite structures or vascular structure including small capillaries without contrast agent in 3D. Such pixel sizes, however, restrict the sample diameters to the micrometer range. Nevertheless, the spatial resolution, which is limited by the focal spot size of around 900 nm, for acceptable acquisition times is hardly better than one micrometer. If the user agrees with micrometer resolution, volumes of centimeter sizes can be evaluated. The multi|scan function (General Electric, Measurement and Control, 2014) enables to scan one height step after the other. In this direction, the sample size is only restricted by the size of interior of the instrument and the hub of the manipulator. Based on the specifications, the system is applicable to a wide sample

Table 2
Results for the quantitative comparison of *CNR* between the tomographic slice and the histological section (see Fig. 7). *CNR* (1): contrast-to-noise ratio between the background and *Stratum moleculare*/white matter, *CNR* (2): contrast-to-noise ratio between the background and *Stratum granulosum*, *CNR* (3): contrast-to-noise ratio between *Stratum moleculare*/white matter and *Stratum granulosum*, VR: volume ratio *Stratum moleculare*/*Stratum granulosum* for 2D slices (*) and 3D data.

	CNR (*I*)	*CNR* (*II*)	*CNR* (*III*)	VR(*)	VR
Histology	3.65 ± 0.10	4.91 ± 0.05	2.75 ± 0.03	1.95 ± 0.03	
μCT	2.81 ± 0.08	4.96 ± 0.17	1.96 ± 0.05	1.93 ± 0.05	$1.97 \pm 2.03 \times 10^{-4}$

range between 0.25 mm and 250 mm sample height. Thus, we conclude that μCT allows sample visualisation with cellular resolution with minor sample size limitations.

Within approximately four hours 600 μCT-slices have been acquired. The acquisition of a comparable number of histological sections by means of serial sectioning might need between five and ten hours. Staining with haematoxylin and eosin (H&E) requires additional time, approximately up to 15 min per slide. In addition, serial sectioning is technically challenging and individual sections can be lost. The final volume reconstruction by registration of thin sections is a complex, technically demanding process (Krauth et al., 2010).

The comparison of histograms, as seen in Fig. 7, enables us to conclude that modalities are comparable and present very similar information for the same anatomical structures. The results suggest that μCT could become a significant complement to histological methods, as it offers the possibility of virtual histology (Gambichler et al., 2007) of physically soft tissues within a laboratory environment. Virtual cutting planes within the tomography volume can essentially simulate cuts at any angle, which would be of considerable benefit to histology, where cut direction can only partially be controlled, typically not altered and has limitations with respect to the number of sections. We specifically envision pre-sectioning scans to extrapolate histological data to 3D.

Histological examinations represent a powerful, high-resolution methodology. One has to understand that H&E, even though it is the most common form of staining, sits well below the capabilities that histochemistry has to offer in general. Histological sections are typically stained with diverse dyes and labelling systems. Furthermore, histochemistry typically reveals biochemical data along with morphology. A qualitative comparison of the histological section (Fig. 8 D) and RGB-scaled tomographic slices (Fig. 8 B and C) highlights similarities in the data. A combination of histology and tomography could enable virtual “multi-staining”, and each histological section can be stained with one protocol highlighting particular structures of interest, while μCT can extrapolate results over the entire specimen. Moreover, μCT is non-destructive, and so the same specimen can be reused for further investigations.

In histology, staining intensity often varies significantly due to storage temperature, tissue preservation, etc. (Richendrfer et al., 2009). In addition, microscopic data are influenced by illumination conditions and the colorimetric characteristics of the camera. Combining imaging methods enables inter- or intra-sample comparisons.

The fusion of histological and tomographic data can enhance the significant benefits of multimodal imaging (Uludağ and Roebroeck, 2014) when studying tissue microstructures. Tomography can be used to complement histology techniques in clinical applications with the potential to automate quantification tasks, for example volume measurements of the entire cerebellum or its layers (Hashimoto et al., 2001; Rosin et al., 2015) or the localisation of pathological changes in FFPE specimens that could then be optimally oriented for sectioning. Measuring the volume of the cerebellum can be performed in vivo by MRI with acceptable resolutions, but the strength of μCT is clearly its micrometer range resolution, and μCT can allow for statistically significant isotropic volume or surface measurements to be performed on the entire tissue sample of microstructures such as individual cells.

Nevertheless, the merits of true isotropic visualisation are not limited to providing better volumetric measurements. Another potential application of μCT data is the correction of local distortions in histological data due to the preparation procedures (Mega et al., 1997) by applying 2D-3D registration, similar to (Schulz et al., 2010a).

Conclusion

We have demonstrated that paraffin-embedded human tissue shows sufficient absorption contrast for the discrimination of the specimen's characteristic morphology, including individual cells. Structures with diameters on the micrometer scale are visible not only in bony tissue, but also in soft materials with laboratory μCT system. Due to the observed effect, one can conclude that paraffin embedding increases the density resolution in brain tissue. Thus, laboratory-based μCT of FFPE samples can be understood as ease of use, fast and reliable tissue visualisation methodology suitable for imaging of biological specimens with volume in cm-range.

Furthermore, we have shown that 2D-3D registration can generate accurate correspondence and has the potential to implement 3D tomographic data into histological examinations. Moreover, 3D data can be correlated to and extend 2D histological data.

Acknowledgements

The financial support of Swiss National Science Foundation (SNSF) projects 147172, 150164 and SNSF R'Equip project 133802 is highly acknowledged. The authors are thankful to members of the BMC team for their helpful discussions, and Peter Thalmann who greatly assisted the work.

References

Ashton, J., West, J., Badea, C., 2015. In vivo small animal micro-CT using nanoparticle contrast agents. Front. Pharmacol. 6. http://dx.doi.org/10.3389/fphar.2015.00256.

Bay, H., Ess, A., Tuytelaars, T., Van Gool, L., 2008. Speeded-Up Robust Features (SURF). Comput. Vis. Image Underst. 110, 346–359. http://dx.doi.org/10.1016/j.cviu.2007.09.014.

Beckmann, F., Herzen, J., Haibel, A., Müller, B., Schreyer, A., 2008. High density resolution in synchrotron-radiation-based attenuation-contrast microtomography. Proc. SPIE 7078, 70781D. http://dx.doi.org/10.1117/12.794617.

Blouin, S., Moreau, M., Baslé, M., Chappard, D., 2006. Relations between radiograph texture analysis and microcomputed tomography in two rat models of bone metastases. Cells Tissues Organs 182, 182–192. http://dx.doi.org/10.1159/000093967.

Chappard, D., Blouin, S., Libouban, H., Baslè, M.F., Audran, M., 2005. Microcomputed tomography for the study of hard tissues and bone biomaterials. Microsc. Anal. 19, 19–21.

Chicherova, N., Fundana, K., Müller, B., Cattin, P., 2014. Histology to μCT data matching using landmarks and a density biased RANSAC. Lect. Notes Comput. Sci. (Including Subseries Lect. Notes Artif. Int. and Lect. N. Bioinformati.) 8673 LNCS, 243–250. http://dx.doi.org/10.1007/978-3-319-10404-1_31.

Chung, K., Wallace, J., Kim, S.Y., Kalyanasundaram, S., Andalman, A., Davidson, T., Mirzabekov, J., Zalocusky, K., Mattis, J., Denisin, A., Pak, S., Bernstein, H., Ramakrishnan, C., Grosenick, L., Gradinaru, V., Deisseroth, K., 2013. Structural and molecular interrogation of intact biological systems. Nature 497, 332–337. http://dx.doi.org/10.1038/nature12107.

Costantini, I., Ghobril, J.P., Di Giovanna, A., Mascaro, A., Silvestri, L., Müllenbroich, M., Onofri, L., Conti, V., Vanzi, F., Sacconi, L., Guerrini, R., Markram, H., Iannello, G., Pavone, F., 2015. A versatile clearing agent for multi-modal brain imaging. Sci. Rep. 5, 1–5. http://dx.doi.org/10.1038/srep09808.

de Crespigny, A., Bou-Reslan, H., Nishimura, M.C., Phillips, H., Carano, R.A.D., D'Arceuil, H.E., 2008. 3D micro-CT imaging of the postmortem brain. J. Neurosci. Methods 171, 207–213. http://dx.doi.org/10.1016/j.jneumeth.2008.03.006.

Dodt, H.U., Leischner, U., Schierloh, A., Jährling, N., Mauch, C., Deininger, K., Deussing, J., Eder, M., Zieglgänsberger, W., Becker, K., 2007. Ultramicroscopy: three-dimensional visualization of neuronal networks in the whole mouse brain. Nat. Methods 4, 331–336. http://dx.doi.org/10.1038/nmeth1036.

Egbert, A., Brunke, O., 2011. High-resolution X-ray computed tomography for materials research. Adv. Mater. Res. 222, 48–51. http://dx.doi.org/10.4028/www.scientific.net/AMR.222.48.

Feldkamp, I., Davis, L., Kress, J., 1984. Practical cone-beam algorithm. J. Opt. Soc. Am. A Opt. Image Sci. Vis. 1, 612–619.

Fischler, M., Bolles, R., 1981. Random sample consensus: a paradigm for model fitting with applications to image analysis and automated cartography. Commun. ACM 24, 381–395. http://dx.doi.org/10.1145/358669.358692.

Fuchs, T., Buhmann, J., 2011. Computational pathology: challenges and promises for tissue analysis. Comput. Med. Imaging Graph. 35, 515–530. http://dx.doi.org/10.1016/j.compmedimag.2011.02.006.

Gambichler, T., Moussa, G., Regeniter, P., Kasseck, C., Hofmann, M., Bechara, F., Sand, M., Altmeyer, P., Hoffmann, K., 2007. Validation of optical coherence tomography in vivo using cryostat histology. Phys. Med. Biol. 52, N75–N85. http://dx.doi.org/10.1088/0031-9155/52/5/N01.

General Electric, Measurement and Control, 2014. phoenix|xray nanotom® m 180 kV/20 W X-ray nanoCT system for high-resolution analysis and 3D metrology. (URL:) https://www.gemeasurement.com/inspection-ndt/radiography-and-computed-tomography/phoenix-nanotom-m.

Germann, M., Morel, A., Beckmann, F., Andronache, A., Jeanmonod, D., Müller, B., 2008. Strain fields in histological slices of brain tissue determined by synchrotron radiation-based micro computed tomography. J. Neurosci. Methods 170, 149–155. http://dx.doi.org/10.1016/j.jneumeth.2008.01.011.

Grodzins, L., 1983a. Optimum energies for x-ray transmission tomography of small samples. Applications of synchrotron radiation to computerized tomography I. Nucl.

Instrum. Methods Phys. Res. 206, 541–545. http://dx.doi.org/10.1016/0167-5087(83)90393-9.
Grodzins, L., 1983b. Critical absorption tomography of small samples.Proposed applications of synchrotron radiation to computerized tomography II. Nucl. Instrum. Methods Phys. Res. 206, 547–552. http://dx.doi.org/10.1016/0167-5087(83)90393-9.
Guk, B., Yae, J., Tae, J., Hwa, S., Yong, S., Sang, J., 2008. X-ray imaging of various biological samples using a phase-contrast hard X-ray microscope. Microsc. Res. Tech. 71, 639–643. http://dx.doi.org/10.1002/jemt.20601.
Hashimoto, H., Shintani, N., Tanaka, K., Mori, W., Hirose, M., Matsuda, T., Sakaue, M., Miyazaki, J.I., Niwa, H., Tashiro, F., Yamamoto, K., Koga, K., Tomimoto, S., Kunugi, A., Suetake, S., Baba, A., 2001. Altered psychomotor behaviors in mice lacking pituitary adenylate cyclase-activating polypeptide (PACAP). Proc. Natl. Acad. Sci. U. S. A. 98, 13355–13360. http://dx.doi.org/10.1073/pnas.231094498.
Huang, S., Kou, B., Chi, Y., Xi, Y., Cao, Y., Cui, W., Hu, X., Shao, Z., Guo, H., Fu, Y., Xiao, T., Sun, J., Zhao, J., Wang, Y., Wu, J., 2015. In-line phase-contrast and grating-based phase-contrast synchrotron imaging study of brain micrometastasis of breast cancer. Sci. Rep. 5. http://dx.doi.org/10.1038/srep09418.
Irshad, H., Veillard, A., Roux, L., Racoceanu, D., 2014. Methods for nuclei detection, segmentation, and classification in digital histopathology: a review-current status and future potential. IEEE Rev. Biomed. Eng. 7, 97–114. http://dx.doi.org/10.1109/RBME.2013.2295804.
Kandel, E.R., Schwartz, J.H., Jessell, T.M., Siegelbaum, S.A., Hudspeth, A.J., 2012. Principles of Neural Science (Kandel). fifth ed. McGraw-Hill Education/Medical.
Krauth, A., Blanc, R., Poveda, A., Jeanmonod, D., Morel, A., Székely, G., 2010. A mean three-dimensional atlas of the human thalamus: generation from multiple histological data. NeuroImage 49, 2053–2062. http://dx.doi.org/10.1016/j.neuroimage.2009.10.042.
Kroon, D.J., Slump, C., 2009. MRI modalitiy transformation in demon registration. Proc. ISBI 1, 963–966. http://dx.doi.org/10.1109/ISBI.2009.5193214.
Lang, S., Zanette, I., Dominietto, M., Langer, M., Rack, A., Schulz, G., Le Duc, G., David, C., Mohr, J., Pfeiffer, F., Müller, B., Weitkamp, T., 2014. Experimental comparison of grating- and propagation-based hard X-ray phase tomography of soft tissue. J. Appl. Phys. 116, 116. http://dx.doi.org/10.1063/1.4897225.
Langer, M., Pacureanu, A., Suhonen, H., Grimal, Q., Cloetens, P., Peyrin, F., 2012. Phase nanotomography resolves the 3D human bone ultrastructure. PLoS One 7. http://dx.doi.org/10.1371/journal.pone.0035691.
Lareida, A., Beckmann, F., Schrott-Fischer, A., Glueckert, R., Freysinger, W., Müller, B., 2009. X-ray tomography of the human inner ear: synchrotron radiation-based study of nerve fibre bundles, membranes and ganglion cells. J. Microsc. 234, 95–102. http://dx.doi.org/10.1111/j.1365-2818.2009.03143.x.
Manjon-Herrera, J.V., 2006. EM image segmentation. (URL:) http://www.mathworks.com/matlabcentral/fileexchange/10956-em-image-segmentation.
Markelj, P., Tomaževič, D., Likar, B., Pernuš, F., 2012. A review of 3D/2D registration methods for image-guided interventions. Med. Image Anal. 16, 642–661. http://dx.doi.org/10.1016/j.media.2010.03.005.
Mega, M.S., Chen, S.S., Thompson, P.M., Woods, R.P., Karaca, T.J., Tiwari, A., Vinters, H.V., Small, G.W., Toga, A.W., 1997. Mapping histology to metabolism: coregistration of stained whole-brain sections to premortem PET in Alzheimer's disease. NeuroImage 5, 147–153. http://dx.doi.org/10.1006/nimg.1996.0255.
Metscher, B.D., 2009. MicroCT for comparative morphology: simple staining methods allow high-contrast 3D imaging of diverse non-mineralized animal tissues. BMC Physiol. 9, 1–14. http://dx.doi.org/10.1186/1472-6793-9-11.
Mokso, R., Cloetens, P., Maire, E., Ludwig, W., Buffire, J.Y., 2007. Nanoscale zoom tomography with hard x rays using Kirkpatrick-Baez optics. Appl. Phys. Lett. 90. http://dx.doi.org/10.1063/1.2719653.
Müller, B., Beckmann, F., Huser, M., Maspero, F., Szekely, G., Ruffieux, K., Thurner, P., Wintermantel, E., 2002. Non-destructive three-dimensional evaluation of a polymer sponge by micro-tomography using synchrotron radiationy. Biomol. Eng. 19, 73–78. http://dx.doi.org/10.1016/S1389-0344(02)00014-X.
Müller, B., Deyhle, H., Lang, S., Schulz, G., Bormann, T., Fierz, F., Hieber, S., 2012. Three-dimensional registration of tomography data for quantification in biomaterials science. Int. J. Mater. Res. 103, 242–249. http://dx.doi.org/10.3139/146.110663.
Müller, B., Riedel, M., Thurner, P.J., 2006. Three-dimensional characterization of cell clusters using synchrotron-radiation-based micro-computed tomography. Microsc. Microanal. 12, 97–105. http://dx.doi.org/10.1017/S1431927606060168.
Murray, E., Cho, J., Goodwin, D., Ku, T., Swaney, J., Kim, S.Y., Choi, H., Park, Y.G., Park, J.Y., Hubbert, A., McCue, M., Vassallo, S., Bakh, N., Frosch, M., Wedeen, V., Seung, H., Chung, K., 2015. Simple, scalable proteomic imaging for high-dimensional profiling of intact systems. Cell 163, 1500–1514. http://dx.doi.org/10.1016/j.cell.2015.11.025.
Ribi, W., Senden, T.J., Sakellariou, A., Limaye, A., Zhang, S., 2008. Imaging honey bee brain anatomy with micro-X-ray-computed tomography. J. Neurosci. Methods 171, 93–97. http://dx.doi.org/10.1016/j.jneumeth.2008.02.010.
Richardson, D., Lichtman, J., 2015. Clarifying tissue clearing. Cell 162, 246–257. http://dx.doi.org/10.1016/j.cell.2015.06.067.
Richendrfer, H., Wetzel, J., Swann, J., 2009. Temperature, peroxide concentration, and immunohistochemical staining method affects staining intensity, distribution, and background. Appl. Immunohistochem. Mol. Morphol. 17, 543–546. http://dx.doi.org/10.1097/PAI.0b013e3181a91595.
Rosin, J., McAllister, B., Dyck, R., Percival, C., Kurrasch, D., Cobb, J., 2015. Mice lacking the transcription factor SHOX2 display impaired cerebellar development and deficits in motor coordination. Dev. Biol. 399, 54–67. http://dx.doi.org/10.1016/j.ydbio.2014.12.013.
Schulz, G., Morel, A., Imholz, M., Deyhle, H., Weitkamp, T., Zanette, I., Pfeiffer, F., David, C., Müller-Gerbl, M., Müller, B., 2010a. Evaluating the microstructure of human brain tissues using synchrotron radiation-based micro computed tomography. Proc. SPIE 7804, 78040F. http://dx.doi.org/10.1117/12.859273.
Schulz, G., Waschkies, C., Pfeiffer, F., Zanette, I., Weitkamp, T., David, C., Müller, B., 2012. Multimodal imaging of human cerebellum - merging X-ray phase microtomography, magnetic resonance microscopy and histology. Sci. Rep. 2, 826. http://dx.doi.org/10.1038/srep00826.
Schulz, G., Weitkamp, T., Zanette, I., Pfeiffer, F., Beckmann, F., David, C., Rutishauser, S., Reznikova, E., Müller, B., 2010b. High-resolution tomographic imaging of a human cerebellum: comparison of absorption and grating-based phase contrast. J. R. Soc. Interface 7, 1665–1676. http://dx.doi.org/10.1098/rsif.2010.0281.
Silvestri, L., Bria, A., Sacconi, L., Iannello, G., Pavone, F., 2012. Confocal light sheet microscopy: micron-scale neuroanatomy of the entire mouse brain. Opt. Express 20, 20582–20598. http://dx.doi.org/10.1364/OE.20.020582.
So, P., 2002. Encyclopedia of Life Sciences, Two-photon Fluorescence Light Microscopy. Macmillan Publishers Ltd, Nature Publishing Group.
Sombke, A., Lipke, E., Michalik, P., Uhl, G., Harzsch, S., 2015. Potential and limitations of X-ray micro-computed tomography in arthropod neuroanatomy: a methodological and comparative survey. J. Comp. Neurol. 523, 1281–1295. http://dx.doi.org/10.1002/cne.23741.
Stalder, A., Ilgenstein, B., Chicherova, N., Deyhle, H., Beckmann, F., Müller, B., Hieber, S., 2014. Combined use of micro computed tomography and histology to evaluate the regenerative capacity of bone grafting materials. Int. J. Mat. Res. 105, 679–691. http://dx.doi.org/10.3139/146.111050.
Thimm, B., Hofmann, S., Schneider, P., Carretta, R., Müller, R., 2012. Imaging of cellular spread on a three-dimensional scaffold by means of a novel cell-labeling technique for high-resolution computed tomography. Tissue Eng. Part C Methods 18, 167–175. http://dx.doi.org/10.1089/ten.tec.2011.0262.
Uludağ, K., Roebroeck, A., 2014. General overview on the merits of multimodal neuroimaging data fusion. NeuroImage 102, 3–10. http://dx.doi.org/10.1016/j.neuroimage.2014.05.018.
Vladimirov, N., Mu, Y., Kawashima, T., Bennett, D., Yang, C.T., Looger, L., Keller, P., Freeman, J., Ahrens, M., 2014. Light-sheet functional imaging in fictively behaving zebrafish. Nat. Methods 11, 883–884. http://dx.doi.org/10.1038/nmeth.3040.
Wang, H., Zhu, J., Akkin, T., 2014. Serial optical coherence scanner for large-scale brain imaging at microscopic resolution. NeuroImage 84, 1007–1017. http://dx.doi.org/10.1016/j.neuroimage.2013.09.063.
Wenz, J., Schleede, S., Khrennikov, K., Bech, M., Thibault, P., Heigoldt, M., Pfeiffer, F., Karsch, S., 2015. Quantitative X-ray phase-contrast microtomography from a compact laser-driven betatron source. Nat. Commun. 6. http://dx.doi.org/10.1038/ncomms8568.
Wolf, S., Supatto, W., Debrégeas, G., Mahou, P., Kruglik, S., Sintes, J.M., Beaurepaire, E., Candelier, R., 2015. Whole-brain functional imaging with two-photon light-sheet microscopy. Nat. Methods 12, 379–380. http://dx.doi.org/10.1038/nmeth.3371.
Zehbe, R., Haibel, A., Riesemeier, H., Gross, U., Kirkpatrick, C., Schubert, H., Brochhausen, C., 2010. Going beyond histology.Synchrotron micro-computed tomography as a methodology for biological tissue characterization: from tissue morphology to individual cells. J. R. Soc. Interface 7, 49–59. http://dx.doi.org/10.1098/rsif.2008.0539.
Zehbe, R., Schmitt, V.H., Kirkpatrick, C.J., Brochhausen, C., 2015. High resolution X-ray tomography - three-dimensional characterisation of cell-scaffold constructs for cartilage tissue engineering. Mater. Sci. Technol. (UK) 31, 167–173. http://dx.doi.org/10.1179/1743284714Y.0000000667.

X-ray micro-tomography for investigations of brain tissues on cellular level

A. Khimchenko, G. Schulz, H. Deyhle, P. Thalmann, I. Zanette, M-C. Zdora, C. Bikis, A. Hipp, S. E. Hieber, G. Schweighauser, J. Hench, B. Müller,

Proceedings of SPIE 9967, 996703 (2016)
(doi:10.1117/12.2237554)

X-ray micro-tomography for investigations of brain tissues on cellular level

Anna Khimchenko[a*], Georg Schulz[a], Hans Deyhle[a], Peter Thalmann[a], Irene Zanette[b], Marie-Christine Zdora[b,c], Christos Bikis[a], Alexander Hipp[d], Simone E. Hieber[a], Gabriel Schweighauser[e], Jürgen Hench[e], and Bert Müller[a]

[a] Biomaterials Science Center, Department of Biomedical Engineering, University of Basel, Gewerbestrasse 14, 4123 Allschwil, Switzerland;
[b] Diamond Light Source Ltd, Diamond House, OX11 0DE Didcot, Oxfordshire, UK;
[c] Department of Physics and Astronomy, University College London, Gower Street, WC1E 6BT London, UK;
[d] Helmholtz-Zentrum Geesthacht, Max-Planck-Strasse 1, 21502 Geesthacht, Germany;
[e] Institute of Pathology, Department of Neuropathology, Basel University Hospital, Schönbeinstrasse 40, 4056 Basel, Switzerland

ABSTRACT

X-ray imaging in absorption contrast mode is well established for hard tissue visualization. However, performance for lower density materials is limited due to a reduced contrast. Our aim is three-dimensional (3D) characterization of micro-morphology of human brain tissues down to (sub-)cellular resolution within a laboratory environment. Using the laboratory-based microtomography (µCT) system nanotom® m (GE Sensing & Inspection Technologies GmbH, Wunstorf, Germany) and synchrotron radiation at the Diamond-Manchester Imaging Branchline I13-2 (Diamond Light Source, Didcot, UK), we have acquired 3D data with a resolution down to 0.45 µm for visualization of a human cerebellum specimen down to cellular level. We have shown that all selected modalities, namely laboratory-based absorption contrast micro-tomography (LBµCT), synchrotron radiation based in-line single distance phase contrast tomography (SDPR) and synchrotron radiation based single-grating interferometry (GI), can reach cellular resolution for tissue samples with a size in the mm-range. The results are discussed qualitatively in comparison to optical microscopy of haematoxylin and eosin (H&E) stained sections. As phase contrast yields to a better data quality for soft tissues and in order to overcome restrictions of limited beamline access for phase contrast measurements, we have equipped the µCT system nanotom® m with a double-grating phase contrast set-up. Preliminary experimental results of a knee sample consisting of a bony part and a cartilage demonstrate that phase contrast data exhibits better quality compared to absorption contrast. Currently, the set-up is under adjustment. It is expected that cellular resolution would also be achieved. The questions arise (1) what would be the quality gain of laboratory-based phase contrast in comparison to laboratory-based absorption contrast tomography and (2) could laboratory-based phase contrast data provide comparable results to synchrotron radiation based phase contrast data.

Keywords: X-ray micro-tomography, phase contrast, absorption contrast, grating interferometry, synchrotron radiation, brain tissue, cerebellum.

1. INTRODUCTION

Human brain belongs to the most impressive[1] organs within the body and its disorders are a severe health problem of a modern ageing society.[2] Being diverse in macroscopic symptoms, neurodegenerative disorders have much in common on (sub-)cellular level: loss of cells, demyelination or damage of cell axons.[3] There are many open questions in the field. For example, exact causes and key clinical features of a degenerative process, such as the role of metal ions,[4–6] are not clear; knowledge about neuroanatomical connections is limited as well.[7] Thus, high-resolution three-dimensional (3D) visualization of brain tissue can be highly beneficial.[8]

* anna.khimchenko@unibas.ch; phone: +41 61 207 54 41; fax: +41 61 207 54 99; bmc.unibas.ch

Developments in X-Ray Tomography X, edited by Stuart R. Stock, Bert Müller, Ge Wang, Proc. of SPIE Vol. 9967, 996703 · © 2016 SPIE · CCC code: 0277-786X/16/$18 · doi: 10.1117/12.2237554

The structure of brain and nervous system is complex,[9,10] having a 3D multi-scale hierarchical organization. Thus, characterization of volumes is desirable over thin sections. Nevertheless, within a laboratory environment remains a gap in large-scale 3D imaging techniques that provides high spatial resolution and density contrast for soft tissues. Serial sectioning or block-face methods[11,12] require a complex volume reconstruction,[13] do not provide isotropic resolution, are destructive, time-consuming, and often related to a significant tissue loss, stress, and strain. Sectioning-free methods combined with tissue-transformation[14,15] are expensive, time-consuming and cause local changes within inhomogeneous tissues.

The conventional approach for visualization of soft tissues with a cellular resolution within a laboratory environment remains optical microscopy,[16,17] see Figure 1. Apart from possible slicing or staining artifacts (Fig. 1 steps 5 - 8), this methodology is highly time-consuming, making it almost impossible to cover the complete 3D micro-architecture.[18–20] In addition, this methodology is destructive (Fig. 1 step 5).[17]

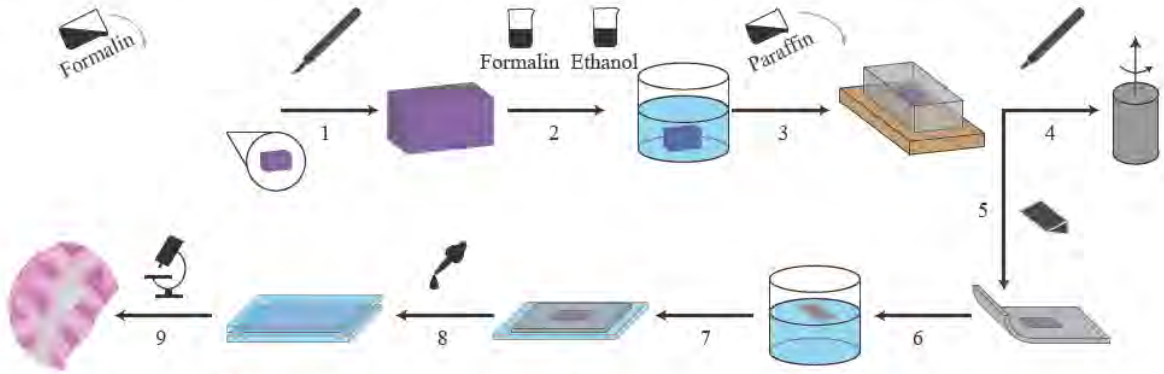

Figure 1. Imaging work flow: schematic representation of the specimen preparation for optical microscopy examination (steps 1 - 3 and 5 - 9) and tomography (steps 1 - 4). 1: specimen dissection; 2: fixation and dehydration; 3: paraffin embedding; 4: punching of a cylinder; 5: sectioning by microtome; 6, 7: mounting of a thin section on a glass slide; 8: staining; 9: optical microscopy examination.

At the same time, X-ray imaging modalities can offer cellular resolution for large tissue volumes in a non-destructive manner.[21–25] In this communication, we discuss methods for soft tissue visualization suitable for extracting cellular information within a laboratory environment. Comparing laboratory-based absorption contrast data of formalin-fixed paraffin-embedded (FFPE) human cerebellum specimen to selected synchrotron radiation based phase contrast modalities, one can see that data quality is comparable. It is expected that extending laboratory-based μCT system towards phase contrast will yield further data quality increase. The open questions remain (1) what is the quality gain in comparison to laboratory-based absorption contrast tomography and (2) could laboratory-based phase contrast data provide a comparable result to the synchrotron radiation based phase contrast data.

2. MATERIALS AND METHODS

2.1 Specimen preparation

The human cerebellum block from a 73-year-old male body was visualized *post mortem*. Informed consent for scientific use was obtained and all procedures were conducted in accordance with the Declaration of Helsinki and approved by the Ethikkommission Nordwestschweiz. The specimen preparation and paraffin embedding were performed based on the standard histological protocols (Fig. 1 steps 1 - 3), for more details see,[21,26] After paraffin embedding the tomography specimen with 4.0 mm height and 2.6 mm diameter was extracted with a metal punch (Fig. 1 step 4).

The femoratibial articular surface of the lateral femur condyle of the left knee joint was extracted from a donated body of a 87 years-old female, for more details see.[27] All steps were conducted in accordance with the Declaration of Helsinki and according to the ethical guidelines of the Canton Basel.

2.2 Laboratory-based absorption contrast micro-tomography

Laboratory-based absorption contrast micro-tomography ($LB_{\mu}CT$) was carried out on nanotom® m (GE Sensing & Inspection Technologies GmbH, Wunstorf, Germany) equipped with a 180 kV / 15 W nanofocus® tube with tungsten target.[28,29] The experimental parameters are summarized in Table 1. To increase the flux, the detector was moved close to source position, corresponding to the focus-detector distance FDD 255 mm, and sample close to source position, corresponding to the focus-object distance FOD 4.94 mm. Data acquisition and reconstruction were performed with datos|x 2.0 software (phoenix|x-ray, GE Sensing & Inspection Technologies GmbH, Wunstorf, Germany). The reconstructed slices were median filtered using VGStudio MAX 2.1 (Volume Graphics, Heidelberg, Germany) for a noise reduction (median filter size 3 × 3).

Table 1. Parameters of tomography methods. $LB_{\mu}CT$: laboratory-based absorption contrast micro-tomography; LBGI: laboratory-based grating interferometry; GI_8: synchrotron radiation based single grating with a period 8 µm phase contrast interferometry; GI_{10}: synchrotron radiation based single grating with a period 10 µm phase contrast interferometry; $SDPR_{1.1}$: synchrotron radiation based in-line single distance phase contrast tomography with an effective pixel size 1.1 µm; $SDPR_{0.45}$: synchrotron radiation based in-line single distance phase contrast tomography with an effective pixel size 0.45 µm; l: effective pixel size; W: beam parameters; U: tube acceleration voltage; I: tube current; E: photon energy; №: number of projections; t_{exp}: exposure time; $t_{exp}{}^{*}$: exposure time for a single phase step; d_p: sample detector distance; d_i: inter-grating distance; α: scanning angle range.

	l [µm]	W	№	t_{exp} [s]	d_p [cm]	d_i [cm]	α [deg.]
$LB_{\mu}CT$	2.20	$U = 60$ kV, $I = 310$ kV	1440	2.00	22.00		360.0
LBGI	23.22	$U = 42$ kV, $I = 310$ kV	400	9.00*		29.60	240.6
GI_8	1.10	$E = 19$ keV	1200	3.00*		58.30	180.0
GI_{10}	2.30	$E = 19$ keV	1200	3.00*		72.00	180.0
$SDPR_{1.1}$	1.10	$E = 19$ keV	2400	1.58	8.50		360.0
$SDPR_{0.45}$	0.45	$E = 19$ keV	2400	8.00	5.00		360.0

2.3 X-Ray micro-tomography in phase contrast mode

Figure 2 shows experimental arrangements for phase contrast tomography. The special optical elements, such as gratings, are required only for the grating-based methods (Fig.2 A - F).

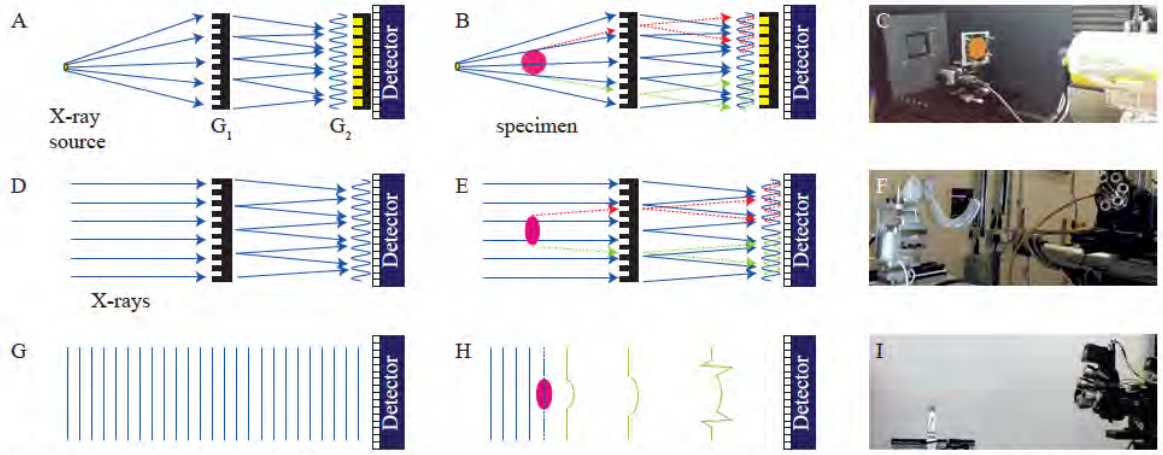

Figure 2. Schematic set-ups for X-ray micro-tomography in phase contrast mode with photographs. A, B, C: laboratory-based double-grating interferometry; D, E, F: synchrotron radiation based single-grating interferometry; G, H, I: synchrotron radiation based in-line single distance tomography. G_1: phase grating; G_2: analyser grating.

2.3.1 Laboratory-based double-grating interferometry

In order to extend capabilities of the nanotom® m toward phase contrast, it was equipped with a double-grating interferometric set-up, for more details see.[30] Laboratory-based double-grating (LBGI) measurement was performed with parameters summarized in Table 1. The source operation mode was set to *"mode 1"*, corresponding to an estimated source size of 2 µm, as specified by the supplier. Due to a sufficiently small source size the source grating (G_0) was not required. Measurements in single-grating configuration were not possible and the analyser grating (G_2) was required for the set-up as the detector is not able to resolve the interference pattern.

Figure 2 A - C shows experimental set-up for a cone-beam laboratory-based double-grating interferometry. The distance between the gratings corresponds to the 1st Talbot order. The gratings were fabricated for a design energy of 30 keV (microworks GmbH, Karlsruhe, Germany). A phase-stepping technique was used.[31] Grating G_1 was scanned over 2 periods of interference pattern in 11 phase steps. The phase recovery and tomographic reconstruction of the data were carried out in Matlab R2014a (MathWorks, Natick, USA).

2.3.2 Synchrotron radiation based single-grating interferometry

Figure 2 D - E schematically shows the set-up for synchrotron radiation based single-grating interferometry (GI) and Figure 2 F photograph of the set-up. GI of a human cerebellum specimen was performed at Diamond-Manchester Imaging Branchline I13-2 (Diamond Light Source, Didcot, UK).[32] A monochromatic X-ray beam was extracted from a silicon <111> double crystal monochromator. After being transmitted through the sample, the X-ray beam was collected by a scintillator-based X-ray detector pco.4000 (PCO AG, Kelheim, Germany) with 4× and 2× optical magnifications, with 2 single-grating set-ups: GI_8 and GI_{10}, for more details see Table 1. For both set-ups the distance between the gratings corresponds to the 1st Talbot order. The absence of a water tank in the set-up caused phase wrapping between the sample and air. Thus a "no-tank correction" was performed before phase retrieval.[33] Data processing and reconstruction were performed in a similar to LBGI manner.

2.3.3 Synchrotron radiation based in-line single distance tomography

Synchrotron radiation based in-line single distance phase contrast imaging of a human cerebellum specimen was performed at Diamond-Manchester Imaging Branchline I13-2 using a pco.4000 detector. The effective pixel sizes were 0.45 µm ($SDPR_{0.45}$) and 1.1 µm ($SDPR_{1.1}$) depending on the optical magnification of the scintillator-based detector. Since the specimen diameter was bigger for the effective pixel size of 0.45 µm than effective field of view (FOV), measurement was performed in a local tomography configuration. Flat-field and dark-current corrections, zero-padding, and phase recovery of tomography data were performed using the software tool ANKAphase[34] with an input parameter $\delta/\beta = 2406$[21] for 1.1 µm effective pixel size and $\delta/\beta = 414$ for 0.45 µm effective pixel size. The second δ/β value was decreased in order to reduce gradient artefacts in the data based on qualitative assessment. The tomographic reconstruction was done in Matlab R2014b (Simulink, The MathWorks, Inc., USA).

2.3.4 Data registration

For the comparison of tomography data acquired with selected modalities, datasets were registered using automatic 3D/3D registration tool[19,35] with rigid transformation constraints. The SDPR with effective pixel size 1.1 µm was set as reference dataset.

3. RESULTS AND DISCUSSION

3.1 Phase contrast versus absorption contrast

Figure 3 presents selected registered tomographic slices measured by LBµCT (A, D), GI_{10} (B, E) and $SDPR_{1.1}$ (C, F) with line profiles. The figure shows for each imaging modality one selected slice of a human cerebellum specimen with a magnification. Magnifications in Figure 3 E - F are cropped around the region occupied by structures of interest. Visual inspection of the registered slices reveals that *Stratum granulosum*, *Stratum moleculare*, individual cells, and blood vessels within the white matter can be recognised for all modalities in a comparable manner. Intensity differentiation between *Stratum granulosum* and *Stratum moleculare*, which both belong to grey matter, can enable intensity-based segmentation of individual cerebellar layers. LBµCT data exhibits a higher level of noise, thus additional filtering is essential for a better feature extraction.

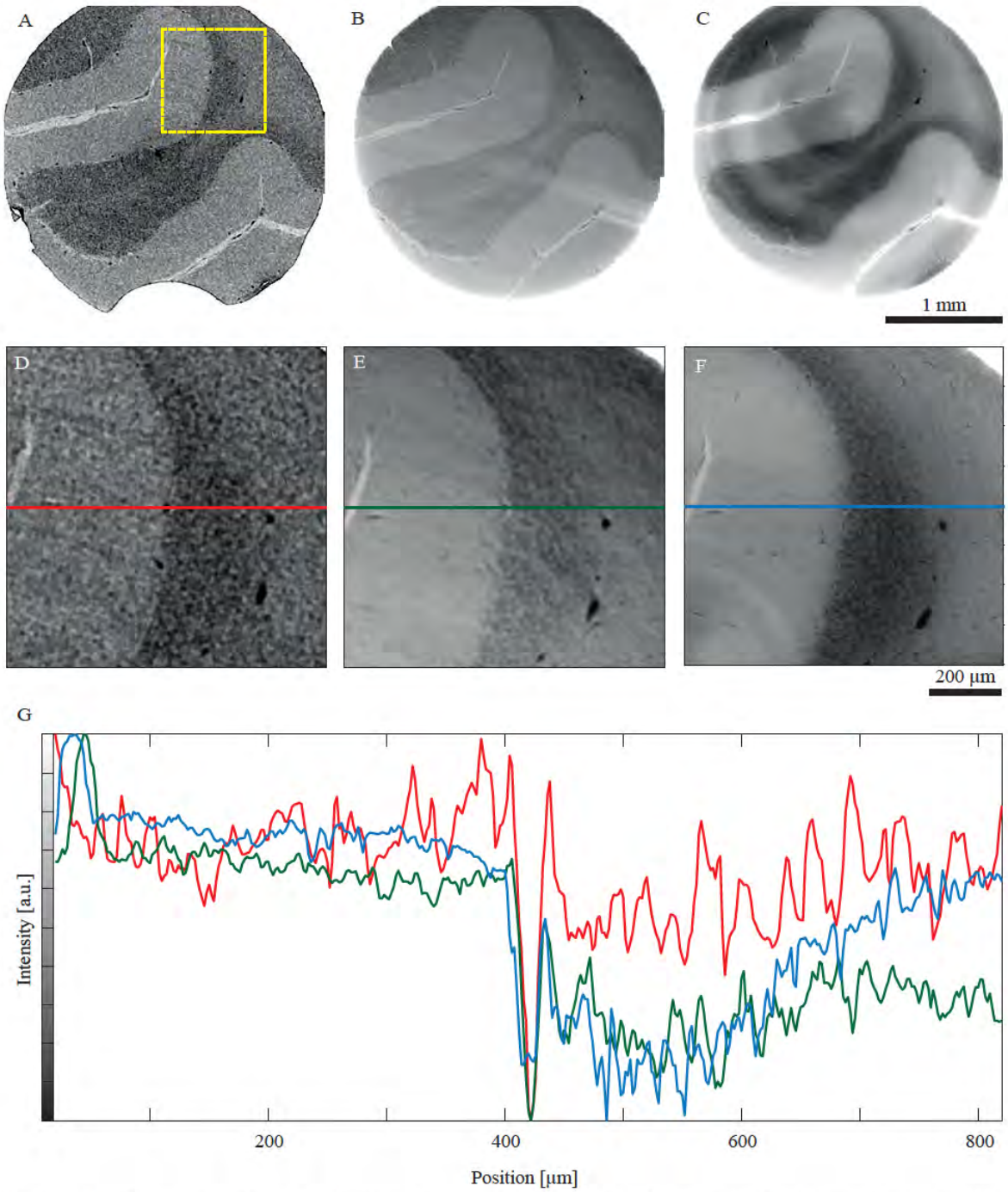

Figure 3. Selected registered tomographic slices measured by µCT in absorption contrast (A, D), synchrotron radiation based phase contrast interferometry with a grating period of 10 µm (B, E) and synchrotron radiation based in-line single distance phase contrast tomography with an effective pixel size of 1.1 µm. Line plot through the magnified part of slices (G) illustrates that modalities are comparable in terms of normalized intensity.

Currently available laboratory-based μCT systems can provide isotropic resolution[1] down to 300 nm. The limiting parameter for the successful visualization of soft tissue in the absorption mode is contrast.[1] Thus, for visualization of soft tissues, phase contrast is preferred due to a higher sensitivity.[17,36] It was recently demonstrated that FFPE brain tissues provide a contrast comparable to a conventional histology.[26] In this communication, we state that the data contrast is almost alike to a synchrotron radiation based phase contrast data.

3.2 Cellular visualization

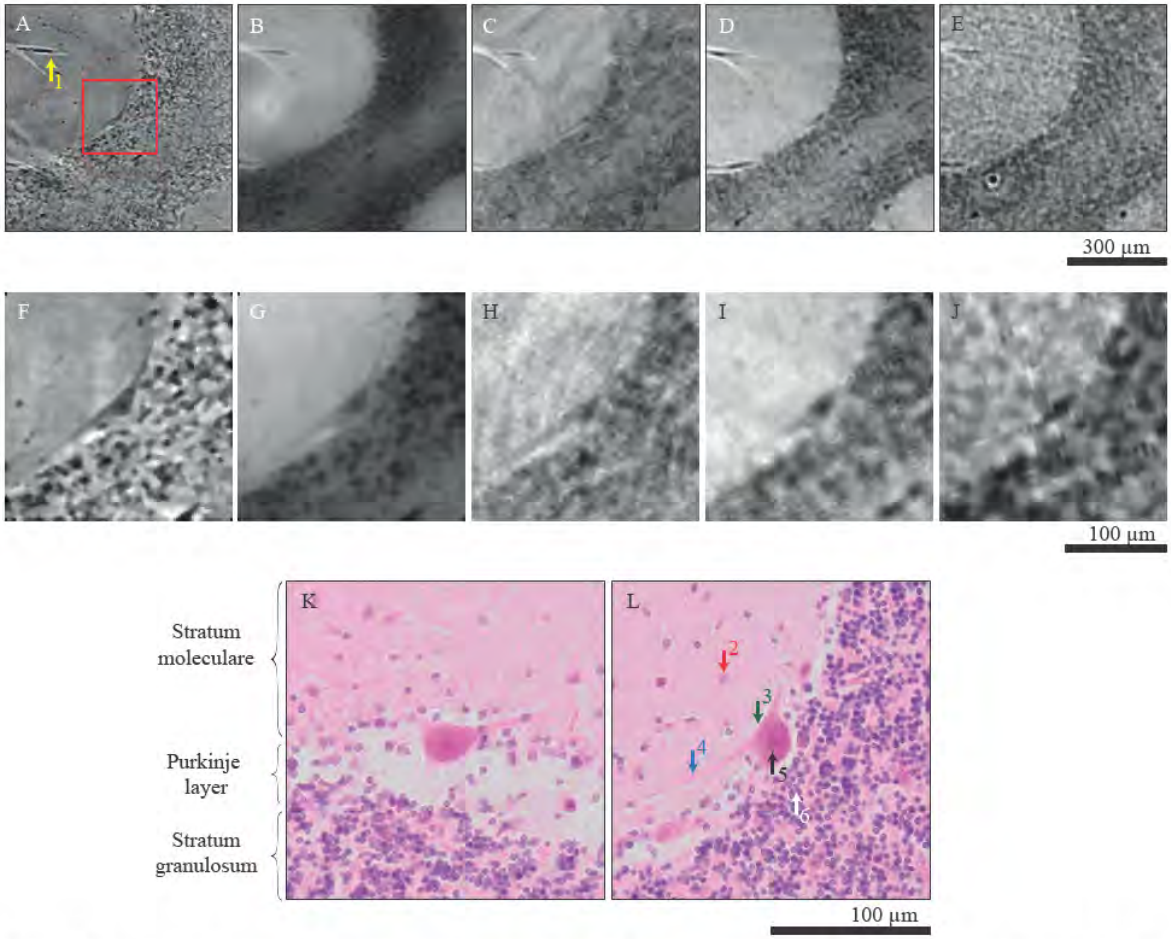

Figure 4. Hard X-ray images of a human cerebellum block showing a tomographic visualization of individual cells with magnification (A - J) and selected cropped histological sections (K - L). A, F: synchrotron radiation based in-line single distance phase contrast tomography with an effective pixel size of 0.45 μm; B, G: synchrotron radiation based in-line single distance phase contrast tomography with an effective pixel size of 1.1 μm; C, H: synchrotron radiation based phase contrast interferometry with a grating period of 8 μm; D, I: synchrotron radiation based phase contrast interferometry with a grating period of 10 μm; E, J: laboratory based absorption contrast μCT; K, L: histology. Yellow arrow (1): blood vessel; Red arrow (2): stellate cell; Green arrow (3): Purkinje cell with dendrite (4, blue); Black arrow (5): nucleus of Purkinje cell; White arrow (6): granular cell.

Figure 4 presents selected registered tomographic slices of a human cerebellum block showing individual cells with magnification (A - J). The tomographic slices are qualitatively compared to the equivalent images of a

FFPE human cerebellum obtained with optical microscopy of H&E-stained section.[26] Analysing Purkinje cells in cerebellum, we can see that in all modalities a comparable number of features can be discriminated, although, stellate cells are only visible in SDPR data. The highest level of detail was achieved for the Fig. 4 A/F and B/G, where one can distinguish cell bodies and neural fibers. This is related to the effective pixels size of the data.

Laboratory-based absorption contrast tomography of FFPE can reach cellular resolution.[26] With a pixel size of 2.2 μm it already enables visualization of the beginning of a dendrite tree, see Figure 4 J. The further increase of resolution can enable visualization of complete neuronal dendrite structures without dedicated contrast agent in 3D within a laboratory environment. It can be expected that laboratory-based absorption contrast tomography with decreased pixel size can enable quantification of the 3D neuronal dendrite structure, for example, bifurcation angles and density, dendritic tree size or fractal dimensions. The method can be used for the identification and quantification of a neural degeneration at early stages and that it has the potential of providing a powerful tool for the quantitative evaluation of cells changes in *post mortem* brain tissues.

3.3 Grating interferometry using laboratory system

Figure 5 shows first reconstruction results for laboratory-based double-grating phase contrast interferometry obtained for human knee sample, consisting of a bony part and a cartilage. The phase contrast slice is shown in Fig. 5 A, conventional absorption contrast in Fig. 5 B and dark-field in Fig. 5 C. Whereas the bony part of the sample looks very similar in the absorption (Fig. 5 B) and phase contrast (Fig. 5 A) images, a difference is visible in the cartilage, which is invisible in the absorption contrast.

Boundaries and interfaces produce a strong signal in the dark-field image.[37] As the bone part is highly porous, it is expected to be clearly visible in dark-field images. The marginal dark-field contrast can be explained by a low contrast-to-noise ratio (CNR) due to a limited number of projections and scanning angle range.

Grating-based phase contrast imaging can provide an important supplementary information to conventional absorption contrast, retrieving X-ray absorption, phase, and dark-field images simultaneously. Combining absorption, phase and dark-field, grating-based tomography offers a powerful multi-modal approach. In future, a further increase in the sensitivity could provide a required contrast for visualisation with a cellular resolution.

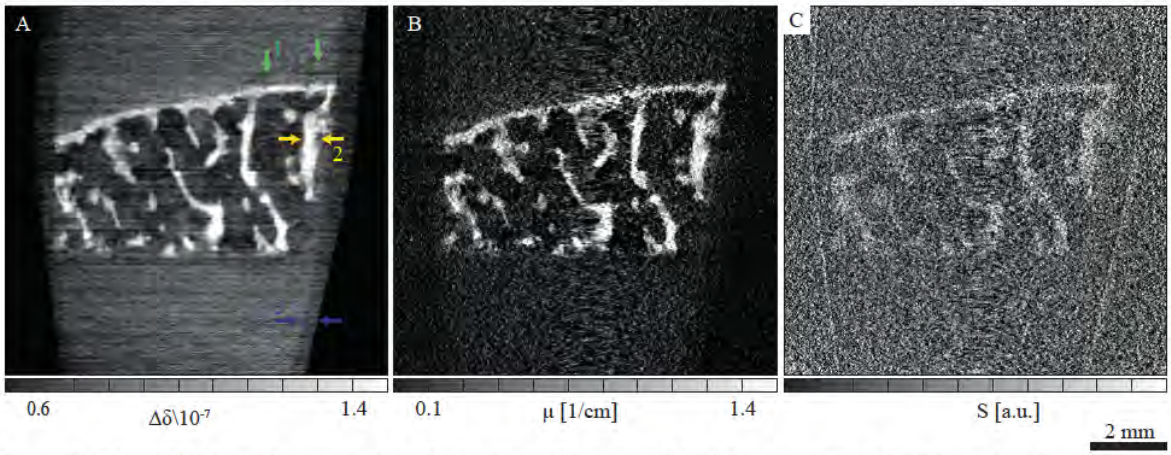

Figure 5. Selected horizontal cross-section of a knee sample measured by laboratory-based double-grating phase contrast tomography. A: phase contrast; B: absorption contrast; C: dark field. Green arrow (1): inhomogeneity in cartilage; Yellow arrow (2): bone structure; Blue arrow (3): container wall.

4. SUMMARY AND OUTLOOK

As it was recently shown, laboratory-based μCT of FFPE sample yields to the absorption contrast, comparable to a conventional histological sections.[26] In this work we have shown that laboratory-based μCT can also provide

data which is almost alike to synchrotron radiation based phase contrast, on the example of human cerebellum specimen.

It is highly beneficial to correlate morphological structures with their cellular functions.[38] X-rays are a powerful tool in non-destructive volumetric imaging of micromorphology. We suggest that laboratory-based tomography could be combined with optical microscopy to characterize 3D structure of soft materials.[39] Within this context, X-ray tomography enables the 3D visualisation and quantification of tissues prior to histological sectioning.[1,40]

In this work, we present selected tomography results of FFPE human cerebellum specimen at varying contrast and resolution. The highest resolution was achieved for synchrotron radiation based in-line single distance phased contrast tomography. We qualitatively compared selected tomography methods, reaching a cellular resolution. In order to identify the appropriate tomography approach to visualize micromorphology of soft tissue a more detailed comparison is required, which should include synchrotron radiation based double-grating interferometry with a water tank, synchrotron radiation based single-grating interferometry with a water tank, etc. Such a comparison should include instrumental and time requirements for data acquisition and reconstruction, as well as data quality and a potential for data combination.

5. ACKNOWLEDGEMENTS

The authors acknowledge the financial support of the Swiss National Science Foundation (SNSF) projects 147172 and SNSF R'Equip project 133802. The authors highly appreciated the assistance of the team of Diamond Synchrotron Radiation Facility, Didcot, UK, particularly Christoph Rau, Joan Vila-Comamala and Pierre Thibault.

REFERENCES

[1] Schulz, G., Weitkamp, T., Zanette, I., Pfeiffer, F., Beckmann, F., David, C., Rutishauser, S., Reznikova, E., and Müller, B., "High-resolution tomographic imaging of a human cerebellum: Comparison of absorption and grating-based phase contrast," *J. R. Soc. Interface* **7**(53), 1665–1676 (2010).

[2] Saba, L., [*Imaging in Neurodegenerative Disorders*], Oxford University Press, Great Clarendon street, Oxford, OX2 6DP (2015).

[3] Praet, J., Santermans, E., Reekmans, K., de Vocht, N., Le Blon, D., Hoornaert, C., Daans, J., Goossens, H., Berneman, Z., Hens, N., Van der Linden, A., and Ponsaerts, P., "Histological characterization and quantification of cellular events following neural and fibroblast(-like) stem cell grafting in healthy and demyelinated CNS tissue," *Methods Mol. Bio.* **1213**, 265–283 (2014).

[4] Miller, L., Wang, Q., Telivala, T., Smith, R., Lanzirotti, A., and Miklossy, J., "Synchrotron-based infrared and X-ray imaging shows focalized accumulation of Cu and Zn co-localized with -amyloid deposits in Alzheimer's disease," *J. Struct. Biol.* **155**(1), 30–37 (2006).

[5] Bourassa, M. and Miller, L., "Metal imaging in neurodegenerative diseases," *Metallomics* **4**(8), 721–738 (2012).

[6] Leskovjan, A., Lanzirotti, A., and Miller, L., "Amyloid plaques in PSAPP mice bind less metal than plaques in human Alzheimer's disease," *NeuroImage* **47**(4), 1215–1220 (2009).

[7] Papp, E., Leergaard, T., Csucs, G., and Bjaalie, J., "Brain-wide mapping of axonal connections: Workflow for automated detection and spatial analysis of labeling in microscopic sections," *Front. Neuroinform.* **10**, 11 (2016).

[8] Schulz, G., Weitkamp, T., Zanette, I., Pfeiffer, F., Müller-Gerbl, M., David, C., and Müller, B., "Asymmetric rotational axis reconstruction of grating-based X-ray phase contrast tomography of the human cerebellum," *Proc. SPIE* **8506**, 850604 (2012).

[9] Lichtman, J., Pfister, H., and Shavit, N., "The big data challenges of connectomics," *Nat. Neurosci.* **17**(11), 1448–1454 (2014).

[10] Kasthuri, N., Hayworth, K., Berger, D., Schalek, R., Conchello, J., Knowles-Barley, S., Lee, D., Vázquez-Reina, A., Kaynig, V., Jones, T., Roberts, M., Morgan, J., Tapia, J., Seung, H., Roncal, W., Vogelstein, J., Burns, R., Sussman, D., Priebe, C., Pfister, H., and Lichtman, J., "Saturated reconstruction of a volume of neocortex," *Cell* **162**(3), 648–661 (2015).

[11] Oh, S. W., Harris, J. A., Ng, L., Winslow, B., Cain, N., Mihalas, S., Wang, Q., Lau, C., Kuan, L., Henry, A. M., Mortrud, M. T., Ouellette, B., Nguyen, T. N., Sorensen, S. A., Slaughterbeck, C. R., Wakeman, W., Li, Y., Feng, D., Ho, A., Nicholas, E., Hirokawa, K. E., Bohn, P., Joines, K. M., Peng, H., Hawrylycz, M. J., Phillips, J. W., Hohmann, J. G., Wohnoutka, P., Gerfen, C. R., Koch, C., Bernard, A., Dang, C., Jones, A. R., and Zeng, H., "A mesoscale connectome of the mouse brain," *Nature* **508**(7495), 207–214 (2014).

[12] Ichimura, K., Miyazaki, N., Sadayama, S., Murata, K., Koike, M., Nakamura, K.-I., Ohta, K., and Sakai, T., "Three-dimensional architecture of podocytes revealed by block-face scanning electron microscopy," *Sci. Rep.* **5**, 8993 (2015).

[13] Krauth, A., Blanc, R., Poveda, A., Jeanmonod, D., Morel, A., and Székely, G., "A mean three-dimensional atlas of the human thalamus: Generation from multiple histological data," *NeuroImage* **49**(3), 2053–2062 (2010).

[14] Chung, K., Wallace, J., Kim, S.-Y., Kalyanasundaram, S., Andalman, A. S., Davidson, T. J., Mirzabekov, J. J., Zalocusky, K. A., Mattis, J., Denisin, A. K., Pak, S., Bernstein, H., Ramakrishnan, C., Grosenick, L., Gradinaru, V., and Deisseroth, K., "Structural and molecular interrogation of intact biological systems," *Nature* **497**(7449), 332–337 (2013).

[15] Murray, E., Cho, J. H., Goodwin, D., Ku, T., Swaney, J., Kim, S.-Y., Choi, H., Park, Y.-G., Park, J.-Y., Hubbert, A., McCue, M., Vassallo, S., Bakh, N., Frosch, M. P., Wedeen, V. J., Seung, H. S., and Chung, K., "Simple, scalable proteomic imaging for high-dimensional profiling of intact systems," *Cell* **163**(6), 1500–1514 (2015).

[16] Krenkel, M., Markus, A., Bartels, M., Dullin, C., Alves, F., and Salditt, T., "Phase-contrast zoom tomography reveals precise locations of macrophages in mouse lungs," *Sci. Rep.* **5**, 9973 (2015).

[17] Lang, S., Zanette, I., Dominietto, M., Langer, M., Rack, A., Schulz, G., Le Duc, G., David, C., Mohr, J., Pfeiffer, F., Müller, B., and Weitkamp, T., "Experimental comparison of grating- and propagation-based hard X-ray phase tomography of soft tissue," *J. Appl. Phys.* **116**(15), 154903 (2014).

[18] Schulz, G., Morel, A., Imholz, M., Deyhle, H., Weitkamp, T., Zanette, I., Pfeiffer, F., David, C., Müller-Gerbl, M., and Müller, B., "Evaluating the microstructure of human brain tissues using synchrotron radiation-based micro computed tomography," *Proc. SPIE* **7804**, 78040F (2010).

[19] Müller, B., Deyhle, H., Lang, S., Schulz, G., Bormann, T., Fierz, F., and Hieber, S., "Three-dimensional registration of tomography data for quantification in biomaterials science," *Int. J. Mater. Res.* **103**(2), 242–249 (2012).

[20] Germann, M., Morel, A., Beckmann, F., Andronache, A., Jeanmonod, D., and Müller, B., "Strain fields in histological slices of brain tissue determined by synchrotron radiation-based micro computed tomography," *J. Neurosci. Meth.* **170**(1), 149–155 (2008).

[21] Hieber, S. E., Bikis, C., Khimchenko, A., Schweighauser, G., Hench, J., Chicherova, N., Schulz, G., and Müller, B., "Tomographic brain imaging with nucleolar detail and automatic cell counting," *Sci. Rep.* **6**, 32156 (2016).

[22] Zehbe, R., Haibel, A., Riesemeier, H., Gross, U., Kirkpatrick, C., Schubert, H., and Brochhausen, C., "Going beyond histology. Synchrotron micro-computed tomography as a methodology for biological tissue characterization: From tissue morphology to individual cells," *J. R. Soc. Interface* **7**(42), 49–59 (2010).

[23] Huang, S., Kou, B., Chi, Y., Xi, Y., Cao, Y., Cui, W., Hu, X., Shao, Z., Guo, H., Fu, Y., Xiao, T., Sun, J., Zhao, J., Wang, Y., and Wu, J., "In-line phase-contrast and grating-based phase-contrast synchrotron imaging study of brain micrometastasis of breast cancer," *Sci. Rep.* **5**, 9418 (2015).

[24] Zehbe, R., Schmitt, V. H., Kirkpatrick, C. J., and Brochhausen, C., "High resolution X-ray tomography - Three-dimensional characterisation of cell-scaffold constructs for cartilage tissue engineering," *Mater. Sci. Tech. (UK)* **31**(2), 167–173 (2015).

[25] Langer, M., Pacureanu, A., Suhonen, H., Grimal, Q., Cloetens, P., and Peyrin, F., "X-Ray phase nanotomography resolves the 3D human bone ultrastructure," *PLoS ONE* **7**, 8 (2012).

[26] Khimchenko, A., Deyhle, H., Schulz, G., Schweighauser, G., Hench, J., Chicherova, N., Bikis, C., Hieber, S., and Müller, B., "Extending two-dimensional histology into the third dimension through conventional micro computed tomography," *NeuroImage* **139**, 26–36 (2016).

[27] Götz, C., "Comparing absorption and phase contrast modes in micro computed tomography measurements of osteochondral specimens of the human knee," *Masters thesis in Sport Sciences, University of Basel* (2015).
[28] General Electric, Measurement and Control, "Phoenix nanotom m 180 kV / 20 W X-ray nanoCT system for high-resolution analysis and 3D metrology, https://www.gemeasurement.com/inspection-ndt/radiography-and-computed-tomography/phoenix-nanotom-m," (26.09.2016).
[29] Egbert, A. and Brunke, O., "High-resolution X-ray computed tomography for materials research," *Adv. Mat. Res.* **222**, 48–51 (2011).
[30] Khimchenko, A., Schulz, G., Deyhle, H., Hieber, S., Hasan, S., Bikis, C., Schulz, J., Costeur, L., and Müller, B., "Non-destructive phase contrast hard X-ray imaging to reveal the three-dimensional microstructure of soft and hard tissues," *Proc. SPIE* **9797**, 97970B (2016).
[31] Weitkamp, T., Diaz, A., David, C., Pfeiffer, F., Stampanoni, M., Cloetens, P., and Ziegler, E., "X-ray phase imaging with a grating interferometer," *Opt. Express* **13**(16), 6296–6304 (2005).
[32] Rau, C., Wagner, U., Pešić, Z., and De Fanis, A., "Coherent imaging at the Diamond beamline I13," *Phys. Stat. Sol.* **208**(11), 2522–2525 (2011).
[33] Haas, W., Bech, M., Bartl, P., Bayer, F., Ritter, A., Weber, T., Pelzer, G., Willner, M., Achterhold, K., Durst, J., Michel, T., Prümmer, M., Pfeiffer, F., Anton, G., and Hornegger, J., "Phase-unwrapping of differential phase-contrast data using attenuation information," *Proc. SPIE* **7962**, 79624R (2011).
[34] Weitkamp, T., Haas, D., Wegrzynek, D., and Rack, A., "ANKAphase: Software for single-distance phase retrieval from inline X-ray phase-contrast radiographs," *J. Synchrotron Rad.* **18**(4), 617–629 (2011).
[35] Andronache, A., von Siebenthal, M., Székely, G., and Cattin, P., "Non-rigid registration of multi-modal images using both mutual information and cross-correlation," *Med. Image Anal.* **12**(1), 3–15 (2008).
[36] Zanette, I., Lang, S., Rack, A., Dominietto, M., Langer, M., Pfeiffer, F., Weitkamp, T., and Müller, B., "Holotomography versus x-ray grating interferometry: A comparative study," *Applied Physics Letters* **103**(24), 244105 (2013).
[37] Pfeiffer, F., Bech, M., Bunk, O., Kraft, P., Eikenberry, E., Brönnimann, C., Grünzweig, C., and David, C., "Hard X-ray dark-field imaging using a grating interferometer," *Nat. Mater.* **7**(2), 134–137 (2008).
[38] Miller, L. and Dumas, P., "From structure to cellular mechanism with infrared microspectroscopy," *Curr. Opin. Struct. Biol.* **20**(5), 649–656 (2010).
[39] Walton, L., Bradley, R., Withers, P., Newton, V., Watson, R., Austin, C., and Sherratt, M., "Morphological characterisation of unstained and intact tissue micro-architecture by X-ray computed micro- and nano-tomography," *Sci. Rep.* **5**, 10074 (2015).
[40] Wenz, J., Schleede, S., Khrennikov, K., Bech, M., Thibault, P., Heigoldt, M., Pfeiffer, F., and Karsch, S., "Quantitative X-ray phase-contrast microtomography from a compact laser-driven betatron source," *Nat. Commun.* **6**, 7568 (2015).

Chapter 3

Laboratory-based phase-contrast tomography

Implementation of a double-grating interferometer for phase-contrast computed tomography in a conventional system nanotom® m

A. Khimchenko, G. Schulz, P. Thalmann, B. Müller,

APL Bioengineering (submitted)

Implementation of a double-grating interferometer for phase contrast computed tomography in a conventional system nanotom® m

A. Khimchenko,[1] G. Schulz,[1, a)] P. Thalmann,[1] and B. Müller[1]
Biomaterials Science Center, University of Basel, Allschwil, Switzerland

(Dated: 22 May 2017)

In this communication, we present the integration of X-ray double-grating interferometer (XDGI) into an advanced, commercially available micro computed tomography system nanotom® m with a transmission X-ray source and a micrometre-sized focal spot. The performance of the interferometer is demonstrated by comparing the registered three-dimensional images of a human knee joint piece in phase and conventional absorption contrast modes. XDGI provides enough contrast (1.094 ± 0.152) to identify the cartilage layer, which is not recognized in the conventional mode. Consequently, the two modes are complementary, as the present XDGI set-up only reaches a spatial resolution of (73 ± 6) µm, whereas the true micrometre resolution in absorption has been proven. The XDGI is especially supportive for soft tissue imaging and for the visualization of weak X-ray absorbing species in the direct neighborhood of stronger absorbing components.

I. INTRODUCTION

Micro computed tomography (µCT) based on conventional X-ray sources usually operates in the absorption contrast mode. Main disadvantages of this technique are a limited contrast in materials composed of a low atomic number Z elements and an absence of quantitative information. Simultaneous visualization of soft and hard tissues is a challenge too. For an optimized choice of the photon energy, weak absorbing parts do not provide sufficient contrast, thus, staining procedures are often required[1,2], whereas hard parts show the streak and beam hardening artifacts characteristic for low photon energies. In addition, determination of an effective photon energy of a polychromatic spectrum is complex and gray values cannot be related easily to a local X-ray absorption.

Phase imaging is often preferred over conventional absorption contrast for soft tissue imaging[3,4] and for the visualization of weak X-ray absorbing species in the direct neighborhood of stronger absorbing components[5]. As a consequence, several researchers have built CT systems working in the phase contrast mode[6–8]. In quantitative visualization using polychromatic sources grating interferometry is especially powerful[9]. The three-grating set-up works with conventional sources[10–12]. Measurements in a Talbot configuration with two gratings are performed with micro-focus tubes[13], multiline[14] and liquid-metal-jet[15] sources. However, Talbot interferometer set-up realization, within a commercial laboratory absorption contrast µCT system with a transmission polychromatic source for tomographic imaging, remains a challenge due to restrictions in system dimensions, limited flux, and a micrometre-sized X-ray source. The extension of a commercially available µCT system by a grating set-up is particularly interesting, as phase contrast leads to a complementary and quantitative information which enables multi-modal imaging of soft and hard tissue components in a single advanced apparatus without the requirement of building a complete system.

We propose the integration of a symmetrical[12] X-ray double-grating interferometer (XDGI) into an advanced commercial µCT system nanotom® m (GE Sensing & Inspection Technologies GmbH, Wunstorf, Germany). The main advantages of the symmetrical set-up compared to the asymmetrical are the straightforward grating positioning, flexibility and set-up costs reduction as the same mask can be used for fabrication of both gratings. Nevertheless, higher sensitivities can be obtained by an asymmetric set-up as higher Talbot orders can be adjusted. The purpose of the present study is to make a direct comparison between phase and absorption contrast tomography performed within a laboratory µCT system nanotom® m in order to highlight the added value of extension by a grating set-up.

II. MATERIALS AND METHODS

In order to test the applicability of a laboratory µCT system, extended to phase contrast, we measured a human knee joint piece, consisting of bone and cartilage layers, obtained post-mortem from an 87-year-old female body donated to the Institute of Anatomy, University of Basel, Switzerland. All donors of the program contributed their body to education and research purposes. All procedures were conducted in accordance with the Declaration of Helsinki. Experts extracted the knee piece from the surface of the tibia by a metal cylinder, subsequent formalin fixated and kept in an eppendorf container.

A double-grating symmetric interferometric set-up[16], see Figure 1, was incorporated into the advanced µCT system nanotom® m equipped with a 180 kV/15 W nanofocus® transmission tube with an adjustable focal spot diameter (0.9 - 2.7 µm) and operated with a tungsten target[17]. The system has a temperature stabilized digital GE DXR 500L detector with a pixel length of

a)Electronic mail: georg.schulz@unibas.ch

TABLE I. Tomography parameters and a quantitative comparison of the acquired data. "Phase": laboratory-based phase contrast tomography via a double-grating set-up integrated into a commercially available µCT system nanotom® m, "Absorption 1": absorption contrast tomography by nanotom® m with a comparable set-up to interferometry, Absorption 2": absorption contrast tomography by nanotom® m with optimized settings, U: acceleration voltage, I: current, N: number of projections, t: exposure time, t^*: total exposure time for a single phase stepping image, l: effective pixel size, d_p: sample detector distance, d_o: focus sample distance, CNR: contrast-to-noise ratio between cartilage and formalin, SR: edge-based spatial resolution.

Scan	U [kVp]	I [µA]	N	t [s]	l [µm]	d_p [mm]	d_o [mm]	CNR	SR [µm]
Phase	42	275	600	10.0*	23.3	460.0	140.0	1.094 ± 0.152	73 ± 6
Absorption 1	42	275	600	70.0	23.3	460.0	140.0	0.073 ± 0.007	59 ± 5
Absorption 2	42	380	600	3.0	23.3	172.5	52.5	0.287 ± 0.003	60 ± 5

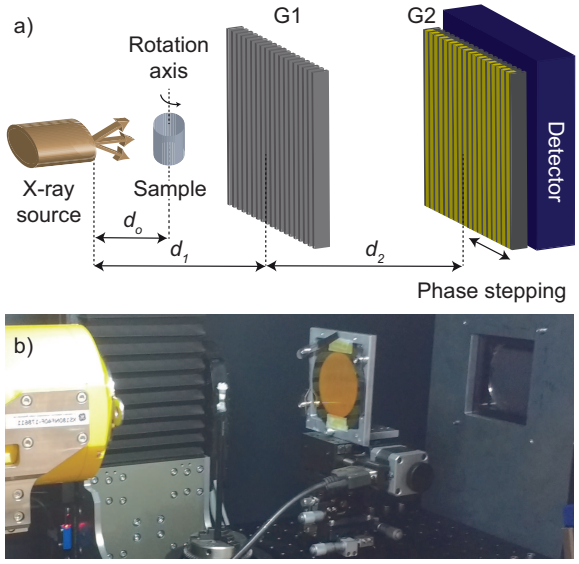

FIG. 1. (a) Scheme and (b) realization within the µCT system nanotom® m of a cone-beam double-grating interferometric set-up. G1: phase grating; G2: analyzer grating; d_1: distance from the source to phase grating G1; d_2: distance from the phase to analyzer grating G2; d_o: distance from the source to sample. The sample is mounted on the tomographic rotation stage and placed in front of G1, whereas G2 is positioned close to the detector.

100 µm (3072 × 2400 pixels) based on endurance™ scintillator technology[18]. XDGI measurements were performed using a phase grating G1 with a periodicity of 7 µm and a Si structure height of 200 µm, in order to achieve a phase shift of π for photons with the energy of 30 keV, corresponding to an estimated acceleration voltage of 42 kVp[16]. The gold lines of the analyzer grating G2 had a structure height of 85 µm with a periodicity of 7 µm. Inter-grating distances corresponds to the first fractional Talbot order, where phase grating G1 is positioned at a distance of $d_1 = 29.6$ cm downstream from the source, and analyzer grating just in front of the detector $d_2 = 29.6$ cm. Analyzing the visibility map, see Figure 2j, one can see that for the proposed set-up with the selected source-to-G2 distance, grating diameter and design energy shadowing effect can be neglected, thus curved gratings are not required as was shown by Thüring et al.[8]. Nevertheless, one has to use a curved grating in order to match the beam divergence with bigger gratings or operating a set-up for higher energies. A phase-stepping technique that allows the extraction of phase, absorption and dark-field signal[19], where G2 was scanned over two periods of the interference pattern in seven phase steps, was used. For the tomography, 600 equiangular projections over 360° with the total exposure time per single phase stepping image of 10 s (2 × 5 s) were acquired. Reference (without a sample) and dark-field (without X-ray beam) images were taken every 50 angular positions. Additional experimental parameters are listed in Table I. The phase recovery and parallel-beam reconstruction using the filtered back-projection algorithm[20,21] of the data were carried out in MATLAB R2016b (MathWorks, Natick, USA). The raw data were median-filtered for noise reduction (kernel size 3 × 3). To correct for cone-beam geometry, phase projections were renormalized[22] by a factor of $\frac{d_1}{d_o} = 2.11$, where d_o denotes the focus sample distance.

Absorption contrast tomography experiments were carried out in µCT system nanotom® m. Experimental parameters are listed in Table I. Data processing and reconstruction were done automatically, using datos|x 2.0 software (phoenix|x-ray, GE Sensing & Inspection Technologies GmbH, Wunstorf, Germany), which implements cone-beam reconstruction based on Feldkamps algorithm[23]. The scanning parameters for "Absorption 1" were optimized in order to be comparable to the grating interferometry, although they were not optimal for absorption contrast imaging.

For the comparison of parallel-beam reconstruction using the filtered back-projection algorithm with Hilbert filter implemented in Matlab and optimized cone-beam reconstruction based on Feldkamps algorithm implemented in datos|x 2.0 raw projections were cropped and integrated. For the reconstruction in datos|x the intensity in raw projections was normalized.

For the quantitative comparison of the datasets, rigid registration with nearest-neighbour interpolation using the library provided by ITK[24,25] was used. The trans-

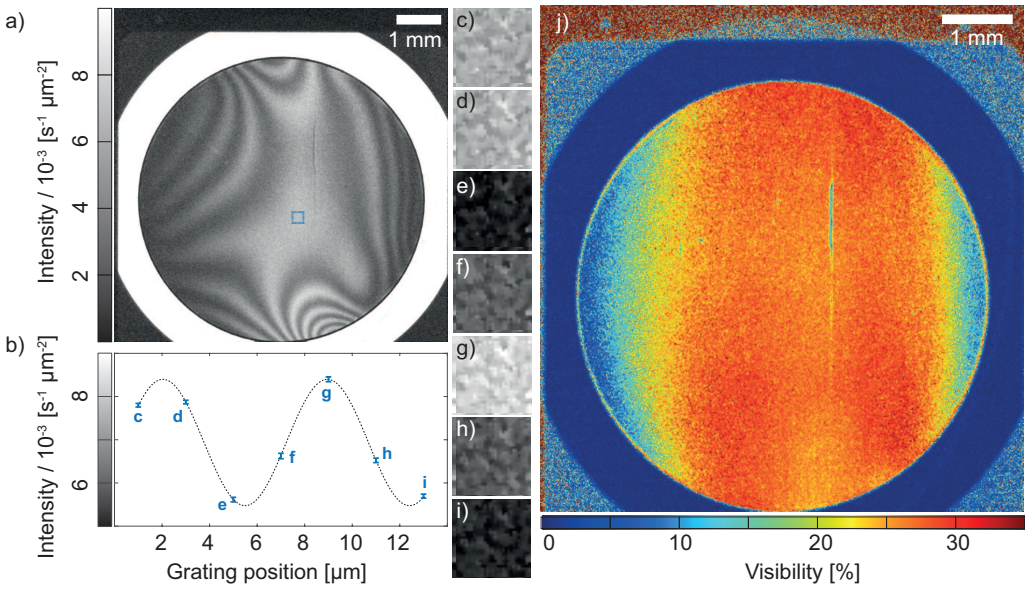

FIG. 2. (a) Interference pattern at the first fractional Talbot distance. (b) Stepping curve: mean intensity oscillations in the centre of the field of view (30 × 30 detector pixels) over seven grating positions (c - i). Measurement was performed with the total exposure time per single phase stepping image of 10 s (2 × 5 s) in "*mode 1*". (j) Visibility map.

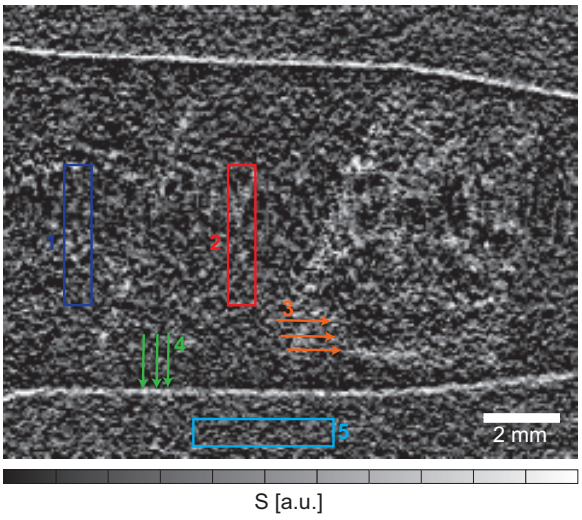

FIG. 3. Selected horizontal cross-section of a knee sample measured by laboratory-based double-grating set-up in dark-field mode. Dark blue (1): formalin, Red (2): cartilage, Orange (3): bone, Green (4): container wall, Light blue (5): air.

lation registration of the datasets for the comparison between parallel and cone-beam reconstruction was performed separately.

The quantitative comparison was based on the calculation of a contrast-to-noise ratio (CNR) and an edge-based spatial resolution (SR). CNR was defined as $|I_1 - I_2|/\sigma_2$, where I denotes the mean intensity of the volume of interest (VOI) and σ is the standard deviation of the gray value within this volume. VOIs = 124 × 20 × 24 voxels were selected within the cartilage and formalin from the same location within each dataset. The gray values within VOIs were fitted with Gaussians[26] to extract I and σ. To estimate the upper limit of SR[25], we chose a region at the bone-cartilage interface. In order to reduce noise effects, the profile line was *smoothed* using a moving average filter with a span of five.

III. RESULTS AND DISCUSSION

The interference pattern induced by phase grating is shown in Figure 2b. Mean visibility, based on Fourier analysis in the centre of the field of view (FOV = 30 × 30 pixels) was (25.6 ± 0.7)% for "*mode 1*" with an estimated source size of 2.0 µm, see Figure 2j, (33.0 ± 0.7)% for "*mode 2*" with an estimated source size of 1.0 µm, and (32.8 ± 2.0)% for "*mode 3*" with an estimated source size of around 0.9 µm. Due to the source size (2.0 - 2.7 µm), an interference pattern was not observed in "*mode 0*", thus visibility values can not be calculated. An average detector counts per pixel for "*mode 1*" were higher than for "*mode 2*"and "*mode 3*"(336 ± 7 versus 163 ± 7 and 133 ± 7, respectively). Thus, the highest set-up sensitivity[12] is achieved at "*mode 1*", which was used for the tomographic scans.

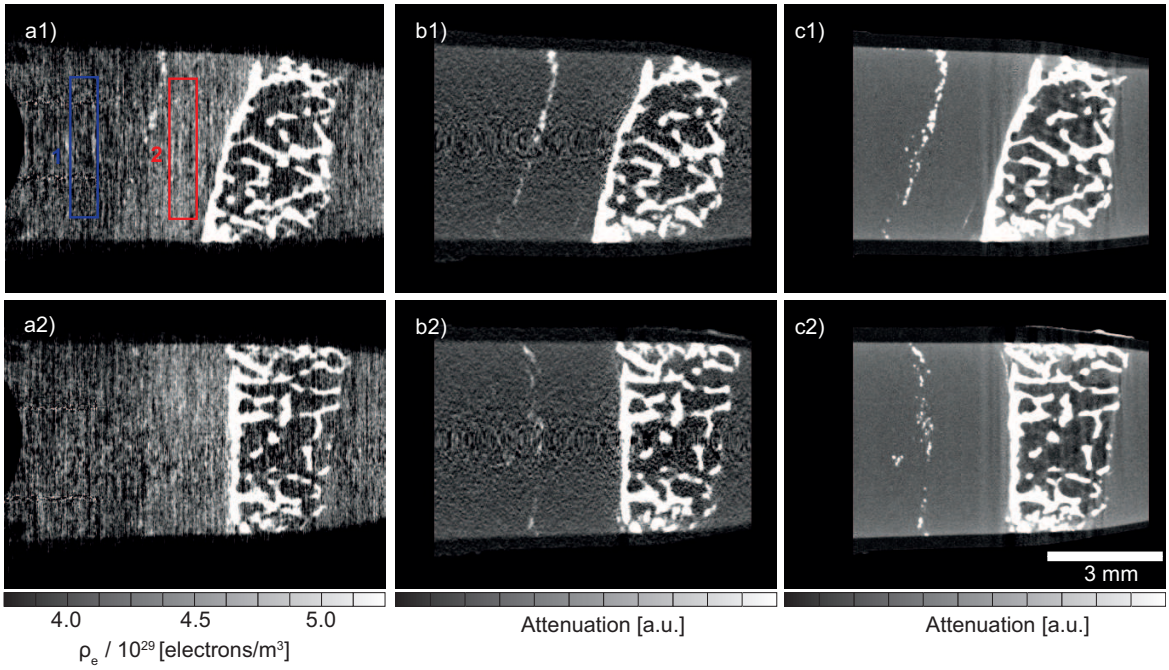

FIG. 4. Qualitative comparison of the data acquired by a laboratory-based double-grating phase contrast set-up and advanced absorption contrast µCT system. Registered tomographic slices of human knee joint sample measured by grating interferometry - "Phase" (a), absorption contrast µCT system nanotom® m with a comparable - "Absorption 1" (b) and optimized settings - "Absorption 2" (c). Dark blue (1): formalin, Red (2): cartilage. Scanning parameters are listed in Table I.

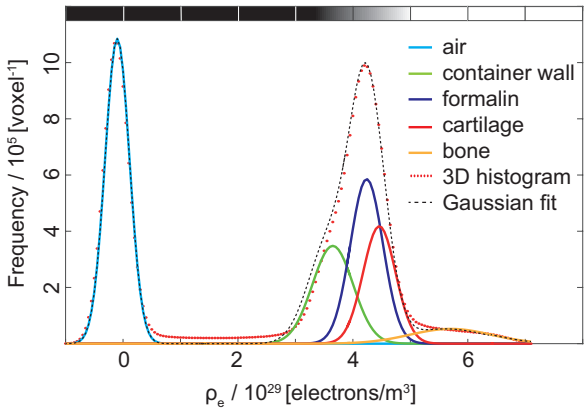

FIG. 5. Three-dimensional histogram of a knee sample measured in the phase contrast mode and a multi-Gaussian fit to the corresponding histogram.

Grating interferometry is a multi-modal imaging technique, providing absorption, phase and dark-field signals simultaneously[27]. Homogeneous specimens, such as soft tissues, lead to a negligible scattering, whereas ones with microscopic electron density fluctuations such as bone give rise to a scattering signal. Therefore, the structures in cartilage are hardly visible, as represented in Figure 3.

Figure 4 shows characteristic, registered cross-sections of a knee joint piece provided by phase and absorption contrast modes: laboratory-based double-grating phase contrast set-up Fig. 4a, absorption contrast with a set-up comparable to interferometry Fig. 4b and absorption contrast with optimized set-up Fig. 4c. Whereas the bony part of the sample is comparable in the absorption Fig. 4b - c and phase contrast Fig. 4a images, a difference is seen in the cartilage which is invisible in the absorption contrast measurements. While the contrast gain for soft tissue visualization between phase and absorption contrast modes is the expected result[28–30], purpose of the provided comparison is to highlight the added value of grating interferometer incorporated into the µCT system with transmission source. Cartilage is involved in degenerative changes of a knee joint. The ability of assessment of pathologic changes in a knee cartilage within a laboratory environment using not only magnetic resonance imaging (MRI)[31], but also hard X-ray can be beneficial for a broad range of biomedical applications.

When comparing results from the phase and absorption contrast modes, it can be noted that XDGI provides images with a lower SR compared to ones acquired in the absorption contrast mode. The results of a quantitative comparison are summarized in Table I. A three-dimensional histogram of a knee sample measured in the phase contrast mode and a multi-Gaussian fit to the corresponding histogram is shown in Figure 5.

We have verified that the reconstruction using the assumption of the parallel- or cone-beam has a neglectable effect on the final result. Both reconstructions yielded almost identical results in terms of density and spatial resolutions. The result is expected as the cone angle is less than 4°.

Medical applications often rely on a quantitative interpretation of gray-scale value, for example, in the assessment of bone density[9,32]. One advantage of XDGI is the ability to provide quantitative information about the decrement δ of the complex refractive index n: $\delta_{cartilage} = (3.42 \pm 0.19) \times 10^{-7}$ and $\delta_{formalin} = (3.25 \pm 0.23) \times 10^{-7}$. The typical quantity of interest is electron density $\rho_e = 2\pi\delta/r_0\lambda^2$, where ρ_e is electron density, r_0 - electron radius and λ - X-ray wavelength. Calculated electron density of formalin is $\rho_{eformalin}$= (4.24 $\pm$ 0.03) $\times$ 10^{29} electrons/m^3 and of cartilage $\rho_{ecartilage}$= (4.46 $\pm$ 0.03) $\times$ 10^{29} electrons/m^3. These values were estimated within VOIs = 180 $\times$ 40 $\times$ 40 voxels. Experimental values are in the same order of magnitude as those found in the literature[3,33].

In order to take accurate electron density measurements, calibration with a reference can be beneficial. Thus, a phantom consisting of polypropylene (PP), polyether ether ketone (PEEK) and polyoxymethylene (POM) discs with an average diameter of 6 mm was used. Measurement was performed with an effective pixel size of 23.1 µm. After reconstruction the acquired data was median-filtered 3 $\times$ 3 for noise reduction. Electron densities, calculated within VOI = 120 $\times$ 20 $\times$ 100 voxels within each disc, are: ρ_{ePP} = (3.86 $\pm$ 0.05) $\times$ 10^{29} electrons/m^3, ρ_{ePEEK} =(4.87 $\pm$ 0.07) $\times$ 10^{29} electrons/m^3 and ρ_{ePOM} (5.44 $\pm$ 0.06) $\times$ 10^{29} electrons/m^3. We have identified a deviation from literature values[34,35]. The polychromatic nature of the X-ray source, for example, can explain an offset or a shift in electron density. Thus, a precise calibration needs values of phantoms acquired at monochromatic beams.

IV. CONCLUSION AND OUTLOOK

In conclusion, we present in this study an integration of X-ray double-grating interferometer into an advanced, commercially available µCT system nanotom® m with a transmission X-ray source and a micrometre-sized focal spot. We demonstrate the performance of this three-dimensional phase imaging by comparing the results of a human knee joint piece in phase and a conventional absorption contrast modes. Despite the lower SR of XDGI by a factor of approximately 1.2, the contrast was sufficient to identify the cartilage layer, thereby showing an improvement of the CNR between cartilage and formalin by a factor of about four. Thus, the overall quality factor[36] is increased. The proposed set-up demonstrates sufficient stability for tomographic scans, by which the electron density values can be retrieved. Nevertheless, the precise set-up calibration is required. Our results suggest that the extension of a commercially available µCT system via grating interferometer offers the potential to fill the gap between laboratory-based absorption contrast µCT and phase contrast µCT using synchrotron radiation or conventional sources in the quantitative visualization of soft tissues.

The most important further step for biomedical applications would be the increase of the FOV by fabrication of bigger gratings, as currently the field of view is limited to 23 mm at the detector plane. At this point one has to take care that a curvature of the gratings will be essential in order to eliminate visibility decay towards the lateral directions. In order to increase the sensitivity of the grating interferometer an asymmetric set-up working at a higher Talbot order with decreased period of analyzer grating p_2 will be realized. For bigger or higher absorbing specimens a set-up for higher energies can be implemented.

V. ACKNOWLEDGEMENTS

The authors thank C. Götz of the Biomaterials Science Center, University of Basel, and M. Müller-Gerbl of Musculoskeletal Research, Department of Biomedicine, University of Basel, for providing the knee sample, and Sascha Martin of the Department of Physics, University of Basel, for the plastic phantom. The financial contribution of Swiss National Science Foundation (SNSF) projects 147172 and 144535 and R'Equip project 133802 is highly acknowledged.

[1] B. Metscher, "Micro CT for comparative morphology: Simple staining methods allow high-contrast 3D imaging of diverse non-mineralized animal tissues," BMC Physiol. **9** (2009).

[2] B. Müller, J. Fischer, U. Dietz, P. Thurner, and F. Beckmann, "Blood vessel staining in the myocardium for 3D visualization down to the smallest capillaries," Nucl. Instrum. Methods Phys. Res. B **246**, 254–261 (2006).

[3] I. Zanette, S. Lang, A. Rack, M. Dominietto, M. Langer, F. Pfeiffer, T. Weitkamp, and B. Müller, "Holotomography versus x-ray grating interferometry: A comparative study," Appl. Phys. Lett. **103**, 244105 (2013).

[4] A. Momose, W. Yashiro, Y. Takeda, Y. Suzuki, and T. Hattori, "Phase tomography by X-ray Talbot interferometry for biological imaging," Jpn. J. Appl. Phys. **45**, 5254–5262 (2006).

[5] M. N. Holme, G. Schulz, H. Deyhle, T. Weitkamp, F. Beckmann, J. A. Lobrinus, F. Rikhtegar, V. Kurtcuoglu, I. Zanette, T. Saxer, and B. Müller, "Complementary X-ray tomography techniques for histology-validated 3D imaging of soft and hard tissues using plaque-containing blood vessels as examples," Nat. Protocols **9**, 1401–1415 (2014).

[6] D. Larsson, W. Vågberg, A. Yaroshenko, A. Yildirim, and H. Hertz, "High-resolution short-exposure small-animal labo-

ratory x-ray phase-contrast tomography," Sci. Rep. **6**, 39074 (2016).
[7]P. Bidola, K. Morgan, M. Willner, A. Fehringer, S. Allner, F. Prade, F. Pfeiffer, and K. Achterhold, "Application of sensitive, high-resolution imaging at a commercial lab-based X-ray micro-CT system using propagation-based phase retrieval," J. Microsc. **00**, 1–10 (2017).
[8]T. Thuering, P. Modregger, T. Grund, J. Kenntner, C. David, and M. Stampanoni, "High resolution, large field of view x-ray differential phase contrast imaging on a compact setup," Appl. Phys. Lett. **99**, 041111 (2011).
[9]J. Herzen, T. Donath, F. Pfeiffer, O. Bunk, C. Padeste, F. Beckmann, A. Schreyer, and C. David, "Quantitative phase-contrast tomography of a liquid phantom using a conventional x-ray tube source," Opt. Express **17**, 10010–10018 (2009).
[10]F. Pfeiffer, T. Weitkamp, O. Bunk, and C. David, "Phase retrieval and differential phase-contrast imaging with low-brilliance X-ray sources," Nat. Phys. **2**, 258–261 (2006).
[11]T. Thüring, M. Abis, Z. Wang, C. David, and M. Stampanoni, "X-ray phase-contrast imaging at 100 keV on a conventional source," Sci. Rep. **4**, 5198 (2014).
[12]L. Birnbacher, M. Willner, A. Velroyen, M. Marschner, A. Hipp, J. Meiser, F. Koch, T. Schröter, D. Kunka, J. Mohr, F. Pfeiffer, and J. Herzen, "Experimental realisation of high-sensitivity laboratory X-ray grating-based phase-contrast computed tomography," Sci. Rep. **6**, 24022 (2016).
[13]K.-H. Yoon, J. Ryu, C. Jung, C. Ryu, Y. Kim, Y. Kwon, M. Park, S. Cho, and K. Chon, "Differential X-ray phase-contrast imaging with a grating interferometer using a laboratory X-ray microfocus tube," J. Korean Phys. Soc. **65**, 2111–2116 (2014).
[14]A. Momose, W. Yashiro, H. Kuwabara, and K. Kawabata, "Grating-based x-ray phase imaging using multiline x-ray source," Jpn. J. Appl. Phys. **48**, 076512 (2009), cited By 37.
[15]T. Zhou, U. Lundström, T. Thüring, S. Rutishauser, D. Larsson, M. Stampanoni, C. David, H. Hertz, and A. Burvall, "Comparison of two x-ray phase-contrast imaging methods with a microfocus source," Opt. Express **21**, 30183–30195 (2013).
[16]A. Khimchenko, G. Schulz, H. Deyhle, S. E. Hieber, S. Hasan, C. Bikis, J. Schulz, L. Costeur, and B. Müller, "Non-destructive phase contrast hard x-ray imaging to reveal the three-dimensional microstructure of soft and hard tissues," Proc. SPIE **9797**, 97970B (2016).
[17]A. Egbert and O. Brunke, "High-resolution X-ray computed tomography for materials research," Adv. Mat. Res. **222**, 48–51 (2011).
[18]DXR500L Static Digital Detector Array, Direct Radiography, GE Sensing & Inspection Technologies GmbH, https://www.gemeasurement.com/inspection-ndt/radiography-and-computed-tomography/dxr500l-static-digital-detector-array (2016).
[19]T. Weitkamp, A. Diaz, C. David, F. Pfeiffer, M. Stampanoni, P. Cloetens, and E. Ziegler, "X-ray phase imaging with a grating interferometer," Opt. Express **13**, 6296–6304 (2005).
[20]A. C. Kak and M. Slaney, *Principles of computerized tomographic imaging* (IEEE Press, 1988).
[21]F. Pfeiffer, O. Bunk, C. Kottler, and C. David, "Tomographic reconstruction of three-dimensional objects from hard X-ray differential phase contrast projection images," Nucl. Instr. Meth. Phys. Res. A **580**, 925–928 (2007).
[22]M. Engelhardt, J. Baumann, M. Schuster, C. Kottler, F. Pfeiffer, O. Bunk, and C. David, "High-resolution differential phase contrast imaging using a magnifying projection geometry with a microfocus x-ray source," Appl. Phys. Lett. **90**, 224101 (2007).
[23]L. Feldkamp, L. Davis, and J. Kress, "Practical cone-beam algorithm," J. Opt. Soc. Am. A **1**, 612–619 (1984).
[24]The Insight Segmentation and Registration Toolkit (ITK), available online at: http://www.itk.org (2016).
[25]P. Thalmann, C. Bikis, A. Hipp, B. Müller, S. E. Hieber, and G. Schulz, "Single and double grating-based x-ray microtomography using synchrotron radiation," Appl. Phys. Lett. **6**, 24022 (2017).
[26]B. Müller, F. Beckmann, M. Huser, F. Maspero, G. Székely, K. Ruffieux, P. Thurner, and E. Wintermantel, "Non-destructive three-dimensional evaluation of a polymer sponge by microtomography using synchrotron radiation," Biomol. Eng. **19**, 73–78 (2002).
[27]F. Pfeiffer, M. Bech, O. Bunk, P. Kraft, E. Eikenberry, C. Brönnimann, C. Grünzweig, and C. David, "Hard-x-ray dark-field imaging using a grating interferometer," Nat. Mater. **7**, 134–137 (2008).
[28]W. Yashiro, Y. Takeda, and A. Momose, "Efficiency of capturing a phase image using cone-beam x-ray Talbot interferometry," J. Opt. Soc. Am. A **25**, 2025–2039 (2008).
[29]M. Müller, A. Yaroshenko, A. Velroyen, M. Bech, A. Tapfer, B. Pauwels, P. Bruyndonckx, A. Sasov, and F. Pfeiffer, "Contrast-to-noise ratio optimization for a prototype phase-contrast computed tomography scanner," Rev. Sci. Instrum. **86**, 123705 (2015).
[30]S. McDonald, F. Marone, C. Hintermüller, G. Mikuljan, C. David, F. Pfeiffer, and M. Stampanoni, "Advanced phase-contrast imaging using a grating interferometer," J. Synch. Radiat. **16**, 562–572 (2009).
[31]M. Crema, F. Roemer, M. Marra, D. Burstein, G. Gold, F. Eckstein, T. Baum, T. Mosher, J. Carrino, and A. Guermazi, "Articular cartilage in the knee: Current MR imaging techniques and applications in clinical practice and research," Radiographics **31** (2011).
[32]G. Schulz, C. Götz, H. Deyhle, M. Müller-Gerbl, I. Zanette, M.-C. Zdora, A. Khimchenko, P. Thalmann, A. Rack, and B. Müller, "Hierarchical imaging of the human knee," Proc. SPIE **9967**, 99670R (2016).
[33]G. Schulz, T. Weitkamp, I. Zanette, F. Pfeiffer, F. Beckmann, C. David, S. Rutishauser, E. Reznikova, and B. Müller, "High-resolution tomographic imaging of a human cerebellum: comparison of absorption and grating-based phase contrast," J. R. Soc. Interface. **7**, 1665–1676 (2010).
[34]Z. Qi, J. Zambelli, N. Bevins, and G.-H. Chen, "Quantitative imaging of electron density and effective atomic number using phase contrast CT," Phys. Med. Biol. **55**, 2669–2677 (2010).
[35]A. Sarapata, M. Chabior, C. Cozzini, J. Sperl, D. Bequú, O. Langner, J. Coman, I. Zanette, M. Ruiz-Yaniz, and F. Pfeiffer, "Quantitative electron density characterization of soft tissue substitute plastic materials using grating-based x-ray phase-contrast imaging," Rev. Sci. Instrum. **85**, 103708 (2014).
[36]P. Thurner, F. Beckmann, and B. Müller, "An optimization procedure for spatial and density resolution in hard X-ray micro-computed tomography," Nucl. Instr. Meth. Phys. Res. B **225**, 599–603 (2004).

Chapter 4

Nanoanatomy of the selected brain tissues

Nanoanatomy: Three-dimensional imaging of human brain tissues beyond optical resolution

A. Khimchenko, C. Bikis, A. Pacureanu, S. E. Hieber, P. Thalmann, H. Deyhle, G. Schweighauser, J. Hench, M. Müller-Gerbl, G. Schulz, P. Cloetens, and B. Müller

(in preparation)

Nanoanatomy: Three-dimensional imaging of human brain tissues beyond optical resolution

Anna Khimchenko[1], Christos Bikis[1], Alexandra Pacureanu[2], Simone E. Hieber[1], Peter Thalmann[1], Hans Deyhle[1], Gabriel Schweighauser[3], Jürgen Hench[3], Stephan Frank[3], Magdalena Müller-Gerbl[4], Georg Schulz[1], Peter Cloetens[2], Bert Müller[1*]

[1]Biomaterials Science Center (BMC), Department of Biomedical Engineering, University of Basel, Allschwil, 4123, Switzerland.
[2]ID16A-NI Nano-Imaging Beamline, European Synchrotron Radiation Facility, Grenoble, 38043, France.
[3]Institute of Pathology, Department of Neuropathology, Basel University Hospital, Basel, 4056, Switzerland.
[4]Musculoskeletal Research Group, Department of Biomedicine, Basel University of Basel, Basel, 4056, Switzerland.

[*]To whom correspondence should be addressed; E-mail: bert.mueller@unibas.ch

Although conventional light microscopy allows for quantifying brain tissue morphology below a single-cell level, the lateral resolution of histological sections is limited to the wavelength of visible light, and the orthogonal resolution is usually restricted to the section's thickness ($\approx$ 1 µm). We introduce X-ray nano-holotomography with isotropic voxels down to 25 nm, in order to visualize three-dimensionally the anatomical micro- and nanostructures of the

human cerebellum and neocortex. These images exhibit a spatial resolution of at least 84 [59 117] nm. Therefore, these three-dimensional data resemble surface images obtained by electron microscopy, while avoiding the requirement of high-vacuum conditions and electron dense staining. Cellular and subcellular structures within Purkinje, granule, stellate, and pyramidal cells of formalin-fixed paraffin-embedded tissue blocks are resolved and segmented. Future hierarchical anatomy studies will rely on these relatively large volumes (0.43 mm^3) and can be reasonably extended to the entire human brain.

One-Sentence Summary

The article reports on the use of synchrotron radiation-based nano-holotomography for visualization of human brain tissue.

Introduction

The mammalian brain belongs to the most complex organs within the body, containing billions of neurons of hundreds of types with structures of interest at length scales down to the nanometer. This has sparked significant interest and efforts aimed at visualizing and understanding this tissue, given that its functions depend on hierarchically organized neuronal structures (*1*). Although brain tissue continues to be an attractive subject for investigations in neuroscience (*2, 3*), conventional imaging methodologies are limited in the three-dimensional (3D) representation at the nanometer scale.

To date, *in vivo* imaging of cells remains elusive, with the exception of STED microscopy (*4*). Nevertheless, a substantial effort has been devoted to revealing the 3D microstructure of brain tissue *ex vivo*, with or without the requirement of serial sectioning (*5–14*). Currently applied automated sectioning methods have overcome most of the drawbacks of a conventional

microtome and ultra-thin sections yield nearly isotropic voxels. Modern multi-focusing microscopy devices pushing orthogonal resolution below section thickness and digital image processing algorithms simplifying volume reconstruction. Nevertheless, up to date, 3D imaging of subcellular structures based on 2D histological sections in combination with microscopy is limited by sectioning-induced artefact and only possible if the cutting location was fortuitously selected. Moreover, the requirement of subcellular orthogonal resolution is mainly not satisfied (*15*). Recent protocols for rendering tissue transparency, for example CLARITY or PACT, in combination with advanced microscopy approaches enable up to whole-organ clearing (*16*). Nevertheless, serial sectioning or optical-ablative methods still suffer from acquisition times of days at single-cell resolution (*17*), significant computational effort and serious tissue consumption. On the same time, technically demanding tissue clearing (*18*) remains time consuming and has a reduced sample storage time. Subsequent to clearing, powerful histology can only partially be applied due to stain or antibody intensity reduction. In addition, intact preservation of tissue and cellular structures after clearing is questionable. Despite all above mentioned challenges, microscopy approaches successfully provided valuable insights into 3D cerebellar microstructure development (*19–21*).

X-ray imaging is known in 3D non-destructive imaging. For example, X-ray microscopy and ptychography studies allow the visualization of biological specimens (*22–27*), nevertheless, their usage is restricted by the effective field of view (FOV) and data acquisition rate.

X-ray phase-contrast imaging using synchrotron radiation with micrometer resolution is routinely performed at synchrotron radiation facilities (*28*). However, reaching the isotropic 100-nm barrier for soft tissues without applying a contrast agent remains a challenge. Going beyond optical resolution with 3D non-destructive imaging technique is an important milestone towards a bigger goal - full brain neuronal imaging with nanometer resolution. It is assumed that the further activities can foster the establishment of this emerging domain in the field of

anatomy. In this manner, nanoanatomy can become an integral part of nano-medicine.

Herein, we report on investigations into human brain nanoanatomy with synchrotron radiation-based hard X-ray nano-holotomography (XNH) at the ID16A-NI nano-imaging beamline (European Synchrotron Radiation Facility (ESRF), Grenoble, France) (*29*) with pixel sizes down to 25 nm. As a proof-of-principle experiment, we recorded nano-holotomography data for formalin-fixed paraffin-embedded (FFPE) human cerebellum and neocortex blocks, in which well-described cellular and subcellular structures of Purkinje, granule, stellate and pyramidal cells are recognized. Using a neocortex specimen imaged with an effective pixel size of 50 nm, we demonstrate the capabilities of our fully automated segmentation strategy for pyramidal cells. Segmentation of subcellular structures, including nuclear membranes and nucleoli, is also presented. To demonstrate the validity of this imaging modality, we compared conventionally hematoxylin and eosin (H&E)-stained histological sections with the related virtual sections reconstructed from XNH data. For the specific cases of the neocortex and the cerebellum, the clear determination of cellular and subcellular structures, including Purkinje and pyramidal cells as well as basket and stellate cells, is not only a technical achievement, but it also represents substantial progress in neuroscience research.

Compared to serial sectioning, tissue transformation by clearing, and ptychography, the approximately four-hour acquisition time is short. Taken together, after non-destructive modality tissue samples can not only readily be analyzed by sectional histology, offering characterization down to molecular level, but, in addition two-dimensional tinctorial data can be interpolated into three-dimensional space. Thus, limitations such as the type or numbers of stainings that could be applied to optically cleared tissue, no longer apply.

4

Results

Evaluation of XNH data

Overcoming limitations of optical microscopy, X-ray-based techniques can augment 3D visualization of human tissues, as long as the resulting contrast is reasonable. Limitations due to wavelength are not an issue, thus the application of X-ray optics extends spatial resolution far into the nanometer range, as we elucidate in this study.

The imaging benefits from a *prescan*, single distance fast tomography scan with relatively low magnification, albeit a wide FOV. Based on the prescan, the region of interest is selected and XNH data in local mode and at progressively increasing magnification levels is acquired. For instance, the prescan was based on radiographs with an effective pixel size of 200 nm and FOV of 0.4 mm $\times$ 0.4 mm (Fig. 1A). In one of samples, this region contains a pyramidal cell, which was imaged later with effective pixel sizes of 100 nm (Fig. 1B) and 50 nm (Fig. 1C). In total the data was collected with effective pixel sizes of 200 nm, 130 nm, 100 nm, 50 nm, and 25 nm, and related spatial and density resolutions for visualizing the neuronal architecture was determined. The contrast decrease in line with the effective pixel size was observed.

As illustrated in Figure 1, data recorded with a pixel length of 50 nm and binned by a factor of two (Fig. 1E) exhibiting a contrast-to-noise ratio (CNR) with respect to background (paraffin) of 0.806 [0.795 0.818], whereas the CNR of the data with 100 nm pixels corresponds to 0.734 [0.731 0.762]. The associated spatial resolutions are 92 [65 200] nm and 293 [235 391] nm, respectively, i.e., a significant improvement with respect to data with 100 nm voxels. Certainly, the effective FOV has decreased.

These quantitative metrics are directly related to the medical relevance of the acquired data. While the nuclear envelope (yellow rectangle) can be distinguished in the data acquired with both pixel sizes, namely 50 nm with binning factor of two and 100 nm, accurate estimation of

the envelope thickness is only possible based on the data with an effective pixel size of 50 nm. Based on the data acquired with an effective pixel size of 50 nm with binning factor of two it is possible to discriminate individual nuclear structures (blue circle) and assume presence of nuclear pores (green polygon) in nuclear envelope (yellow rectangle).

To demonstrate the resolution capabilities of XNH, we scanned human cerebellum with a pixel size down to 25 nm. Based on a scan with an effective pixel size of 130 nm (Fig. 2A), we selected a region of interest containing a Purkinje cell. Figure 2B represents tomography data recorded with an effective pixel size of 25 nm. Due to the low CNR of 0.260 [0.249 0.272] provided, the MTF was performed taking the median over ten slices resulting in upper estimation of the spatial resolution of 84 [59 117] nm. Despite the decrease in CNR, the increase in spatial resolution of the data acquired with an effective pixel size of 25 nm is noticeable. Only data acquired with an effective pixel size of 25 nm enables to clearly discriminate nuclear pores (green polygon) within nuclear envelope (yellow rectangle) of a Purkinje cell, and cell membranes (yellow rectangle) of stellate and granular cell, as well as their nuclear content (blue circle).

Even the use of 100 nm voxels yields more detailed anatomical data than light microscopy (Fig. 3). The tomography data for cerebellum and neocortex tissues allow for the direct observation of individual pyramidal (Fig. 3A), Purkinje and granular (Fig. 3B) cells. More importantly, cellular and subcellular features, including cell soma (orange ellipse), dendrite (purple star), nuclear envelope (yellow rectangle) enclosing nucleolus (red square) and some nuclear content (blue circle) can be detected.

The important benefit of XNH is the absolute compatibility with conventional histological analysis based on stained tissue sections. As it is demonstrated, the same specimen, see Figure 4, after tomographic imaging can be successfully stained with H&E without intensity reduction.

6

Tomography volume (Fig. 4A) has been converted into the RGB space (Fig. 4B) according to the 2D H&E-stained histological sections. For comparison, magnifications emphasize cellular structures, i.e., a granular (top) and a stellate cell (bottom). Considering the cerebellum, we demonstrate that histology and XNH complement each other: histology yields 2D functional information based on a variety of histochemical stains, while tomography reveals quantitative information over the entire tissue volume, with significantly increased spatial resolution. Multi-scale approaches that integrate multi-modal data are of the utmost interest when aiming to bridge scales effectively.

Owing to its cone-beam geometry and highly precision reflective optics, XNH can produce images significantly exceeding light microscopy, without applying contrast agents or staining, as required for electron microscopy (EM). Thus, there is a wide range of potential applications where XNH can be used before application of established imaging techniques, with the added potential of increased automation. For example, many pathological brain conditions are associated with cell loss (*30–35*) or abnormal cellular morphology (*36, 37*)

One more advantage of XNH is its ability to quantitatively record local refractive indices, delivering data as known from differential interference contrast microscopy, a widely used, labelling-free technique restricted to relatively thin ($\approx$ 25 µm), transparent specimens. This is potentially interesting, since the differentiation of Purkinje cells with comparable dimensions into *dark* and *light* ones, for example, based only on a difference in staining intensities, has been reported in human and animal studies (*38*). Nevertheless, the effect of fixation artifacts on data has to be characterized, hence, further studies have been suggested.

Segmenting cells and subcellular structures

The cellular organization of the human brain has been the focus of neuroscience research for more than a century, but complete neuronal network morphology is still missing (*39*). Despite

brain's size and complexity, one can realistically reveal the 3D localization of individual cells and identify nanostructures of interest from selected volumes.

Within the cerebellum, Purkinje cells form neuronal subpopulation with large somata and thus relatively easy to segment. In contrast, neocortical pyramidal cells, for example, are significantly smaller but occur in much higher densities. Consequently, intensity-based, region-growing segmentation approaches are unsuitable for automatically segmenting pyramidal neurons within the human neocortex. In the current study, even adaptive thresholding fails to segment individual pyramidal neurons, since the refractive index of the cells does not differ enough from the background values. Interactive learning and segmentation such as ilastik (*40*) have been applied successfully to segment components in EM images. This software, however, fails for cell segmentation in the present case.

For the XNH data the contrast was reasonable but not sufficient for simple segmentation approaches. As a consequence, we developed two-step framework for the fully automatic segmentation of pyramidal neurons within the cerebrum block. It rests upon a recently designed procedure (*28*) that is combined with sparse field method (SFM) of active contours (*41*) implemented with level sets (Fig. 5). Figure 5B displays the segmented pyramidal cells with characteristic features, including a large apical dendrite, a few short basal dendrites and the pyramid-shaped soma. Obviously, the morphology of pyramidal cells is generally homogeneous. Nevertheless, some diversity is present, particularly for the dendrites' diameter, which range from a few nanometers to several micrometers

In order to verify the automatic procedure, we performed semi-automatic segmentation using the Image Segmenter app® implemented in MATLAB R2016b (MathWorks, Natick, USA) in combination with an SFM. Here, individual pyramidal neurons were manually identified in a single slice by Image Segmenter. The SFM algorithm automatically extended these seeds up to the entire volume.

8

Using a neocortex specimen imaged with an effective pixel size of 50 nm with a binning factor of four (Fig. 5A), we demonstrate the capabilities of fully automated segmentation strategy for pyramidal cells with high accuracy (Fig. 5B). In this sense all pyramidal cells with cell body size within the specified range which were not touching the border of the sample were successfully segmented by both, automatic (Fig. 5C) and semi-automatic (Fig. 5D), approaches.

In order to identify subcellular structures, we used an intensity-based, region-growing segmentation framework implemented in the software package VGStudio MAX 2.0. Figure 5 displays a 3D rendering of subcellular structures within Purkinje cell recorded with a 100 nm pixel size. Region-growing segmentation allows for the exclusion of cell soma (green), nuclear membranes (blue), nuclear content (pink), and nucleolus (violet), whilst intensity thresholding helps discriminating between granular cells (red).

One can diagnose Purkinje cells as large, pear-shaped neurons with an average diameter of 30 µm, having both an axon and a dendrite. In the initial axonal and dendritic segments we observed tubular structures with electron density increased relative to the surroundings. The nuclear envelope probably contains nuclear pores. We also observed relatively big with respect to granular cells, rounded cells, potentially basket cells, located right above the Purkinje cell layer and giving off axonal ramifications in the direction of a neighboring Purkinje cell.

Conclusions

In conclusion, we have demonstrated the application of synchrotron radiation-based hard X-ray magnified phase-contrast nano-holotomography to resolve brain tissue nanoanatomy. The detection of individual subcellular structures with nm-resolution, without application of stains, sets a new standard in non-destructive three-dimensional imaging. Thus, biomedical questions which are currently addressed by optical or electron microscopy can be studied beforehand by XNH in a complementary manner. This non-destructive approach adds increased automation

and facilitates interpretation of cellular ultrastructure including its alterations caused by pathological conditions or medical interventions. Therefore we believe that synchrotron radiation-based hard X-ray magnified phase-contrast nano-holotomography is likely to influence future studies on developmental and functional biology and anatomy.

Acknowledgements

The authors acknowledge the financial support of the Swiss National Science Foundation (SNSF) projects 147172, 150164 and 147172. The authors thank B. Osmani, University of Basel, for his help with the special preparation required for vacuum conditions and many useful discussions. The authors also acknowledge the staff of the European Synchrotron Radiation Facility (ESRF), Grenoble, France, for their support during data acquisition and reconstruction. The project was supported by the ESRF (proposal MD-969).

References and Notes

1. L. Hogstrom, S. Guo, K. Murugadoss, M. Bathe, *Interface Focus* **6** (2016).

2. C. Petersen, *Neuron* **56**, 339 (2007).

3. P. Mombaerts, *et al.*, *Cell* **87**, 675 (1996).

4. S. Berning, K. Willig, H. Steffens, P. Dibaj, S. Hell, *Science* **335**, 551 (2012).

5. K. Amunts, *et al.*, *Science* **340**, 1472 (2013).

6. A. Li, *et al.*, *Science* **330**, 1404 (2010).

7. S. W. Oh, *et al.*, *Nature* **508**, 207 (2014).

8. T. Ragan, *et al.*, *Nat. Methods* **9**, 255 (2012).

9. K. Ichimura, *et al.*, *Sci. Rep.* **5**, 8993 (2015).

10. S. Mikula, J. Binding, W. Denk, *Nat. Methods* **9**, 1198 (2012).

11. K. Micheva, S. Smith, *Neuron* **55**, 25 (2007).

12. K. Chung, *et al.*, *Nature* **497**, 332 (2013).

13. E. Murray, *et al.*, *Cell* **163**, 1500 (2015).

14. H.-U. Dodt, *et al.*, *Nat. Methods* **4**, 331 (2007).

15. A. Khimchenko, *et al.*, *NeuroImage* **139**, 26 (2016).

16. P. H. Neckel, U. Mattheus, B. Hirt, L. Just, A. F. Mack, *Sci. Rep.* **6**, 34331 (2016).

17. K. Chung, K. Deisseroth, *Nat. Methods.* **10**, 508 (2013).

18. D. S. Richardson, J. W. Lichtman, *Cell* **162**, 246 (2015).

19. M. Bénard, A. Lebon, H. Komuro, D. Vaudry, L. Galas, *JoVE* **e52810**, 8 (2015).

20. L. Silvestri, *et al.*, *JoVE* **80** (2013).

21. H. Wang, J. Zhu, T. Akkin, *NeuroImage* **84**, 1007 (2014).

22. G.-C. Yin, *et al.*, *Appl. Phys. Lett.* **88**, 241115 (2006).

23. D. Y. Parkinson, G. McDermott, M. Le Gros, C. A. Larabell, *Microsc. Microanal.* **14**, 666 (2008).

24. W. S. Haddad, *et al.*, *Science* **266**, 1213 (1994).

25. Y. S. Chu, *et al.*, *Appl. Phys. Lett.* **92** (2008).

26. J. Andrews, F. Meirer, Y. Liu, Z. Mester, P. Pianetta, *Microsc. Res. Tech.* **74**, 671 (2011).

27. M. Dierolf, *et al.*, *Nature* **467**, 436 (2010).

28. S. E. Hieber, *et al.*, *Sci. Rep.* **6**, 32156 (2016).

29. J. C. da Silva, *et al.*, *Optica* **4**, 492 (2017).

30. N. Quillinan, *et al.*, *Neuroscience* **284**, 555 (2015).

31. S. Lomoio, D. Necchi, V. Mares, E. Scherini, *Epilepsy Res.* **93**, 17 (2011).

32. R. Louis, *et al.*, *Parkinsonism Relat. Disord.* **20**, 1270 (2014).

33. H. Miyahara, T. Itonaga, T. Maeda, T. Izumi, K. Ihara, *Neuropathology* **35**, 266 (2015).

34. A. MacKenzie-Graham, *et al.*, *NeuroImage* **48**, 637 (2009).

35. M. Schubert, D. Panja, M. Haugen, C. Bramham, C. Vedeler, *Acta Neuropathol.* **128**, 835 (2014).

36. R. Raike, E. Hess, H. Jinnah, *Brain Res.* **1611**, 56 (2015).

37. R. Idol, *et al.*, *PLoS ONE* **9** (2014).

38. O. Castejòn, *Biocell* **36**, 1 (2012).

39. H. Mohan, *et al.*, *Cereb. Cortex* **25**, 4839 (2015).

40. C. Sommer, C. Straehle, U. Kothe, F. Hamprecht, *Proc. ISBI* **5872394**, 230 (2011).

41. Sparse Field Methods for Active Contours, *available online at: https://ch.mathworks.com/matlabcentral/fileexchange/23847-sparse-field-methods-for-active-contours?focused=6125428stab=function* (2017).

12

42. P. Bleuet, *et al.*, *Rev. Sci. Instrum.* **80**, 056101 (2009).

43. P. Cloetens, *et al.*, *Appl. Phys. Lett.* **75**, 2912 (1999).

44. A. Mirone, E. Brun, E. Gouillart, P. Tafforeau, J. Kieffer, *Nucl. Instrum. Methods Phys. Res. B* **324**, 41 (2014).

45. The Insight Segmentation and Registration Toolkit (ITK), *available online at: http://www.itk.org* (2016).

46. B. Müller, *et al.*, *Biomol. Eng.* **19**, 73 (2002).

47. P. Thalmann, *et al.*, *Appl. Phys. Lett.* **6**, 24022 (2017).

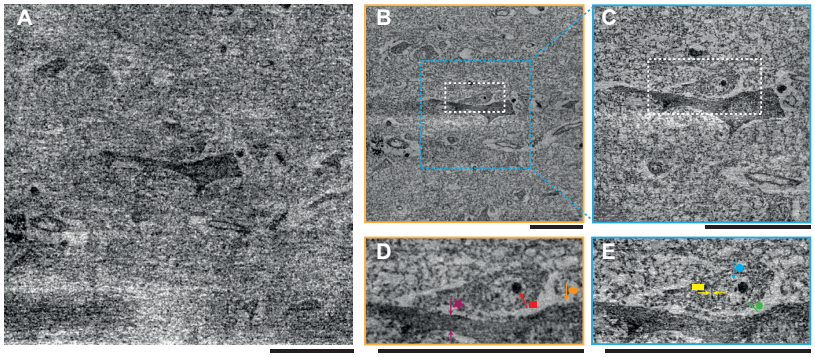

Fig. 1. Comparing data for a neocortex cylinder measured with 200 nm (prescan), 100 nm and 50 nm pixel sizes.
Based on prescan (A) with a field of view of 0.4 mm × 0.4 mm, the part with a selected pyramidal cell was measured with effective pixel sizes of 100 nm (B) and 50 nm (C). Comparing data measured with an effective pixel size of 100 nm (D) and 50 nm binned twice (E), one can appreciate that 50 nm data provide increased density and spatial resolutions, albeit the effective field of view decreases. The data enables discrimination of cellular and subcellular structures: cell soma (orange ellipse), dendrite (purple star), nuclear envelope (yellow rectangle) with nuclear pores (green polygon) enclosing nucleolus (red square) and some nuclear content (blue circle). Scale bars correspond to 50 µm.

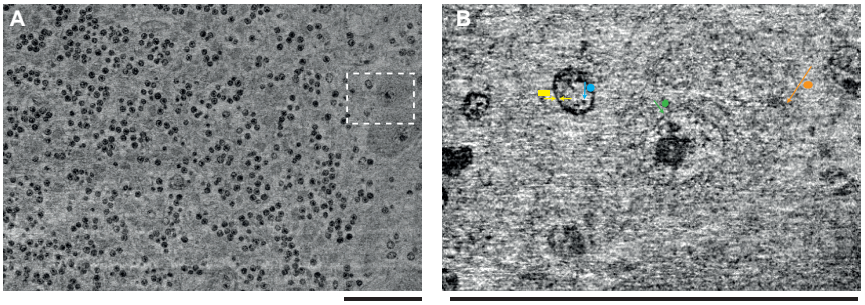

Fig. 2. Reaching the isotropic 100 nm resolution barrier for soft tissues, without applying contrast agent to a cerebellum block example.
Based on the scan with an effective pixel size of 130 nm (A), a region of interest containing a Purkinje cell was identified and scanned with an effective pixel size of 25 nm (B). While the 25 nm data provide significantly improved spatial resolution allowing to distinguish nuclear pores (green polygon) within nuclear envelope (yellow rectangle) of Purkinje cell, and cell membranes (yellow rectangle) of stellate and granular cell, as well as their nuclear content (blue circle), the noise level increases, making it hard to discriminate the cell soma (orange ellipse). The scale bars correspond to 50 µm.

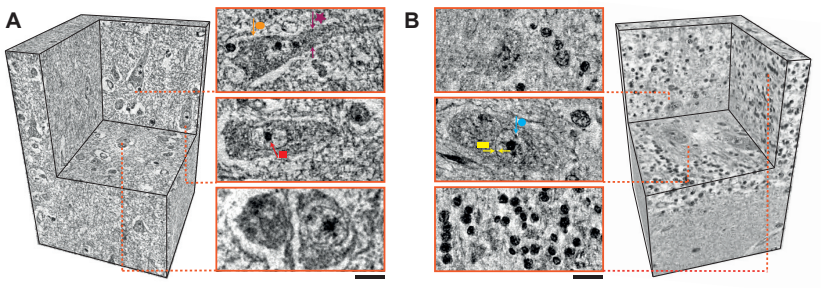

Fig. 3. 3D volume rendering of cerebellum and neocortex specimens, highlighting electron microscopy-like data quality acquired without extensive tissue preparation.
Visualization of neocortex (A) and cerebellum (B) blocks measured with an effective pixel size of 100 nm. Magnifications of selected cutting planes illustrate cellular and subcellular features, including cell soma (orange ellipse), dendrite (purple star), nuclear envelope (yellow rectangle) enclosing nucleolus (red square) and some nuclear content (blue circle). The scale bars correspond to 10 µm.

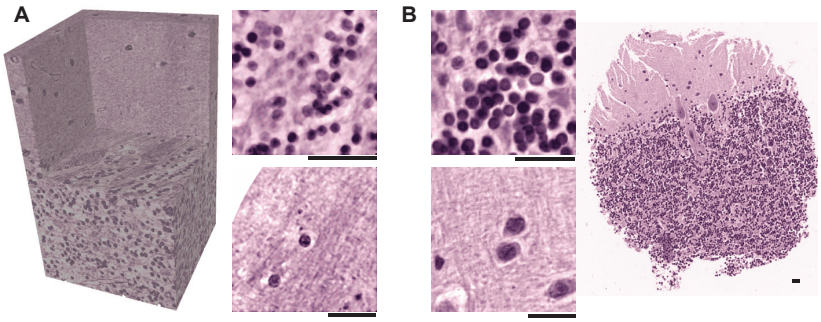

Fig. 4. Virtual histology by colorized µCT, illustrating the potential of XNH to extrapolate histological results over the complete tissue volume with the added value of increased resolution.
Tomography volume (A) converted into RGB color space to resemble the H&E-stained histological section (B). Scale bars correspond to 20 µm.

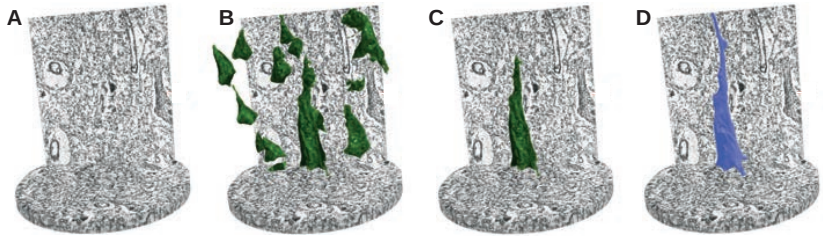

Fig. 5. Segmentation of individual pyramidal cells.
Automatic segmentation of pyramidal cells within a neocortex block (A) with a diameter $d = 0.1$ mm measured with an effective pixel size of 50 nm. For verification of the automatic segmentation (B, C), semi-automatic segmentation based on manually initialised elastic modelling was performed (D).

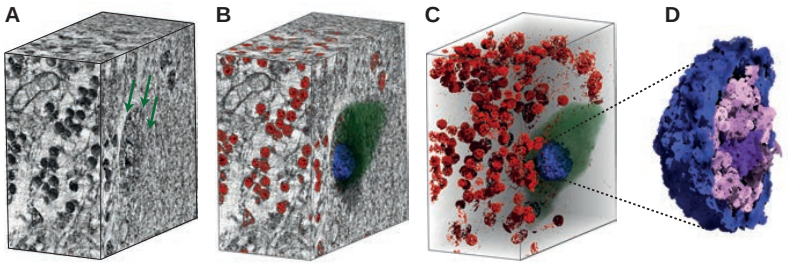

Fig. 6. 3D rendering of subcellular structures within a Purkinje cell measured with an effective pixel size of 100 nm.
Region-growing segmentation allows for the exclusion of cell soma (green), nuclear membrane (blue), nuclear content (pink) and nucleolus (violet). Intensity thresholding (red) enables the discrimination of granule cells.

Supplementary Materials for Nanoanatomy: Three-dimensional imaging of human brain tissues beyond optical resolution

Anna Khimchenko[1], Christos Bikis[1], Alexandra Pacureanu[2], Simone E. Hieber[1], Peter Thalmann[1], Hans Deyhle[1], Gabriel Schweighauser[3], Jürgen Hench[3], Stephan Frank[3], Magdalena Müller-Gerbl[4], Georg Schulz[1], Peter Cloetens[2], Bert Müller[1*]

[1]Biomaterials Science Center (BMC), Department of Biomedical Engineering, University of Basel, Allschwil, 4123, Switzerland.
[2]ID16A-NI Nano-Imaging Beamline, European Synchrotron Radiation Facility, Grenoble, 38043, France.
[3]Institute of Pathology, Department of Neuropathology, Basel University Hospital, Basel, 4056, Switzerland.
[4]Musculoskeletal Research Group, Department of Biomedicine, Basel University of Basel, Basel, 4056, Switzerland.

*To whom correspondence should be addressed; E-mail: bert.mueller@unibas.ch

Materials and methods

Specimen preparation

Post mortem specimens were collected from donated to the Institute of Anatomy, University of Basel and Basel University Hospital, Switzerland brains. All donors of the programs contributed their bodies to education and research purposes. Informed consent for scientific use was

obtained and all procedures were conducted in accordance with the Declaration of Helsinki. The brains were fixed in 4 % histological-grade buffered formalin, before samples of the neocortex, adjacent white matter and cerebellum were excised, dehydrated in ethanol, cleared in xylenes and embedded in a paraffin/plastic polymer mixture (Surgipath Paraplast, Leica Biosystems, Switzerland). Cylindrical specimens with a diameter of ≈500 µm and a height of ≈1 mm were cut from paraffin blocks using a metal punch.

Nano-holotomography

Phase-contrast nano-holomomography images were acquired at the ID16A-NI nano-imaging beamline of the European Synchrotron Radiation Facility (ESRF) in Grenoble, France (*29*). The high brilliance beam can be focused to a spot at least 13 nm in size. For the imaging experiments an X-ray beam with a photon energy of 17.05 keV corresponding to the first harmonic of a single-line undulator (19 mm period U19) was focused onto a spot of approximately 25 nm × 30 nm via a pair of multilayer-coated Kirkpatrick-Baez (KB) mirrors for horizontal and vertical focusing. The photon flux was of the order of 10^{11} photons per second. The sample was mounted on a rotation stage downstream from the focal plane inside a vacuum chamber. The pressure in the vacuum chamber is in the range 10^{-7} - 10^{-8} mbar. Nevertheless, should not be generalized that vacuum condition is the essential pre-request for XNH data acquisition. The measurements can be performed in air under the atmospheric pressure. The main point behind the vacuum environment is protection of KB optics and increased stability, hence the ultimate resolution can be reached.

The detector, composed of a scintillator converting X-rays to visible light, magnifying optics and a CCD camera (FReLoN, ESRF, Grenoble, France) with 4096 × 4096 pixels, was placed approximately 1.2 m away from the focal plane. Four tomographic scans were recorded by placing the sample at preselected distances between the focus and the detector. The divergent

beam yielded a geometrical magnification $M = (D_1 + D_2)/D_1$, where D_1 denotes the distance between focal plane and sample, and D_2 denotes the distance between sample and detector. For each rotation angle, the four recorded radiographs were processed to obtain phase maps that were subsequently used for tomographic reconstruction.

As the samples were larger (≈500 µm) than the field of view (FOV), local holotomography measurements were performed after selecting the relevant region of interest on a single-distance low-resolution tomography scan – a prescan with an effective pixel size of 200 nm. A complete set of holograms was composed of four times 2000 angular projections. The summary of experimental parameters is listed in Table S1.

Table S1:
Scanning parameters. All scans were performed at a mean photon energy of 17 keV. *l*: effective pixel size; *N*: number of projections; *d*: number of propagation distances; *t*: exposure time; *D*: the focus to sample distances.

Sample N	**Tissue**	***l*** [nm]	***N***	***d***	***t*** [s]	***D*** [mm]
1.1	Cerebellum	200	1200	1	0.25	{80.533 }
1.2	Cerebellum	130	1200	4	0.25	{52.346 54.592 63.575 82.226}
1.3	Cerebellum	50	1200	4	0.25	{20.133 20.997 24.452 31.625}
1.4	Cerebellum	25	1800	4	0.25	{10.066 10.499 12.226 15.812}
2.1	Cortex	200	1200	1	0.3	{80.533}
2.2	Cortex	100	2000	4	0.3	{40.266 41.994 48.904 63.251}
2.3	Cortex	50	2000	4	0.3	{20.133 20.997 24.452 31.625}
3.1	Cerebellum	200	1200	1	0.3	{80.533 }
3.2	Cerebellum	100	1900	4	0.3	{40.266 41.994 48.904 63.251}
3.3	Cerebellum	50	1900	4	0.3	{20.133 20.997 24.452 31.625}

In order to retrieve the phase maps (*42, 43*), a set of four radiographs at a given rotation angle was normalized with respect to the incoming beam, then brought to the same magnification, aligned and used in an adapted contrast transfer function (CTF) algorithm to determine the phase shift. Tomographic reconstruction was obtained by filtered back projections using PyHST2 (*44*). The reconstructed images provided the 3D distribution of the real part of the complex refractive

index, which is proportional to local electron density ρ_e.

Histology

Subsequent to tomography, samples were re-embedded in a standard histology paraffin block and sectioned at a thickness of 4 µm for histological examination. Sections were mounted on glass slides and stained with hematoxylin and eosin (H&E). The resulting slides were digitized using a microscope slide scanner (Pannoramic midi, 3DHISTECH, Sysmex Suisse AG) with an effective pixel size of 240 nm.

3D-3D registration

For comparison of the datasets measured of different pixel size, translation registration was performed, using the library by ITK (*45*), allowing to select the same region of interest for the analysis.

Quantitative metrics

The quantitative evaluation of XNH data was based on the calculation of a volumetric contrast-to-noise ratio (CNR) and an edge-based upper limit of spatial resolution. CNR was defined as: $CNR = |I_1 - I_2|/\sqrt{\sigma_1^2 + \sigma_2^2}$, where I_1 and I_2 indicate the mean intensities of homogeneous components within the specimen, and σ_1 and σ_2 are corresponding to the standard deviations. The grey values in the 3D intensity histogram were fitted with two Gaussians (*46*) to extract I and σ.

To estimate the upper limit of spatial resolution we used the intersection of the normalized modulation transfer function (nMTF) with a 10 % value (*47*). For the calculation, we chose a region at the nucleus-nuclear-plasma interface. In order to perform an accurate comparison of the data measured with the selected effective pixel sizes, 50 nm pixel size data was binned with a factor of two. Due to the low CNR provided by the data acquired with 25 nm pixel size,

the nMTF was performed taking the median over ten slices resulting in upper estimation of the spatial resolution.

Data segmentation

For the automatic segmentation of pyramidal neurons within the neocortex block, we used a two-step framework. We applied an approach that had already been successfully applied to a large number of Purkinje cells in the human cerebellum (*28*) in combination with sparse field methods (SFM) of active contours (*41*) using level set. The first step was based on feature-based Frangi-filtering that detects structures of interest by analysing the eigenvalues of the 3D Hessian matrix. The parameters were chosen as α = 0.5, β = 0.1, γ = 60, which accounted well for high intensity changes on the margins of the cells but neglected strong noise in the background, due to the high value for parameter γ. The filter parameters also included the radius range of 15 to 25 voxels with a step size of r = 2. The filter result was binarized using a threshold of 0.01. Objects were neglected if they were smaller than 20,000 voxels or only partially segmented on the margin.

The segmentation results for the Frangi filter were used as an initialization mask for the SFM. Segmentation started with images partitioning in slice-wise manner with N_{it} = 900 iterations and the relative weighting of curve smoothness of ξ = 0.01, followed by a 3D step with N_{it} = 60 and ξ = 1, where the output of the 2D steps was used as an initialization mask. All parameters were selected based on visual inspection, to avoid noise segmentation. Objects smaller than 300 voxels were neglected.

In order to verify the results of an automatic approach, semi-automatic segmentation was performed, whereby each pyramidal cell was individually initialized in one selected slice by means of an Image Segmenter app® implemented in MATLAB R2016b (MathWorks, Natick, USA). This segmentation was used to initialize 2D SFM segmentation in an iterative manner.

The subsequent steps were equivalent to the automatic approach.

Subcellular structures were semi-automatically segmented using an intensity-based, region-growing segmentation framework with multiple seed points implemented in the commercially available software package VGStudio MAX 2.0 (Volume Graphics, Heidelberg, Germany).

6

Chapter 5

Conclusions and Outlook

Due to marginal differences in attenuation and deflection within human brain tissues, visualising them is an ambitious challenge in hard X-ray imaging. It was demonstrated that formalin-fixed paraffin-embedded human cerebellum yields appropriate absorption contrast in laboratory-based µCT data, comparable to conventional histological sections. The high sensitivity of tomography even allows for visualising individual non-stained Purkinje cells within the human cerebellum. The µCT of FFPE samples can be understood as a time-efficient and reliable tissue visualisation methodology, and so it could become a method of choice for imaging of relatively large specimens within the laboratory environment.

Synchrotron radiation-based phase-contrast tomography offers superior 3D images of the human cerebellum, in comparison to laboratory-based absorption-contrast µCT. Nonetheless, it was shown that laboratory µCT can provide data which are almost identical to synchrotron radiation-based phase-contrast tomography. Obviously, synchrotron radiation-based imaging can reach the sub-cellular level, but beamline access is usually restricted. It can be concluded that the laboratory methodology provides a valuable compromise between spatial resolution, density contrast and penetration depth, and therefore it has the potential to fill the current performance gap between synchrotron radiation-based µCT and histology for a variety of tissue biopsies in many post-mortem applications. While histology still yields superior two-dimensional image quality, µCT provides a valuable 3D compliment.

As demonstrated, already with a pixel size of 3.5 µm laboratory-based absorption-contrast µCT can resolve individual brain cells. With the pixel size of 2.2 µm beginning of the dendrite tree can be distinguished. It would be interesting to conduct an additional study on resolution capabilities of laboratory-based absorption-contrast µCT of formalin-fixed paraffin-embedded tissues. For example, a further decrease in pixel size could enable the quantification of the three-dimensional neuronal dendrite structure and organisation. Such data can be particularity important, as many brain pathologies show abnormalities in cellular morphology, such as axonal swellings or increased numbers of branched axons. In addition, the question arises as to whether laboratory-based absorption-contrast µCT can resolve sub-cellular structures.

During the current study, it was demonstrated that pseudo-colouring of tomography data according to the H&E stain can be performed, virtually extending two-dimensional histology into the third dimension. H&E staining, while being the most often used, is not the most powerful. In general, histological examination enables the application of a variety of biochemical tests to the tissue, such as histochemical stains or antibodies. It would be interesting to conduct an additional study to investigate the correlation between different staining protocols and tomography data. If the results came out as expected, this would prove that the results of the thesis are not only valid for H&E stain, but also for a broad range of staining protocols.

As phase-contrast imaging provides improved data quality in comparison to absorption-contrast imaging, the X-ray double-grating interferometer was designed and installed into the advanced conventional µCT system nanotom® m during this work. The set-up´s successful performance was demonstrated in projection and tomographic imaging. These results suggest that the extension of a commercially available absorption-contrast µCT system via grating interferometry offers the potential to fill the current performance gap between LBµCT and phase-contrast µCT using synchrotron radiation in the visualising soft tissues.

In general, this thesis emphasises the need for further grating set-up optimisation, especially in order to reach the cellular resolution. The question arises as to whether laboratory-based phase-contrast data could possible provide results comparable to synchrotron radiation-based phase-contrast data.

Grating interferometry is a multi-modal imaging technique providing absorption, phase and dark-field (scattering) signals simultaneously. In further studies, it would be interesting to investigate the complementarity of the signals in the laboratory set-up, particularly the added value of dark-field images. The thesis emphasises the need for further characterisation of the set-up. While visibility and source size modes were described in the current work, interesting questions on the determination of the set-up design, i.e. different grating distances and periods, asymmetric design or adaptation of gratings to the curvature of the beam, still need to find answers.

In the framework of the current thesis, the application of synchrotron radiation-based hard X-ray magnified phase-contrast nano-holotomography for visualising brain tissues was demonstrated. It was shown that the modality can reveal the 3D nanostructure of human brain tissues, without the use of specific labels. The study shows that automatic cell feature quantification of human tissues is feasible, based on synchrotron radiation-based nano-holotomography. For a long time, visualising the finer morphological details of cells could only be achieved by electron microscopy [76], but the imaging data aquired herein are comparable to these produced by electron microscopy. In the framework of the thesis, the nano-holotomography data of brain tissues with a spatial resolution of at least 84 nm were successfully acquired; however, further experiments with medically relevant specimens are foreseen. While the term *micro-anatomy* has been used for decades, the term *nanoanatomy* is rather new. It is assumed that nanoanatomy could become an integral part of clinical nano-medicine.

In conclusion, this work provides further advances in the X-ray imaging of brain tissues and holds potential for visualising features producing low absorption contrast.

Bibliography

[1] M. R. Stefanescu, M. Dohnalek, S. Maderwald, M. Thürling, M. Minnerop, A. Beck, M. Schlamann, J. Diedrichsen, M. E. Ladd, and D. Timmann. Structural and functional MRI abnormalities of cerebellar cortex and nuclei in SCA3, SCA6 and Friedreich's ataxia. *Brain*, 138(5):1182–1197, 2015.

[2] N. Law, M. Greenberg, E. Bouffet, S. Laughlin, M. D. Taylor, D. Malkin, F. Liu, I. Moxon-Emre, N. Scantlebury, J. Skocic, and D. Mabbott. Visualization and segmentation of reciprocal cerebrocerebellar pathways in the healthy and injured brain. *Hum. Brain Mapp.*, 36(7):2615–2628, 2015.

[3] J. Kim, J. Shin, J.-H. Oh, H. Jung, Y.-B. Kim, Z.-H. Cho, and J. W. Chang. Longitudinal FDG microPET imaging of neuropathic pain: does cerebellar activity correlate with neuropathic pain development in a rat model? *Acta Neurochir.*, 157(6):1051–1057, 2015.

[4] A. S. Choe, Y. Gao, X. Li, K. B. Compton, I. Stepniewska, and A. W. Anderson. Accuracy of image registration between MRI and light microscopy in the ex vivo brain. *J. Magn. Reson. Imaging*, 29(5):683–692, 2011.

[5] P. S. Tsai, B. Friedman, A. I. Ifarraguerri, B. D. Thompson, V. Lev-Ram, C. B. Schaffer, Q. Xiong, R. Y. Tsien, J. A. Squier, and D. Kleinfeld. All-optical histology using ultrashort laser pulses. *Neuron*, 39(1):27–41, 2003.

[6] K. Amunts, C. Lepage, L. Borgeat, H. Mohlberg, T. Dickscheid, M.-É. Rousseau, S. Bludau, P.-L. Bazin, L. B. Lewis, A.-M. Oros-Peusquens, N. J. Shah, T. Lippert, K. Zilles, and A. C. Evans. BigBrain: An ultrahigh-resolution 3D human brain model. *Science*, 340(6139):1472–1475, 2013.

[7] K. Amunts, O. Bücker, and M. Axer. Towards a multiscale, high-resolution model of the human brain. *LNCS*, 8603:3–14, 2014.

[8] A. Li, H. Gong, B. Zhang, Q. Wang, C. Yan, J. Wu, Q. Liu, S. Zeng, and Q. Luo. Micro-optical sectioning tomography to obtain a high-resolution atlas of the mouse brain. *Science*, 330(6009):1404–1408, 2010.

[9] S. W. Oh, J. A. Harris, L. Ng, B. Winslow, N. Cain, S. Mihalas, Q. Wang, C. Lau, L. Kuan, A. M. Henry, M. T. Mortrud, B. Ouellette, T. N. Nguyen, S. A. Sorensen, C. R. Slaughterbeck, W. Wakeman, Y. Li, D. Feng, A. Ho, E. Nicholas, K. E. Hirokawa, P. Bohn, K. M. Joines, H. Peng, M. J. Hawrylycz, J. W. Phillips, J. G. Hohmann, P. Wohnoutka, C. R. Gerfen, C. Koch, A. Bernard, C. Dang, A. R. Jones, and H. Zeng. A mesoscale connectome of the mouse brain. *Nature*, 508(7495):207–214, 2014.

[10] T. Ragan, L. R. Kadiri, K. U. Venkataraju, K. Bahlmann, J. Sutin, J. Taranda, I. Arganda-Carreras, Y. Kim, H. S. Seung, and P. Osten. Serial two-photon tomography for automated ex vivo mouse brain imaging. *Nat. Methods*, 9(3):255–258, 2012.

[11] K. Ichimura, N. Miyazaki, S. Sadayama, K. Murata, M. Koike, K.-I. Nakamura, K. Ohta, and T. Sakai. Three-dimensional architecture of podocytes revealed by block-face scanning electron microscopy. *Sci. Rep.*, 5(8993), 2015.

[12] S. Mikula, J. Binding, and W. Denk. Staining and embedding the whole mouse brain for electron microscopy. *Nat. Methods*, 9(12):1198–1201, 2012.

[13] J. B. Pawley, editor. *Handbook of biological confocal microscopy*. Springer, New York, 3 edition, 2006.

[14] K. D. Micheva and S. J. Smith. Array tomography: A new tool for imaging the molecular architecture and ultrastructure of neural circuits. *Neuron*, 55(1):25–36, 2007.

[15] K. Chung, J. Wallace, S.-Y. Kim, S. Kalyanasundaram, A. S. Andalman, T. J. Davidson, J. J. Mirzabekov, K. A. Zalocusky, J. Mattis, A. K. Denisin, S. Pak, H. Bernstein, C. Ramakrishnan, L. Grosenick, V. Gradinaru, and K. Deisseroth. Structural and molecular interrogation of intact biological systems. *Nature*, 497(7449):332–337, 2013.

[16] E. Murray, J. H. Cho, D. Goodwin, T. Ku, J. Swaney, S.-Y. Kim, H. Choi, Y.-G. Park, J.-Y. Park, A. Hubbert, M. McCue, S. Vassallo, N. Bakh, M. P. Frosch, V. J. Wedeen, H. S. Seung, and K. Chung. Simple, scalable proteomic imaging for high-dimensional profiling of intact systems. *Cell*, 163(6):1500–1514, 2015.

[17] H.-U. Dodt, U. Leischner, A. Schierloh, N. Jährling, C. P. Mauch, K. Deininger, J. M. Deussing, M. Eder, W. Zieglgänsberger, and K. Becker. Ultramicroscopy: Three-dimensional visualization of neuronal networks in the whole mouse brain. *Nat. Methods*, 4(4):331–336, 2007.

[18] D. S. Richardson and J. W. Lichtman. Clarifying tissue clearing. *Cell*, 162(2):246–257, 2015.

[19] G.-C. Yin, M.-T. Tang, Y.-F. Song, F.-R. Chen, K. S. Liang, F. W. Duewer, W. Yun, C.-H. Ko, and H.-P. D. Shieh. Energy-tunable transmission x-ray microscope for differential contrast imaging with near 60 nm resolution tomography. *Appl. Phys. Lett.*, 88(24):241115, 2006.

[20] D. Y. Parkinson, G. McDermott, M. Le Gros, and C. A. Larabell. Quantitative 3-D imaging of eukaryotic cells using soft x-ray tomography. *Microsc. Microanal.*, 14(SUPPL. 2):666–667, 2008.

[21] W. S. Haddad, I. McNulty, J. E. Trebes, E. H. Anderson, R. A. Levesque, and L. Yang. Ultrahigh-resolution x-ray tomography. *Science*, 266(5188):1213–1215, 1994.

[22] Y. S. Chu, J. M. Yi, F. De Carlo, Q. Shen, W.-K. Lee, H. J. Wu, C. L. Wang, J. Y. Wang, C. J. Liu, C. H. Wang, S. R. Wu, C. C. Chien, Y. Hwu, A. Tkachuk, W. Yun, M. Feser, K. S. Liang, C. S. Yang, J. H. Je, and G. Margaritondo. Hard-x-ray microscopy with fresnel zone plates reaches 40 nm Rayleigh resolution. *Appl. Phys. Lett.*, 92(10), 2008.

[23] J. C. Andrews, F. Meirer, Y. Liu, Z. Mester, and P. Pianetta. Transmission X-ray microscopy for full-field nano imaging of biomaterials. *Microsc. Res. Tech.*, 74(7):671–681, 2011.

[24] M. Dierolf, A. Menzel, P. Thibault, P. Schneider, C. M. Kewish, R. Wepf, O. Bunk, and F. Pfeiffer. Ptychographic X-ray computed tomography at the nanoscale. *Nature*, 467(7314):436–439, 2010.

[25] D. Paganin. *Coherent X-ray optics (Oxford Series on Synchrotron Radiation)*. Oxford University Press, 1 edition, 2006.

[26] A. Momose. Recent advances in X-ray phase imaging. *Jpn. J. Appl. Phys.*, 44(9A):6355–6367, 2005.

[27] A. Momose. Phase-sensitive imaging and phase tomography using X-ray interferometers. *Opt. Express*, 11(19):2303–2314, 2003.

[28] I. Zanette, S. Lang, A. Rack, M. Dominietto, M. Langer, F. Pfeiffer, T. Weitkamp, and B. Müller. Holotomography versus X-ray grating interferometry: A comparative study. *Appl. Phys. Lett.*, 103(24), 2013.

[29] A. Momose, T. Takeda, Y. Itai, and K. Hirako. Phase-contrast x-ray computed tomography for observing biological soft tissues. *Nat. Med.*, 2(4):473–475, 1996.

[30] R. Fitzgerald. Phase-sensitive X-ray imaging. *Phys. Today*, 53(7):23–26, 2000.

[31] Y. Liu, J. Nelson, C. Holzner, J. C. Andrews, and P. Pianetta. Recent advances in synchrotron-based hard x-ray phase contrast imaging. *J. Phys. D*, 46(49):494001, 2013.

[32] U. Bonse and M. Hart. An x-ray interferometer. *Appl. Phys. Lett.*, 6(8):155–156, 1965.

[33] A. Snigirev, I. Snigireva, V. Kohn, S. Kuznetsov, and I. Schelokov. On the possibilities of x-ray phase contrast microimaging by coherent high-energy synchrotron radiation. *Rev. Sci. Instrum.*, 66(12):5486–5492, 1995.

[34] C. David, B. Nöhammer, H. H. Solak, and E. Ziegler. Differential x-ray phase contrast imaging using a shearing interferometer. *Appl. Phys. Lett.*, 81(17):3287–3289, 2002.

[35] T. Weitkamp, A. Diaz, C. David, F. Pfeiffer, M. Stampanoni, P. Cloetens, and E. Ziegler. X-ray phase imaging with a grating interferometer. *Opt. Express*, 13(16):6296–6304, 2005.

[36] A. Momose, W. Yashiro, Y. Takeda, Y. Suzuki, and T. Hattori. Phase tomography by X-ray Talbot interferometry for biological imaging. *Jpn. J. Appl. Phys.*, 45(6A):5254–5262, 2006.

[37] A. Momose, S. Kawamoto, I. Koyama, Y. Hamaishi, K. Takai, and Y. Suzuki. Demonstration of x-ray Talbot interferometry. *Jpn. J. Appl. Phys.*, 42(7B):L866–L868, 2003.

[38] F. Pfeiffer, O. Bunk, C. David, M. Bech, G. Le Duc, A. Bravin, and P. Cloetens. High-resolution brain tumor visualization using three-dimensional x-ray phase contrast tomography. *Phys. Med. Biol.*, 52(23):6923–6930, 2007.

[39] F. A. Dilmanian, Z. Zhong, B. Ren, X. Y. Wu, L. D. Chapman, I. Orion, and W. C. Thomlinson. Computed tomography of x-ray index of refraction using the diffraction enhanced imaging method. *Phys. Med. Biol.*, 45(4):933–946, 2000.

[40] J. Baruchel, J. Y. Buffiere, and E. Maire. *X-ray Tomography in Material Science*. Hermes Science Publications, 2000.

[41] T. Takeda, A. Momose, K. Hirano, S. Haraoka, T. Watanabe, and Y. Ital. Human carcinoma: Early experience with phase-contrast x-ray CT with synchrotron radiation - comparative specimen study with optical microscopy. *Radiol.*, 214(1):298–301, 2000.

[42] P. Cloetens, R. Barrett, J. Baruchel, J.-P. Guigay, and M. Schlenker. Phase objects in synchrotron radiation hard x-ray imaging. *J. Phys. D: Appl. Phys.*, 29(1):133–146, 1996.

[43] K. A. Nugent, T. E. Gureyev, D. F. Cookson, D. Paganin, and Z. Barnea. Quantitative phase imaging using hard x rays. *Phys. Rev. Lett.*, 77(14):2961–2964, 1996.

[44] S. W. Wilkins, T. E. Gureyev, D. Gao, A. Pogany, and A. W. Stevenson. Phase-contrast imaging using polychromatic hard X-rays. *Nature*, 384(6607):335–338, 1996.

[45] P. Cloetens, W. Ludwig, J. Baruchel, D. Van Dyck, J. Van Landuyt, J. P. Guigay, and M. Schlenker. Holotomography: Quantitative phase tomography with micrometer resolution using hard synchrotron radiation x rays. *Appl. Phys. Lett.*, 75(19):2912–2914, 1999.

[46] D. Paganin, S. C. Mayo, T. E. Gureyev, P. R. Miller, and S. W. Wilkins. Simultaneous phase and amplitude extraction from a single defocused image of a homogeneous object. *J. Micros.*, 206(1):33–40, 2002.

[47] P. Bleuet, P. Cloetens, P. Gergaud, D. Mariolle, N. Chevalier, R. Tucoulou, J. Susini, and A. Chabli. A hard x-ray nanoprobe for scanning and projection nanotomography. *Rev. Sci. Instrum.*, 80(5):056101, 2009.

[48] T. Weitkamp, D. Haas, D. Wegrzynek, and A. Rack. ANKAphase: Software for single-distance phase retrieval from inline X-ray phase-contrast radiographs. *J. Synchrotron Rad.*, 18(4):617–629, 2011.

[49] P. Bidola, K. Morgan, M. Willner, A. Fehringer, S. Allner, F. Prade, F. Pfeiffer, and K. Achterhold. Application of sensitive, high-resolution imaging at a commercial lab-based X-ray micro-CT system using propagation-based phase retrieval. *J. Microsc.*, 266(2):211–220, 2017.

[50] E. Förster, K. Goetz, and P. Zaumseil. Double crystal diffractometry for the characterization of targets for laser fusion experiments. *Kristall und Technik*, 15(8):937–945, 1980.

[51] V. N. Ingal and E. A. Beliaevskaya. X-ray plane-wave topography observation of the phase contrast from a non-crystalline object. *J. Phys. D*, 28(11):2314–2317, 1995.

[52] T. J. Davis, D. Gao, T. E. Gureyev, A. W. Stevenson, and S. W. Wilkins. Phase-contrast imaging of weakly absorbing materials using hard X-rays. *Nature*, 373(6515):595–598, 1995.

[53] T. Weitkamp, A. Diaz, C. David, F. Pfeiffer, M. Stampanoni, P. Cloetens, and E. Ziegler. X-ray phase imaging with a grating interferometer. *Opt. Express*, 13(16):6296–6304, 2005.

[54] M. Willner, G. Fior, M. Marschner, L. Birnbacher, J. Schock, C. Braun, A. A. Fingerle, P. B. Noël, E. J. Rummeny, F. Pfeiffer, and J. Herzen. Phase-contrast Hounsfield units of fixated and non-fixated soft-tissue samples. *PLoS ONE*, 10(8):e0137016, 2015.

[55] F. Pfeiffer, T. Weitkamp, O. Bunk, and C. David. Phase retrieval and differential phase-contrast imaging with low-brilliance X-ray sources. *Nat. Phys.*, 2(4):258–261, April 2006.

[56] J. Herzen, T. Donath, F. Pfeiffer, O. Bunk, C. Padeste, F. Beckmann, A. Schreyer, and C. David. Quantitative phase-contrast tomography of a liquid phantom using a conventional X-ray tube source. *Opt. Express*, 17(12):10010–10018, 2009.

[57] M. Marschner, M. Willner, G. Potdevin, A. Fehringer, P.B. Noël, F. Pfeiffer, and J. Herzen. Helical X-ray phase-contrast computed tomography without phase stepping. *Sci. Rep.*, 6(23953), 2016.

[58] M. Bech, T. H. Jensen, R. Feidenhans'L, O. Bunk, C. David, and F. Pfeiffer. Soft-tissue phase-contrast tomography with an x-ray tube source. *Phys. Med. Biol.*, 54(9):2747–2753, 2009.

[59] Z. Qi, J. Zambelli, N. Bevins, and G.-H. Chen. Quantitative imaging of electron density and effective atomic number using phase contrast CT. *Phys. Med. Biol.*, 55(9):2669–2677, 2010.

[60] A. Sarapata, M. Chabior, C. Cozzini, J.I. Sperl, D. Bequú, O. Langner, J. Coman, I. Zanette, M. Ruiz-Yaniz, and F. Pfeiffer. Quantitative electron density characterization of soft tissue substitute plastic materials using grating-based x-ray phase-contrast imaging. *Rev. Sci. Instrum.*, 85(10):103708, 2014.

[61] A. Sarapata, M. Willner, M. Walter, T. Duttenhofer, K. Kaiser, P. Meyer, C. Braun, A. Fingerle, P. B. Noël, F. Pfeiffer, and J. Herzen. Quantitative imaging using high-energy X-ray phase-contrast CT with a 70 kVp polychromatic X-ray spectrum. *Opt. Exp.*, 23(1):523–535, 2015.

[62] G. Schulz, T. Weitkamp, I. Zanette, F. Pfeiffer, F. Beckmann, C. David, S. Rutishauser, E. Reznikova, and B. Müller. High-resolution tomographic imaging of a human cerebellum: Comparison of absorption and grating-based phase contrast. *J. R. Soc. Interface*, 7(53):1665–1676, 2010.

[63] G. Schulz, C. Waschkies, F. Pfeiffer, I. Zanette, T. Weitkamp, C. David, and B. Müller. Multimodal imaging of human cerebellum-merging X-ray phase microtomography, magnetic resonance microscopy and histology. *Sci. Rep.*, 2(826), 2012.

[64] S. E. Hieber, C. Bikis, A. Khimchenko, G. Schweighauser, J. Hench, N. Chicherova, G. Schulz, and B. Müller. Tomographic brain imaging with nucleolar detail and automatic cell counting. *Sci. Rep.*, 6(32156), 2016.

[65] B. R. Pinzer, M. Cacquevel, P. Modregger, S. A. McDonald, J. C. Bensadoun, T. Thuering, P. Aebischer, and M. Stampanoni. Imaging brain amyloid deposition using grating-based differential phase contrast tomography. *NeuroImage*, 61(4):1336–1346, 2012.

[66] K. S. Morgan, D. M. Paganin, and K. K. W. Siu. Quantitative x-ray phase-contrast imaging using a single grating of comparable pitch to sample feature size. *Opt. Lett.*, 36(1):55–57, 2011.

[67] J. Rizzi, P. Mercére, M. Idir, P. Da Silva, G. Vincent, and J. Primot. X-ray phase contrast imaging and noise evaluation using a single phase grating interferometer. *Opt. Express*, 21(14):17340–17351, 2013.

[68] A. Balles, C. Fella, J. Dittmann, W. Wiest, S. Zabler, and R. Hanke. X-ray grating interferometry for 9.25 keV design energy at a liquid-metal-jet source. *AIP Conf. Proc.*, 1696:020043, 2016.

[69] A. Hipp, J. Herzen, J. U. Hammel, P. Lytaev, A. Schreyer, and F. Beckmann. Single-grating interferometer for high-resolution phase-contrast imaging at synchrotron radiation sources. *Proc. SPIE*, 9967:996718, 2016.

[70] Y.Takeda, W. Yashiro, Y. Suzuki, S. Aoki, T. Hattori, and A. Momose. X-ray phase imaging with single phase grating. *Japan. J. Appl. Phys.*, 46(1L):L89, 2007.

[71] M. Engelhardt, J. Baumann, M. Schuster, C. Kottler, F. Pfeiffer, O. Bunk, and C. David. High-resolution differential phase contrast imaging using a magnifying projection geometry with a microfocus x-ray source. *Appl. Phys. Lett.*, 90(22):224101, 2007.

[72] T. Thüring, M. Abis, Z. Wang, C. David, and M. Stampanoni. X-ray phase-contrast imaging at 100 keV on a conventional source. *Sci. Rep.*, 4(5198), 2014.

[73] L. Birnbacher, M. Willner, A. Velroyen, M. Marschner, A. Hipp, J. Meiser, F. Koch, T. Schröter, D. Kunka, J. Mohr, F. Pfeiffer, and J. Herzen. Experimental realisation of high-sensitivity laboratory x-ray grating-based phase-contrast computed tomography. *Sci. Rep.*, 6(24022), 2016.

[74] F. Pfeiffer, M. Bech, O. Bunk, P. Kraft, E. F. Eikenberry, Ch. Brönnimann, C. Grünzweig, and C. David. Hard X-ray dark-field imaging using a grating interferometer. *Nat. Mater.*, 7(2):134–137, 2008.

[75] T. Weitkamp, C. David, C. Kottler, O. Bunk, and F. Pfeiffer. Tomography with grating interferometers at low-brilliance sources. *Proc. SPIE*, 6318:63180S, 2006.

[76] B. Maco, M. Cantoni, A. Holtmaat, A. Kreshuk, F. A. Hamprecht, and G. W. Knott. Semiautomated correlative 3D electron microscopy of in vivo-imaged axons and dendrites. *Nat. Protoc.*, 9(6):1354–1366, 2014.

List of Figures

About the Author

List of Publications

Journal Publications

A. Khimchenko, C. Bikis, A. Pacureanu, S. E. Hieber, P. Thalmann, H. Deyhle, G. Schweighauser, J. Hench, M. Müller-Gerbl, G. Schulz, P. Cloetens, and B. Müller, "Nanoanatomy: Three-dimensional imaging of human brain tissues beyond optical resolution." (in preparation)

A. Khimchenko, G. Schulz, P. Thalmann, and B. Müller, "Implementation of a double-grating interferometer for phase contrast computed tomography in a conventional system nanotom® m." *APL Bioengineering* (submitted)

S. E. Hieber, C. Bikis, **A. Khimchenko**, G. Schweighauser, J. Hench, N. Chicherova, G. Schulz, B. Müller, "Tomographic brain imaging with nucleolar detail and automatic cell counting." *Scientific Reports* **6**, 32156 (2016) (doi:10.1038/srep32156)

A. Khimchenko, H. Deyhle, G. Schulz, G. Schweighauser, J. Hench, N. Chicherova, C. Bikis, S. E. Hieber, B. Müller, "Extending two-dimensional histology into the third dimension through conventional micro computed tomography." *NeuroImage* **139**, 26-36 (2016) (doi:10.1016/j.neuroimage.2016.06.005)

Peer-Reviewed Conference Proceedings

A. Khimchenko, G. Schulz, C. Bikis, S. E. Hieber, M. Buscema, H. Deyhle, G. Schweighauser, J. Hench, A.-T. Joita-Pacureanu, P.Thalmann, N. Chicherova, and B. Müller, "Imaging human brain tissue using tomography with conventional and synchrotron X-ray sources." *Proceedings of SPIE* (in preparation)

A. Khimchenko, G. Schulz, C. Bikis, H. Deyhle, N. Chicherova, S. E. Hieber, G. Schweighauser, J. Hench, and B. Müller, "Three-dimensional imaging of human brain tissues using absorption-contrast high-resolution X-ray tomography." *Proceedings of SPIE* **10162**, 101620K (2017) (doi:10.1117/12.2259977)

A. Khimchenko, C. Bikis, G. Schulz, M-C. Zdora, I. Zanette, J. Vila-Comamala, G. Schweighauser, J. Hench, S. E. Hieber, H. Deyhle, P. Thalmann, B. Müller, "Hard X-ray submicrometer tomography of human brain tissue at Diamond Light Source." *Journal of Physics: Conference Series (JPCS)* (2017) (in print)

A. Khimchenko, G. Schulz, H. Deyhle, P. Thalmann, I. Zanette, M-C. Zdora, C. Bikis, A. Hipp, S. E. Hieber, G. Schweighauser, J. Hench, B. Müller, "X-ray micro-tomography for investigations of brain tissues on cellular level." *Proceedings of SPIE* **9967**, 996703 (2016) (doi:10.1117/12.2237554)

S. E. Hieber, C. Bikis, **A. Khimchenko**, G. Schulz, H. Deyhle, P. Thalmann, N. Chicherova, A. Rack, M-C. Zdora, I. Zanette, G. Schweighauser, J. Hench, B. Müller, "Computational cell quantification in the human brain tissues based on hard X-ray phase-contrast tomograms." *Proceedings of SPIE* **9967**, 99670K (2016) (doi:10.1117/12.2237012)

N. Chicherova, S. E. Hieber, G. Schulz, **A. Khimchenko**, C. Bikis, P. C. Cattin, B. Müller, "Automatic histology registration in application to X-ray modalities ." *Proceedings of SPIE* **9967**, 996708 (2016) (doi:10.1117/12.2237322)

H. Deyhle, G. Schulz, **A. Khimchenko**, C. Bikis, S. E. Hieber, C. Jaquiery, C. Kunz, M. Müller-Gerbl, S. Höchel, T. Saxer, A. K. Stalder, B. Ilgenstein, F. Beckmann, P. Thalmann, M. Buscema, N. Rohr, M. N. Holme, B. Müller, "Imaging tissues for biomedical research using the high-resolution micro-tomography system nanotom® m." *Proceedings of SPIE* **9967**, 99670Q (2016) (doi:10.1117/12.2237809)

A. Khimchenko, G. Schulz, H. Deyhle, S. E. Hieber, S. Hasan, C. Bikis, J. Schulz, L. Costeur, B. Müller, "Non-destructive phase contrast hard X-ray imaging to reveal the three-dimensional microstructure of soft and hard tissues." *Proceedings of SPIE* **9797**, 97970B (2016) (doi:10.1117/12.2222038)

Peer-Reviewed Conference Abstracts

A. Khimchenko, G. Schulz, I. Zanette, M.-C. Zdora, A. Hipp, H. Deyhle, S. E. Hieber, C. Bikis, G. Schweighauser, J. Hench, P. Thalmann, B. Müller, "Single grating X-ray phase-contrast tomography for evaluation of brain tissue degeneration on cellular level." *European Cells and Materials* **32**, 2, 41 (2016) (doi:10.22203/eCM)

A. Khimchenko, B. Müller, G. Schulz, "Energy shift of the pink beam at the beamline ID19 measured with a grating interferometer and a liquid phantom." *European Cells and Materials* **30**, 47 (2015)

Publications and Conference Proceedings not directly related to the present thesis

N. Chicherova, S. E. Hieber, **A. Khimchenko**, C. Bikis, B. Müller, P. Cattin, "Automatic Deformable Registration of Histological Slides to µCT volume data." *Journal of Microscopy* (in preparation)

G. Schulz, C Götz, M. Müller-Gerbl, I. Zanette, M-C. Zdora, **A. Khimchenko**, H. Deyhle, P. Thalmann, B. Müller, "Multimodal imaging of the human knee down to the cellular level." *Journal of Physics: Conference Series (JPCS)* (2017) (in press)

M.-C. Zdora, J. Vila-Comamala, G. Schulz, **A. Khimchenko**, A. Hipp, A. Cook, D. Dilg, C. David, C. Grünzweig, C. Rau, P. Thinault, and I. Zanette, "X-ray phase microtomography with a single grating for high-throughput investigations of biological tissue." *Biomedical Optics Express* **8**, 2, 1257-1270 (2017) (doi:10.1364/BOE.8.001257)

G. Schulz, C. Götz, H. Deyhle, M. Müller-Gerbl, I. Zanette, M-C. Zdora, **A. Khimchenko**, P. Thalmann, A. Rack, B. Müller, "Hierarchical imaging of the human knee." *Proceedings of SPIE* **9967**, 99670R (2016) (doi:10.1117/12.2238089)

C. Bikis, P. Janz, G. Schulz, G. Schweighauser, J. Hench, P. Thalmann, H. Deyhle, N. Chicherova, A. Rack, **A. Khimchenko**, S. E. Hieber, L. Mariani, C. A. Haas, B. Müller, "High-resolution synchrotron radiation-based phase tomography of the healthy and epileptic brain." *Proceedings of SPIE* **9967**, 996706 (2016) (doi:10.1117/12.2237816)

M. Buscema, G. Schulz, H. Deyhle, **A. Khimchenko**, S. Matviykiv, M. N. Holme, A. Hipp, F. Beckmann, T. Saxer, K. Michaud, B. Müller, "Histology-validated X-ray tomography for imaging human coronary arteries." *Proceedings of SPIE* **9967**, 99670O (2016) (doi:10.1117/12.2238702)

S. E. Hieber, C. N. Bikis, **A. Khimchenko**, G. Schulz, G. Schweighauser, J. Hench, B. Müller, "Three-dimensional imaging of brain tissue by grating-based micro computed tomography using synchrotron radiation." *European Cells and Materials* **30**, 44 (2015)

S. E. Hieber, **A. Khimchenko**, C. Kelly, L. Mariani, P. Thalmann, G. Schulz, R. Schmitz, I. Greving, M. Dominietto, B. Müller , "Three-dimensional imaging of human hippocampal tissue using synchrotron radiation- and grating-based micro computed tomography." *Proceedings of SPIE* **9212**, 92120S (2014) (doi:10.1117/12.2061582)

P. Thalmann, S. E. Hieber, G. Schulz, H. Deyhle, **A. Khimchenko**, V. Kurtcuoglu, U. Olgac, A. Marmaras, W. Kuo, E. P. Meyer, F. Beckmannd, J. Herzen, S. Ehrbar, B. Müller, "Three-dimensional registration of synchrotron radiation-based micro-computed tomography images with advanced laboratory micro-computed tomography data from murine kidney casts." *Proceedings of SPIE* **9212**, 92120Y (2014) (doi:10.1117/12.2060809)

List of Posters and Presentations

A. Khimchenko, G. Schulz, C. Bikis, S. E. Hieber, M. Buscema, H. Deyhle, G. Schweighauser, J. Hench, A.-T. Joita-Pacureanu, P.Thalmann, N. Chicherova, and B. Müller "Imaging human brain tissue using tomography with conventional and synchrotron X-ray sources"; SPIE Conference: Developments in X-Ray Tomography XI, San Diego, USA, 6 - 10 August 2017 - ORAL PRESENTATION (invited paper)

A. Khimchenko, G. Schulz, H. Deyhle, N. Chicherova, S. E. Hieber, C. Bikis, G. Schweighauser, J. Hench, P. Thalmann, and B. Müller "Imaging human brain tissue down to cellular level using hard X-ray tomography with conventional and synchrotron sources"; European & Global Summit for Cutting-Edge Medicine: Clinical Nanomedicine and Targeted Medicine (CLINAM2017), Basel, Switzerland, 7 - 10 May 2017 - POSTER PRESENTATION

A. Khimchenko, G. Schulz, C. Bikis, H. Deyhle, N. Chicherova, S. E. Hieber, G. Schweighauser, J. Hench, and B. Müller "Three-dimensional imaging of human brain tissues using absorption-contrast high-resolution X-ray tomography"; SPIE Conference: Smart Structures/NDE, Portland, USA, 25 - 29 March 2017 - ORAL PRESENTATION

A. Khimchenko, G. Schulz, M. Buscema, C. Götz, and B. Müller "Laboratory-based hard X-ray grating interferometry using the nanotom® m to augment the visualization of human tissues"; International Symposium on BioMedical Applications of X-Ray Phase Contrast Imaging (IMXP2017) 2017, Garmisch-Partenkirchen, Germany, 26 - 27 January 2017 - POSTER PRESENTATION

A. Khimchenko, G. Schulz, H. Deyhle, P. Thalmann, I. Zanette, M.-C. Zdora, C. Bikis, A. Hipp, S. E. Hieber, G. Schweighauser, J. Hench, and B. Müller "X-ray micro-tomography for investigations of brain tissues on cellular level"; SPIE Conference: Developments in X-Ray Tomography X, San Diego, USA, 28 - 31 August 2016 - ORAL PRESENTATION

A. Khimchenko,S. E. Hieber, H. Deyhle, G. Schulz, I. Zanette, C. Bikis, J. Hench, G. Schweighauser, P. Thalmann, M.-C. Zdora, J. Vila-Comamala, and B. Müller "X-ray nano-microscopy at Diamond I13-2 beamline for the investigation of brain tissues"; X-Ray Microscopy Conference (XRM2016), Oxford, UK, 15 - 19 August 2016 - POSTER PRESENTATION + "SMALL TALK"

A. Khimchenko, G. Schulz, C. Götz, H. Deyhle, S. E. Hieber, and B. Müller "Grating-based X-ray phase contrast tomography for visualization of soft and hard tissues"; European & Global Summit for Cutting-Edge Medicine: Clinical Nanomedicine and Targeted Medicine (CLINAM2016), Basel, Switzerland, 26 - 29 June 2016 - POSTER PRESENTATION

A. Khimchenko, G. Schulz, I. Zanette, M.-C. Zdora, A. Hipp, H. Deyhle, S. E. Hieber, C. Bikis, G. Schweighauser, J. Hench, P. Thalmann, and B. Müller "Single grating X-ray phase-contrast tomography for evaluation of brain tissue degeneration on cellular level"; 22th Swiss Conference on Biomaterials and Regenerative Medicine (SSB+RM2016), Schulthess Klinik, Zürich, Switzerland, 9 - 10 June 2016 - POSTER PRESENTATION

C. N. Bikis, G. Schweighauser, J. Hench, S. Frank, G. Schulz, **A. Khimchenko**, B. Müller, and S. E. Hieber "Phase tomography as a three dimensional complement to histology"; Annual meeting of the SGPath, Basel, Switzerland, 12 - 14 November 2015 - POSTER PRESENTATION

M.-C. Zdora, J. Vila-Comamala, **A. Khimchenko**, G. Schulz, A. Hipp, V. Kuppili, A. C. Cook, C. David, C. Grünzweig, P. Thibault, C. Rau, and I. Zanette "Recent advances in x-ray phase-contrast imaging for biomedical applications at Diamond I13 Beamline"; International Symposium on BioMedical Applications of X-Ray Phase Contrast Imaging (IMXP2016), Garmisch-Partenkirchen, Germany, 21 - 22 January 2015 - POSTER PRESENTATION

M.-C. Zdora, J. Vila-Comamala, **A. Khimchenko**, G. Schulz, A. Hipp, V. Kuppili, A. C. Cook, C. David, C. Grünzweig, C. Rau, P. Thibault, and I. Zanette "X-ray phase-contrast imaging at Diamond I13 Beamline"; 23rd International Congress on X-ray Optics and Microanalysis (ICXOM23), New York, USA, 14 - 18 September 2015 - POSTER PRESENTATION

B. Müller, P. Thalmann, C. Bikis, **A. Khimchenko**, N. Chicherova, M. D. Dominietto, H. Deyhle, S. E. Hieber, and G. Schulz "Multi-modal hard X-ray phase tomography of human brain tissues"; International conference on X-ray and Neutron Phase Imaging with Gratings (XNPIG2015), Bethesda, US, 8 - 11 September 2015 - ORAL PRESENTATION

G. Schulz, **A. Khimchenko**, and B. Müller "Grating-based X-ray phase tomography setup for commercial CT system nanotom® m tissues"; International conference on X-ray and Neutron Phase Imaging with Gratings (XNPIG2015), Bethesda, US, 8 - 11 September 2015 - ORAL PRESENTATION

A. Khimchenko, B. Müller, and G. Schulz "Three-dimensional visualization of brain tissues by phase contrast microtomography using synchrotron radiation"; 21th Swiss Conference on Biomaterials and Regenerative Medicine (SSB+RM2015), Lausanne, Switzerland, 9 - 10 June 2015 - POSTER PRESENTATION

A. Khimchenko, G. Schulz, S. Bugna, I. Zanette, M. Ruiz Yaniz, B. Müller "Synchrotron-radiation grating-based x-ray phase tomography of selected materials for calibration of grating-based measurements at nanotom® m"; International Symposium on BioMedical Applications of X-Ray Phase Contrast Imaging (IMXP2015), Garmisch-Partenkirchen, Germany, 29 - 30 January 2015 - POSTER PRESENTATION

List of Awards

Student Travel Award from the Swiss Society for Biomaterials and Regenerative Medicine (SSB+RM), Switzerland, 2016

H. Don Wolpert award from the Bioinspiration, Biomimetics, and Bioreplication SPIE conference sponsored by the Optical Society of Southern California, USA, 2016